

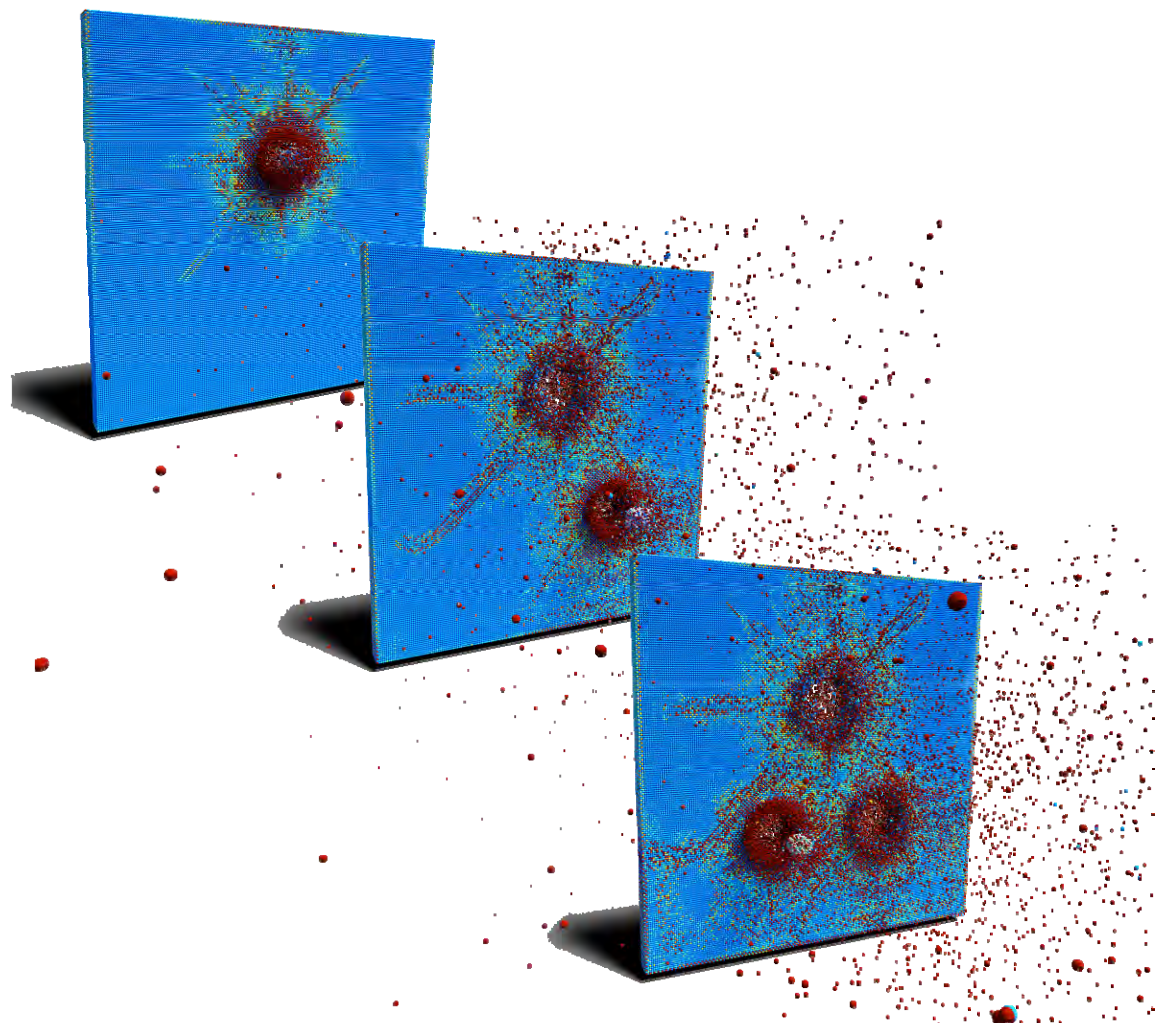


US Army Corps
of Engineers®
Engineer Research and
Development Center

A Multiscale Meshfree Approach for Modeling Fragment Penetration into Ultra High-Strength Concrete

J. S. Chen, S. W. Chi, C. H. Lee, S P. Lin,
C. Marodon, M. J. Roth, and T. R. Slawson

September 2011



A Multiscale Meshfree Approach for Modeling Fragment Penetration into Ultra High-Strength Concrete

M. J. Roth and T. R. Slawson

*Geotechnical and Structures Laboratory
U.S. Army Engineer Research and Development Center
3909 Halls Ferry Road
Vicksburg, MS 39180-6199*

J. S. Chen, S. W. Chi, C. H. Lee, S. P. Lin, and C. Marodon

*Department of Civil and Environmental Engineering
University of California, Los Angeles
Los Angeles, CA 90095*

Final report

Approved for public release; distribution is unlimited.

Prepared for U.S. Army Engineer Research and Development Center
3909 Halls Ferry Road
Vicksburg, MS 39180-6199

Abstract: Results from the efforts in meshfree method development for fragment-impact modeling during April 2009 to March 2011 are described in this report. These efforts focused on an enhanced semi-Lagrangian reproducing kernel particle method formulation for modeling large material deformation and damage mechanisms, multiscale homogenization based on the energy bridging theory pertinent to fragment penetration modeling of concrete materials, and enhanced kernel contact algorithms to model multi-body contact applicable to penetration problems. Several benchmark problems associated with contact-impact simulations as well as multiscale modeling of material damage have been performed to examine the effectiveness of the developed computational methods. These newly developed computational formulations and the associated numerical algorithms have been implemented into the parallel Nonlinear Meshfree Analysis Program (NMAP) code. The numerical formulations and NMAP code implementation accomplished under this effort have been evaluated through 18 verification and validation (V&V) tests based on penetration experiments conducted at The U.S. Army Engineer Research and Development Center (ERDC). The latest version of the NMAP code has been delivered to ERDC. This report, together with the 2009 technical report (Chen et al. 2009), offers the theoretical foundation of NMAP for general users.

DISCLAIMER: The contents of this report are not to be used for advertising, publication, or promotional purposes. Citation of trade names does not constitute an official endorsement or approval of the use of such commercial products. All product names and trademarks cited are the property of their respective owners. The findings of this report are not to be construed as an official Department of the Army position unless so designated by other authorized documents.

DESTROY THIS REPORT WHEN NO LONGER NEEDED. DO NOT RETURN IT TO THE ORIGINATOR.

Contents

Figures and Tables.....	v
Preface.....	viii
Work Accomplished in FY09-11.....	ix
1 Introduction.....	1
2 Semi-Lagrangian RKPM for Contact-Impact Modeling.....	2
Reproducing kernel approximation	2
Semi-Lagrangian reproducing kernel discretization.....	5
<i>Governing equations.....</i>	5
<i>Semi-Lagrangian discretization.....</i>	6
Stabilized Non-conforming Nodal Integration (SNNI).....	9
<i>Boundary correction of SNNI domain integration</i>	11
<i>Temporal stability of semi-Lagrangian RKPM</i>	12
Implementation	15
3 Multiscale Microcrack Informed Damage Model.....	18
Model problem and homogenization operators	18
Energy bridging between scales	24
Characterization of parameters in continuum damage mechanics by energy bridging.....	26
<i>One-parameter scalar damage model.....</i>	26
<i>Two-parameter damage model</i>	27
<i>Fully tensorial damage model</i>	28
Microscopic cell analysis	29
Numerical examples.....	31
<i>Characterization of damage evolution functions</i>	32
<i>Mesh insensitive solution by scaled damage evolution functions</i>	37
4 Enhanced Frictional Natural Kernel Contact Algorithm for Impact Modeling.....	40
Kernel contact algorithm	40
Level set algorithm for determination of surface normal	42
Numerical examples.....	43
<i>Elastic collision of two bodies.....</i>	44
<i>Sliding block on a rigid surface</i>	45
<i>Dynamic Hertz contact.....</i>	47
<i>Dynamic contact of elastic ring.....</i>	48
<i>Cylindrical aluminum bar impacting a rigid wall</i>	51
5 V&V Penetration Study	54
Experimental setup	54

NMAP model	56
Determination of optimal parameters for V&V modeling.....	56
Summary of numerical simulation of V&V problems	66
Comparisons between macroscale and multiscale AFC models.....	72
Empirical formula extracted from penetration V&V numerical and experimental data	79
Summary and discussions.....	83
6 Conclusions.....	86
References.....	89
Appendix A: Derivation of Influence Tensor Using Asymptotic Expansion Based Homogenization.....	92
Appendix B: Derivation of Energy Bridging Equation Using Asymptotic Expansion Based Homogenization.....	95
Appendix C: Two-Variable Damage Model	98
Report Documentation Page	

Figures and Tables

Figures

Figure 1. Contour for 2-D RKPM shape function with rectangular support: (a) domain of influence, (b) RK shape function.	5
Figure 2. Comparison of FEM and RKPM discretization and domains of influence: (a) FEM discretization and (b) RKPM discretization. (The domain of influence of one node is marked in grey color as an example.)	5
Figure 3. Comparison of Lagrangian and semi-Lagrangian kernel supports in undeformed and deformed configurations: (a) undeformed configuration, (b) Lagrangian kernel deformed with the material in the deformed configuration, and (c) semi-Lagrangian kernel in the deformed configuration.	7
Figure 4. Strain smoothing domains for SCNI.	11
Figure 5. Strain smoothing domains for SNNI.	11
Figure 6. Side view of the smoothing domains on the left end of the rod. Solid thick lines: problem boundary; thin solid lines: boundaries of smoothing domains.	13
Figure 7. Wave propagation solved by semi-Lagrangian RKPM with SNNI domain integration method: (a) without boundary SNNI smoothing zone correction, (b) with boundary SNNI smoothing zone correction.	13
Figure 8. Correction of the boundary smoothing domains.	13
Figure 9. Contour plot of amplification factor of semi-Lagrangian discrete equation with SNNI.	14
Figure 10. Flow chart of dynamic semi-Lagrangian RKPM code structure.	15
Figure 11. Neighbors of point L marked as black dot.	16
Figure 12. Bucket search of candidate neighbors of point L (open dash circle points).	16
Figure 13. Bucket search scheme and the bucket update.	17
Figure 14. Microscopic and macroscopic structures.	19
Figure 15. Homogenization of a microscopic cell with fluctuating fields.	20
Figure 16. Notched beam subjected to three-point bending (unit: cm).	32
Figure 17. Microscopic cell problem and cohesive crack model.	33
Figure 18. Normal stress contours (in direction of loading) at different loading stages.	33
Figure 19. (a) Homogenized stress and strain and (b) tensile damage parameter calculated by the microscopic stress and strain fields, where a, b, c, d and e denote the corresponding homogenized stresses, strains and damage parameters calculated based on the stress fields (a), (b), (c), (d) and (e) shown in Figure 18, respectively.	33
Figure 20. Homogenized stress-strain curve.	35
Figure 21. Size dependence of microscopic cells: (a) nominal strength; (b) difference between rupture strain ϵ_u and peak strain ϵ_t	36
Figure 22. Microcracks informed damage evolutions.	36
Figure 23. Finite element mesh with different levels of refinement: (a) coarse mesh; (b) medium mesh; (c) fine mesh.	37
Figure 24. Mesh dependent load-displacement responses using inconsistent microscopic cell.	38

Figure 25. Mesh independent load-displacement responses using consistent microscopic cell.	39
Figure 26. Contour of normal stress in horizontal direction.	39
Figure 27. Contour of normal strain in horizontal direction.	39
Figure 28. Kernel contact algorithm by kernel interaction between contacting bodies.	41
Figure 29. Level set algorithm to identify contact nodes and obtain normal vector of the contact surface.	43
Figure 30. Geometric schematic of two-body elastic contact.	44
Figure 31. Numerical results of two-body elastic contact with same properties and support sizes.	44
Figure 32. Numerical results of two-body elastic contact with $m_1 = m$, $m_2 = 4m$ and $a_1 = 2.0$, $a_2 = 1.75$	45
Figure 33. Schematic of an elastic block resting on a rigid surface subject to gravity.	46
Figure 34. Sliding block problem with the enhanced natural kernel contact algorithm and level set identification of contact surface normal ($\mu = 0.2$)	46
Figure 35. Comparison of block displacement in the sliding block problem with the natural kernel contact algorithm and level set identification of contact surface normal.	47
Figure 36. Hertz contact problem: (a) problem statement and (b) RKPM discretization.	47
Figure 37. Numerical result of contact radius compared to analytical solution (Timoshenko and Goodier 1934).	48
Figure 38. Geometry of an elastic ring impacting on a rigid surface.	49
Figure 39. Impact of an elastic ring on a rigid surface by natural kernel contact algorithm.	49
Figure 40. Comparison of impact and reflected angles between two algorithms for determination of contact surface normal.	50
Figure 41. Geometry of two elastic rings.	50
Figure 42. Impact of two elastic rings using natural kernel contact algorithm.	50
Figure 43. Time-history of total energy for the two-ring impact problem.	51
Figure 44. Schematic of Taylor bar problem and corresponding RKPM discretization.	52
Figure 45. Cylindrical impact deformations predicted by the semi-Lagrangian SNNI RKPM.	53
Figure 46. CorTuf panel mounted in test support fixture, (a) front view (impact face) and (b) side view.	55
Figure 47. Study 1 problem statement.	58
Figure 48. Velocity histories of Study 1.	58
Figure 49. Study 2 problem statement.	59
Figure 50. Linear momentum history.	59
Figure 51. Energy history.	60
Figure 52. Time-step effect on the velocity history.	62
Figure 53. Yield stress versus strain rate for steel (Rule and Jones 1998).	62
Figure 54. Boundary layer correction.	63
Figure 55. Projectile deformation without support size adjustment.	64
Figure 56. Projectile discretization and cross section.	65

Figure 57. Smoothing zone for SNNI (smoothing zone shaded).	65
Figure 58. Comparison of velocity reduction for V&V tests using 32-grain projectiles.....	68
Figure 59. Comparison of velocity reduction for V&V tests using 86-grain projectiles.....	68
Figure 60. Comparison of velocity reduction for V&V tests using 129-grain projectiles.	69
Figure 61. Illustration of measurement of crater sizes and hole dimensions.....	69
Figure 62. Velocity history of Run 6.....	72
Figure 63. Comparison of damage pattern for Run 6.	73
Figure 64. Velocity history of Run 7.	73
Figure 65. Comparison of damage pattern for Run 7.	74
Figure 66. Velocity history of Run 10.....	74
Figure 67. Comparison of damage pattern for Run 10.....	75
Figure 68. Velocity history of Run 16.....	75
Figure 69. Comparison of damage pattern for Run 16.	76
Figure 70. Damage pattern of Run 12.....	77
Figure 71. Damage pattern of Run 9.....	77
Figure 72. Damage pattern of Run 13.....	78
Figure 73. Damage pattern of Run 3.	78
Figure 74. Damage pattern of Run 7.	79
Figure 75. Velocity reduction rate with various thicknesses and impact velocities.....	80
Figure 76. Normalized impact velocity vs. exit velocity (32-grain projectile).....	81
Figure 77. Normalized impact velocity vs. exit velocity (86-grain projectile).....	81
Figure 78. Normalized impact velocity vs. exit velocity (129-grain projectile).....	82
Figure 79. Normalized impact kinetic energy vs. exit kinetic energy.	84

Tables

Table 1. Comparison of deformed geometries for Taylor bar impact problem.....	53
Table 2. Spherical steel projectile properties.	54
Table 3. J2 material model parameters for projectile.....	56
Table 4. AFC model parameters for CorTuf panel.	57
Table 5. Effect of support size on numerical result in terms of velocity.....	59
Table 6. Effect of discretization on exit velocity.	60
Table 7. Discretization of projectile.	61
Table 8. Summary of selected parameters.....	66
Table 9. Exit velocity comparison.	67
Table 10. Crater and hole diameter comparison.	70
Table 11. Projectile and panel mass loss and crater debris weight comparison.....	71
Table 12. Comparisons of exit velocity between macroscale, multiscale AFC models and experimental measurement.....	79
Table 13. Minimum required normalized velocity.	82
Table 14. Fitted coefficient c and critical value $\bar{K}_{critical}$	84

Preface

This report documents research conducted in fiscal years (FY) 2009 through FY 2011 by personnel of the University of California, Los Angeles (UCLA) under contract number W912HZ-07-C-0019. The research was performed in collaboration with, and directed by, personnel of the Survivability Engineering Branch (SvEB), Geosciences and Structures Division (GSD), Geotechnical and Structures Laboratory (GSL), U.S. Army Engineer Research and Development Center (ERDC). Numerical simulations were jointly performed on systems of the ERDC Department of Defense Supercomputing Resource Center and the UCLA computational cluster.

Research funding was provided by the Army Technology Objective-Demonstration research program D.FP.2009.05, DEFeat of Emerging Adaptive Threats (DEFEAT). R. Nicholas Boone was DEFEAT work package manager.

Principal investigator for the UCLA research team was Professor J. S. Chen, Chair and Chancellor's Professor, Department of Civil and Environmental Engineering. ERDC principal investigating engineers were Dr. Thomas R. Slawson and M. Jason Roth, SvEB. Support in scientific data visualization was provided by Dr. Mike Stephens, Miguel Valenciano, Kevin George, and David Longmire, ERDC Data Analysis and Assessment Center.

This report was prepared by Chen, S. W. Chi, C. H. Lee, S. P. Lin and C. Marodon, UCLA, and by Slawson and Roth, SvEB. The research was accomplished under the general supervision of James L. Davis, Chief, SvEB, Bartley P. Durst, Chief, GSD, Dr. William P. Grogan, Deputy Director, GSL, and Dr. David W. Pittman, Director, GSL.

COL Kevin J. Wilson was Commander of ERDC. Dr. Jeffery P. Holland was Director.

Work Accomplished in FY09-11

Major Tasks	Descriptions
1. Enhanced semi-Lagrangian RKPM formulation for modeling excessive material deformation and damage	<p>Semi-Lagrangian RKPM discretization for problems with large material deformation and material separation due to damage</p> <p>Stabilized non-conforming nodal integration (SNNI) for semi-Lagrangian formulation</p> <p>Boundary correction of SNNI domain integration</p> <p>Temporal stability analysis of semi-Lagrangian formulation with SNNI domain integration</p>
2. Multiscale homogenization based on the energy bridging theory pertinent to the fragment penetration modeling of concrete materials	<p>Construction of constitutive tensor with damage induced material degradation based on homogenization of microcracks using asymptotic expansion</p> <p>Microcrack informed damage model (MIDM) based on energy bridging between meso and continuum scales</p> <p>Energy based bridging between continuum-scale damage evolution and microcrack growth</p> <p>Characterization of damage evolution functions with microcell analysis for various damage models</p> <p>Study of numerical size effect between the microcell and continuum-scale models</p> <p>Scaling law for alleviating numerical size effect</p> <p>Development and implementation of MIDM-enhanced ERDC AFC model into NMAP code</p>
3. Enhanced kernel contact algorithms to model multi-body contact applicable to penetration problems	<p>Kernel contact algorithms for multi-body contact</p> <p>Fictitious plasticity law for representing stick-slip conditions under kernel contact framework</p> <p>Level set algorithm for geometry representation in multi-body contact</p>
4. Verification and Validation (V&V) tests of NMAP code	<p>Parametric study of RKPM models for V&V tests</p> <p>Optimal discretization parameters: nodal density, support size</p> <p>Stable time-step size</p> <p>Boundary correction and support size adjustment in contact modeling</p> <p>Dynamic increase factor (DIF)</p> <p>Comparison of RKPM numerical results and experimental data</p> <p>Exit velocity and mass loss of projectile</p> <p>Crater and hole sizes as well as debris weights of panel</p> <p>Damage patterns of panel</p> <p>Empirical formula for determination of terminal ballistic conditions</p> <p>Impact and exit velocity relationship</p> <p>Impact and exit kinetic energy relationship</p>

1 Introduction

Impact and penetration processes in brittle materials involve many complex phenomena such as multi-body contact, fast-evolving weak and strong discontinuities resulting from material softening and failure, and extensive material deformation and flow. Lagrangian mesh-based methods are challenged in these problems as a result of excessive mesh distortion and entanglement. Mesh sensitivity associated with material instability in strain localization and shear band formation is an additional issue. In terms of the material description, the common phenomenological approach to continuum damage evolution lacks a direct link to the driving micro-structure failure processes. This results in reduced accuracy in terms of describing material failure and a loss of uniqueness in strain localization problems.

To improve the capability of modeling penetration in brittle geomaterials, a multiscale reproducing kernel particle method (RKPM) (Chen et al. 1996) formulation and a new damage material model for impact and penetration were developed. Major project developments have included:

- Enhanced semi-Lagrangian reproducing kernel (RK) formulation for modeling excessive material deformation and damage (Guan et al., in preparation)
- Multiscale homogenization based on the energy bridging theory pertinent to fragment penetration modeling of concrete materials (Ren et al., in preparation)
- Enhanced kernel contact algorithms to model multi-body contact applicable to penetration problems
- Implementation of new formulations into Nonlinear Meshfree Analysis Program (NMAP) parallel code (Chi et al., in preparation)

Organization of the report is as follows. The semi-Lagrangian RK formulation for impact and penetration is presented in Chapter 2. The multiscale formulation for microcrack-informed damage evolution is presented in Chapter 3. Recent enhancements of the kernel contact algorithm are given in Chapter 4. Results from a V&V study on penetration modeling with the NMAP code are given in Chapter 5. Conclusions are given in Chapter 6.

2 Semi-Lagrangian RKPM for Contact-Impact Modeling

For large deformation problems involving severe material damage and separation, the deformation gradient is no longer positive definite at all material points and the Total Lagrangian formulation is no longer applicable. Therefore, to address the limitation of Lagrangian discretization for modeling materials with loss of positive definiteness, a semi-Lagrangian RKPM based on an updated Lagrangian formulation has been proposed (Guan et al. 2009; Guan et al., in preparation). In semi-Lagrangian RKPM, the mathematical points are attached to the material points (and thus, Lagrangian), while the supports of reproducing kernel shape functions do not necessarily deform with the materials (and thus semi-Lagrangian). In this approach the neighbor points are redefined during the deformation process to account for large material flow and formation of free surfaces, and the approximation is constructed at the current configuration. In this work, the semi-Lagrangian RKPM framework is introduced for contact-impact modeling. The stability conditions of this approach for explicit time integration are also presented.

Reproducing kernel approximation

Two most commonly used approximation methods in meshfree formulations are the moving least-squares (MLS) approximation and the RK approximation. Different from the finite element method (FEM) where the approximation functions are constructed in the mesh mapped to a natural coordinate, MLS and RK approximations are constructed based on nodal positions in the Cartesian coordinate. This chapter gives a review of the RK approximation, which is the foundation of RKPM.

Consider a closed domain $\bar{\Omega} = \Omega \cup \partial\Omega$, where Ω is the open domain and $\partial\Omega$ is the boundary of Ω , discretized by a set of nodes $\{x_1, x_2, \dots, x_{NP}\}$, $x_I \in \bar{\Omega}$, $I=1, 2, \dots, NP$ and NP is the number of points. The RK approximation of a function u , denoted by u^h , is expressed as (Chen et al. 1996) in Equation 1.

$$u^h(x) = \sum_{I=1}^{NP} \Psi_I(x) d_I \quad (1)$$

where $\Psi_I(x)$ is the RK shape function, and d_I is the corresponding coefficient. The RK shape function is constructed with the following form

$$\Psi_I(x) = C(x; x - x_I) \varphi_a(x - x_I) \quad (2)$$

where x_I is the nodal position vector, $\varphi_a(x - x_I)$ is the kernel function, and $C(x; x - x_I)$ is the correction function.

The kernel function $\varphi_a(x - x_I)$ is a compactly supported positive function

$$\begin{cases} \varphi_a(x - x_I) \geq 0, & \|x - x_I\| / a \leq 1 \\ \varphi_a(x - x_I) = 0, & \|x - x_I\| / a > 1 \end{cases} \quad (3)$$

where a is the measure of support of $\varphi_a(x - x_I)$. The kernel function expressed in Equation 3 has a spherical support with radius a . A kernel function with a rectangular or cubic support can be constructed by multiplication of one-dimensional (1-D) kernel functions (Chen et al. 1996). The kernel function $\varphi_a(x - x_I)$ defines the locality and order of continuity of the approximation. The correction function $C(x; x - x_I)$ is the combination of complete n^{th} order monomials

$$\begin{aligned} C(x; x - x_I) &= \sum_{i+j+k=0}^n b_{ijk}(x) (x_1 - x_{I1})^i (x_2 - x_{I2})^j (x_3 - x_{I3})^k \\ &= H^T(x - x_I) b(x) \end{aligned} \quad (4)$$

$$H^T(x - x_I) = \begin{bmatrix} 1 & x_1 - x_{I1} & x_2 - x_{I2} & x_3 - x_{I3} & (x_1 - x_{I1})^2 & \dots & (x_3 - x_{I3})^n \end{bmatrix} \quad (5)$$

where $b_{ijk}(x)$ are the coefficients of the basis functions, and $b(x)$ and $H(x - x_I)$ are vectors of the coefficients and monomial basis functions, respectively. The coefficient vector $b(x)$ is solved by enforcing the exact reproduction of the monomial bases up to the n^{th} order.

$$\sum_{I=1}^{NP} \Psi_I(x) x_{I1}^i x_{I2}^j x_{I3}^k = x_1^i x_2^j x_3^k \quad i + j + k = 0, 1, \dots, n \quad (6)$$

Equation 6 can be transformed to the following.

$$\sum_{I=1}^{NP} \Psi_I(\mathbf{x}) (\mathbf{x}_1 - \mathbf{x}_{1I})^i (\mathbf{x}_2 - \mathbf{x}_{2I})^j (\mathbf{x}_3 - \mathbf{x}_{3I})^k = \delta_{i0} \delta_{j0} \delta_{k0} \quad i+j+k=0,1,\dots,n \quad (7)$$

By substituting Equation 2 and 4 into Equation 7, the coefficient vector $\mathbf{b}(\mathbf{x})$ is obtained as

$$\mathbf{b}(\mathbf{x}) = \mathbf{M}^{-1}(\mathbf{x}) \mathbf{H}(\mathbf{0}) \quad (8)$$

where

$$\begin{aligned} \mathbf{M}(\mathbf{x}) &= \sum_{J=1}^{NP} \mathbf{H}(\mathbf{x} - \mathbf{x}_J) \mathbf{H}^T(\mathbf{x} - \mathbf{x}_J) \varphi_a(\mathbf{x} - \mathbf{x}_J) \\ \mathbf{H}^T(\mathbf{0}) &= [1 \quad 0 \quad 0 \quad 0 \quad 0 \quad \dots \quad 0] \end{aligned} \quad (9)$$

Finally, the RK shape function is obtained as

$$\Psi_I(\mathbf{x}) = \mathbf{H}^T(\mathbf{0}) \mathbf{M}^{-1}(\mathbf{x}) \mathbf{H}(\mathbf{x} - \mathbf{x}_I) \varphi_a(\mathbf{x} - \mathbf{x}_I) \quad (10)$$

Figure 1 shows the contour plot of a two-dimensional (2-D) RK shape function with rectangular support. The kernel support is shown on the left, thus defining the domain of influence, and the shape function is shown on the right, constructed using a cubic B-spline kernel function and linear bases. Figure 2 shows the comparison of RKPM discretization with circular support and an FEM triangular mesh using the same set of points. The domain of influence of each FEM node is determined by the neighboring connected elements, whereas the domain of influence of the RK shape function is defined by the support of the kernel function. While in RKPM discretization, some domains of influence are extended outside of the physical boundary, the reproducing conditions enforced in Equation 6 guarantee the order of accuracy for all $\mathbf{x} \in \bar{\Omega}$. This extended boundary layer in RKPM needs to be considered in contact problems. However, it serves as an “insulation layer” to ensure impenetration conditions in the normal contact similar to the function of a “gap element” in the finite element setting. More details will be discussed in the kernel contact algorithms in Chapter 4.

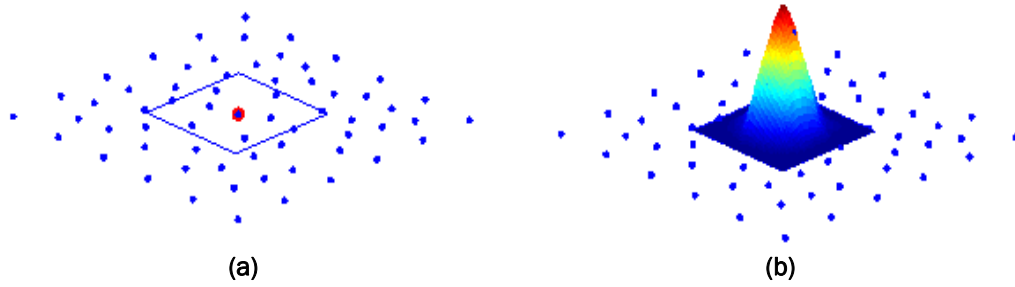


Figure 1. Contour for 2-D RKPM shape function with rectangular support:
(a) domain of influence, (b) RK shape function.

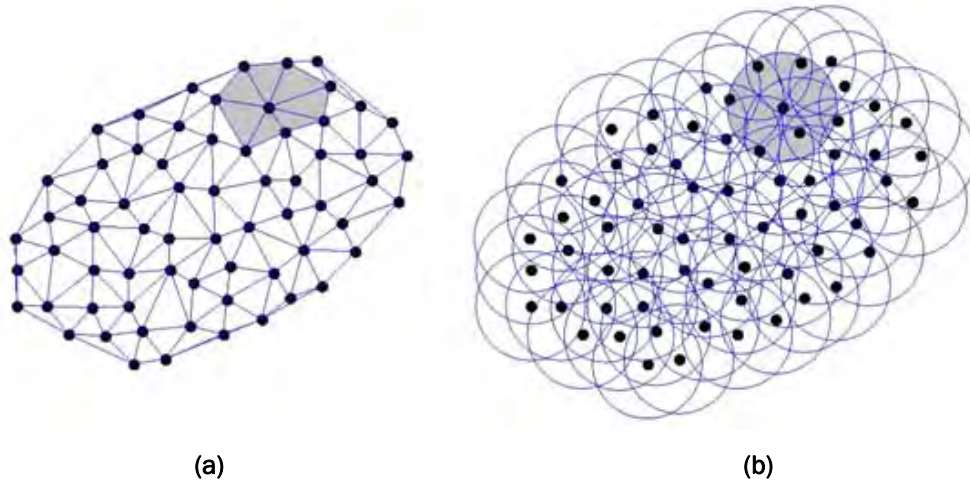


Figure 2. Comparison of FEM and RKPM discretization and domains of influence:
(a) FEM discretization and (b) RKPM discretization. (The domain of influence of one node is marked in grey color as an example.)

Semi-Lagrangian reproducing kernel discretization

Governing equations

For modeling of fragment-impact processes, a semi-Lagrangian RK discretization is introduced to the equation of motion. Start with an updated Lagrangian formulation where the current configuration is the referenced configuration, and introduce a semi-Lagrangian RK approximation constructed in the current configuration to the updated Lagrangian variational equation. Let X be the material coordinate representing the initial position of a material point, and x be the current position of the material point X in the current configuration with domain Ω_x , essential boundary $\partial\Omega_x^g$, and natural boundary $\partial\Omega_x^h$. The weak form of the equation of motion is:

$$\int_{\Omega_x} \delta u_i \rho \ddot{u}_i d\Omega + \int_{\Omega_x} \delta u_{(i,j)} \tau_{ij} d\Omega = \int_{\Omega_x} \delta u_i b_i d\Omega + \int_{\partial\Omega_x^b} \delta u_i h_i d\Gamma \quad (11)$$

where:

u_i = displacement

τ_{ij} = Cauchy stress, $u_{(i,j)} = (\partial u_i / \partial x_j + \partial u_j / \partial x_i) / 2$

ρ = density

b_i = body force

h_i = surface traction

In the pure Lagrangian RKPM formulation, the Lagrangian RK shape functions, $\Psi_I(X)$, are constructed using the material coordinates in the initial configuration. The discretization of Equation 11 by the Lagrangian RK approximation requires taking the spatial derivatives of the Lagrangian RK shape function, $\Psi_I(X)$, which is obtained by the chain rule as

$$\frac{\partial \Psi_I(X)}{\partial x_i} = \frac{\partial \Psi_I(X)}{\partial X_j} \frac{\partial X_j}{\partial x_i} = \frac{\partial \Psi_I(X)}{\partial X_j} F_{ji}^{-1} \quad (12)$$

Here, the deformation gradient \mathbf{F} is first computed using the material spatial derivatives of the Lagrangian RK shape functions, and \mathbf{F}^{-1} is then obtained by taking the inversion of \mathbf{F} (instead of computing \mathbf{F}^{-1} directly). However, the Lagrangian formulation breaks down when the inverse of \mathbf{F} is no longer available. This may occur, for example, when large deformation leads to a non-positive definite \mathbf{F} or material separation takes place. Thus, in this research, the semi-Lagrangian RKPM formulation (Guan et al. 2009) used for fragment-impact problems.

Semi-Lagrangian discretization

The Lagrangian formulation breaks down when mapping between the initial and current configurations is no longer one-to-one. This occurs under conditions such as new free surface formation (i.e., material separation) or free surface closure, which commonly exist in penetration processes. Chen and Wu (2007) proposed a semi-Lagrangian formulation to overcome the shortcoming of the Lagrangian formulation.

In the semi-Lagrangian formulation, the RKPM points follow the material motion, while the distance measure $z = x - x(X_I, t)$ in the kernel function is defined in the deformed configuration. Under this construction, the kernel support of the semi-Lagrangian kernel function does not deform with the material motion. The comparison of the supports of Lagrangian and semi-Lagrangian kernels at undeformed and deformed states is shown in Figure 3. The Lagrangian kernel supports cover the same group of material nodes before and after deformation, while the semi-Lagrangian kernel supports cover a different group of nodes after deformation.

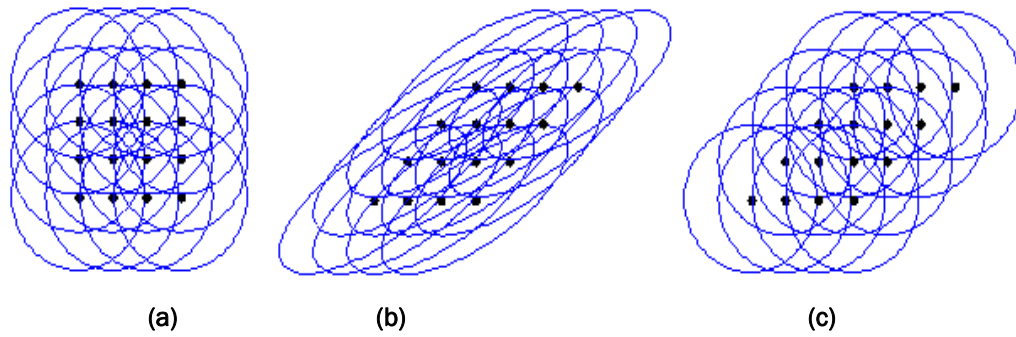


Figure 3. Comparison of Lagrangian and semi-Lagrangian kernel supports in undeformed and deformed configurations: (a) undeformed configuration, (b) Lagrangian kernel deformed with the material in the deformed configuration, and (c) semi-Lagrangian kernel in the deformed configuration.

The semi-Lagrangian RK shape function formulated in the current configuration is expressed as

$$\Psi_I(x) = H^T(x - x(X_I, t))b(x)\varphi_a(x - x(X_I, t)) \quad (13)$$

The coefficient vector $b(x)$ is solved by imposing the semi-Lagrangian reproducing conditions.

$$\sum_{I=1}^{NP} \Psi_I(x) x_1(X_I, t)^i x_2(X_I, t)^j x_3(X_I, t)^k = x_1^i x_2^j x_3^k, \quad i + j + k = 0, 1, \dots, n \quad (14)$$

Solving $b(x)$ from Equation 14 and substituting it into Equation 13 yields the following semi-Lagrangian RK shape function

$$\Psi_I(x) = C(x; x - x(X_I, t))\varphi_a(x - x(X_I, t)) \quad (15)$$

where

$$C(\mathbf{x}; \mathbf{x} - \mathbf{x}(X_I, t)) = \mathbf{H}^T(\boldsymbol{\theta}) \mathbf{M}^{-1}(\mathbf{x}) \mathbf{H}(\mathbf{x} - \mathbf{x}(X_I, t)) \quad (16)$$

$$\mathbf{M}(\mathbf{x}) = \sum_{I=1}^{NP} \mathbf{H}(\mathbf{x} - \mathbf{x}(X_I, t)) \mathbf{H}^T(\mathbf{x} - \mathbf{x}(X_I, t)) \varphi_a(\mathbf{x} - \mathbf{x}(X_I, t)) \quad (17)$$

$$\mathbf{H}^T(\mathbf{x} - \mathbf{x}(X_I, t)) = \begin{bmatrix} 1 & x_1 - x_1(X_I, t) & x_2 - x_2(X_I, t) & \cdots & (x_3 - x_3(X_I, t))^n \end{bmatrix} \quad (18)$$

Let the velocity, v_i , be approximated by semi-Lagrangian RK shape functions.

$$v_i^h(\mathbf{x}, t) = \sum_{I=1}^{NP} \Psi_I(\mathbf{x}) v_{iI}(t) \quad (19)$$

The corresponding semi-Lagrangian approximation of acceleration is given as

$$\ddot{u}_i^h(\mathbf{x}, t) = \dot{v}_i^h(\mathbf{x}, t) = \sum_{I=1}^{NP} (\Psi_I(\mathbf{x}) \dot{v}_{iI}(t) + \Psi_I^*(\mathbf{x}) v_{iI}(t)) \quad (20)$$

where $\Psi_I^*(\mathbf{x})$ is the correction due to the time rate of the semi-Lagrangian kernel $\dot{\varphi}_a$

$$\Psi_I^*(\mathbf{x}) = C(\mathbf{x}; \mathbf{x} - \mathbf{x}(X_I, t)) \dot{\varphi}_a(\mathbf{x} - \mathbf{x}(X_I, t)) \quad (21)$$

$$\dot{\varphi}_a\left(\frac{\|\mathbf{x} - \mathbf{x}(X_I, t)\|}{a}\right) = \varphi_a'\left(\frac{\|\mathbf{x} - \mathbf{x}(X_I, t)\|}{a}\right) \frac{\mathbf{n} \cdot (\mathbf{v} - \mathbf{v}_I)}{a} \quad (22)$$

where $\dot{(\cdot)} = \frac{\partial(\cdot)}{\partial t} \Big|_{[\mathbf{x}]}$ is the material time derivative, and

$$\mathbf{n} = \frac{\mathbf{x} - \mathbf{x}(X_I, t)}{\|\mathbf{x} - \mathbf{x}(X_I, t)\|} \quad (23)$$

Substituting Equation 20 into Equation 11 yields the following semi-Lagrangian discrete equation

$$M\dot{\mathbf{v}} + N\mathbf{v} = \mathbf{f}^{ext} - \mathbf{f}^{int} \quad (24)$$

where

$$\mathbf{M}_{IJ} = \int_{\Omega_x} \rho \Psi_I(\mathbf{x}) \Psi_J(\mathbf{x}) I d\Omega \quad (25)$$

$$\mathbf{N}_{IJ} = \int_{\Omega_x} \rho \Psi_I(\mathbf{x}) \Psi_J^*(\mathbf{x}) I d\Omega \quad (26)$$

$$\mathbf{f}_I^{int} = \int_{\Omega_x} \mathbf{B}_I^T \boldsymbol{\varepsilon} d\Omega \quad (27)$$

$$\mathbf{f}_I^{ext} = \int_{\Omega_x} \Psi_I^T \mathbf{b} d\Omega + \int_{\partial\Omega_x} \Psi_I^T \mathbf{h} d\Gamma \quad (28)$$

where \mathbf{B}_I is the gradient matrix associated with $u_{(i,j)}$, $\boldsymbol{\varepsilon}$ is the stress vector associated with τ_{ij} , and \mathbf{b} and \mathbf{h} are body force and surface traction vectors, respectively.

Stabilized Non-conforming Nodal Integration (SNNI)

Domain integration in Galerkin meshfree methods requires special attention as there is no mesh in the discretization. Gauss integration requires a background grid and introduces significant integration errors if the kernel supports do not match with the integration grid. Nodal integration with stabilization, such as the stabilized conformation nodal integration (SCNI) (Chen et al. 2001; Chen et al. 2002) was proposed as an alternative to the Gauss integration. In SCNI, nodal strain smoothing on a conforming smoothing domain surrounding each node is introduced to achieve stability and optimal convergence. The strain smoothing at the node L is calculated by

$$\bar{\varepsilon}_{ij}(\mathbf{x}_L) = \frac{1}{A_L} \int_{\Omega_L} \varepsilon_{ij} d\Omega = \frac{1}{2A_L} \int_{\Omega_L} (u_{i,j} + u_{j,i}) d\Omega \quad (29)$$

where:

ε_{ij} and $\bar{\varepsilon}_{ij}$ = components of the regular strain and smoothed strain tensors, respectively
 u_i = components of the displacement vector
 A_L = area (or volume) of the conforming smoothing domain associated with node L

By introducing the divergence theorem, the previous equation is transformed to a boundary integral to yield

$$\begin{aligned} \frac{1}{2A_L} \int_{\Omega_L} (u_{i,j} + u_{j,i}) d\Omega &= \frac{1}{2A_L} \int_{\partial\Omega_L} (u_i n_j + u_j n_i) d\Gamma \\ &= \frac{1}{2A_L} \int_{\partial\Omega_L} \sum_{I=1}^{NP} \Psi_I(x) u_{ii} n_j + \sum_{I=1}^{NP} \Psi_I(x) u_{jj} n_i d\Gamma \quad (30) \\ &= \sum_{I=1}^{NP} (\bar{b}_{ij} u_{ii} + \bar{b}_{ji} u_{jj}) \end{aligned}$$

where

$$\bar{b}_{ij} = \frac{1}{A_L} \int_{\partial\Omega_L} \Psi_I(x) n_j d\Gamma \quad (31)$$

In Equation 31, \bar{b}_{ij} is the smoothed gradient of the shape function. Strain smoothing on a conforming smoothing domain, that is, $\cup_L \bar{\Omega}_L = \bar{\Omega}$, is the requirement to satisfy the integration constraint for optimal convergence (Chen et al. 2001). One choice for generation of the conforming smoothing domains is the Voronoi diagram, as shown in Figure 4. However, SCNI comes with the cost of constructing the conforming smoothing domains, and it is particularly tedious in the semi-Lagrangian discretization where smoothing domain reconstruction at every time-step is needed. For penetration problems, the damage evolution and the associated new surface formation further complicate the Voronoi cell generation. In this work, the stabilized non-conforming nodal integration (SNNI) (Chen et al. 2006; Chen and Wu 2007) is introduced. In this approach, the conforming requirement in the nodal strain smoothing domain is not enforced, that is, $\cup_L \bar{\Omega}_L \neq \bar{\Omega}$ as shown in Figure 5, where simple strain smoothing domains are used. RKPM with SNNI remains stable, with accuracy comparable to that with SCNI (Chen et al. 2006; Chen and Wu 2007).

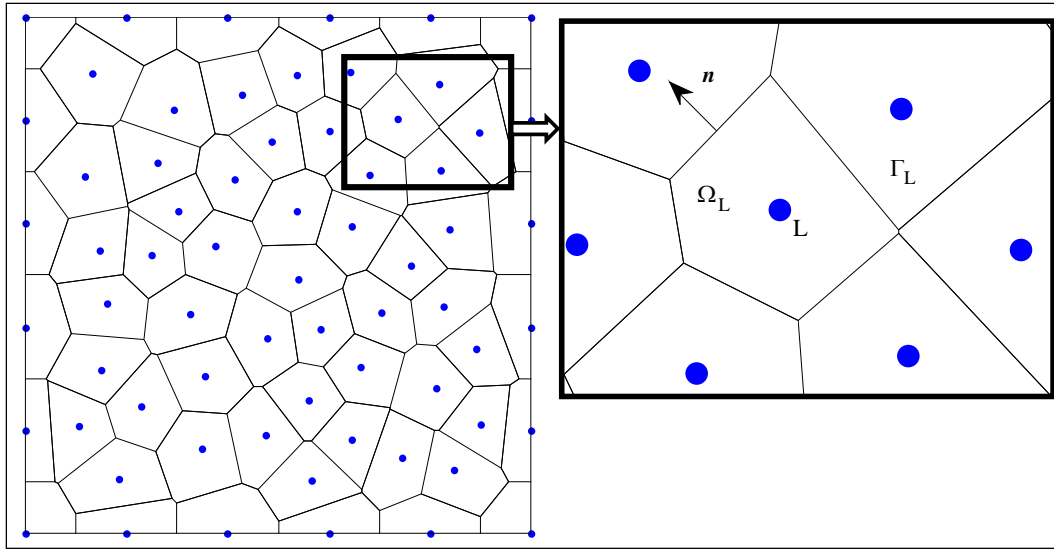


Figure 4. Strain smoothing domains for SCNI.

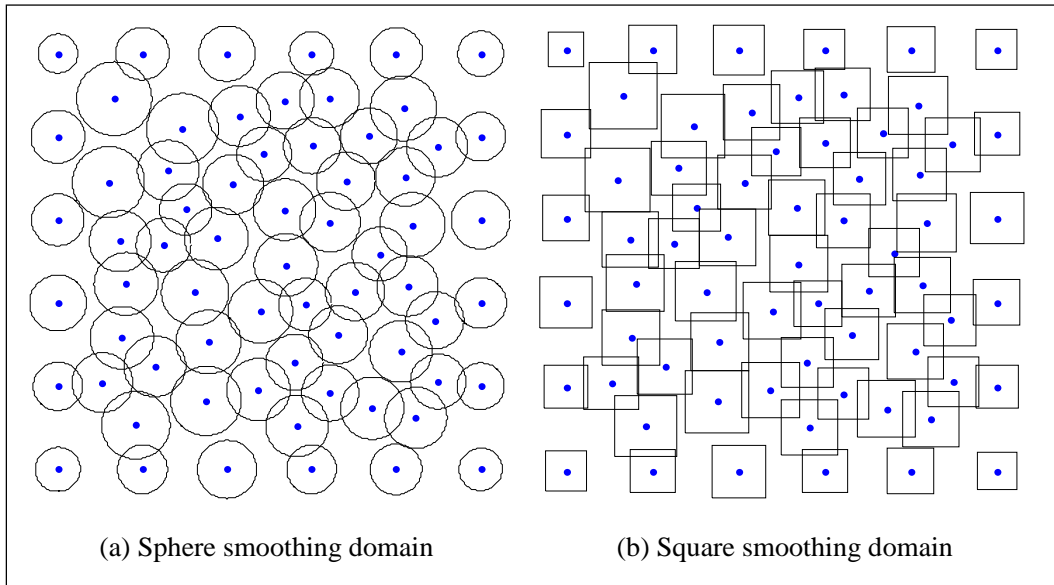


Figure 5. Strain smoothing domains for SNNI.

Boundary correction of SNNI domain integration

How the strain smoothing domains of SNNI should be properly corrected on the problem boundaries are shown here. Consider solving the elastic wave propagation through a three-dimensional (3-D) rod using semi-Lagrangian RKPM with SNNI domain integration. The properties of the rod are: length = 10 m ($0 \leq x \leq 10$), square cross-sectional area ($0 \leq y, z \leq 0.02$), Young's modulus $E = 10000$, Poisson's ratio $\nu = 0$, and density $\rho = 1$. Here the Poisson's effect is purposely removed for the wave to propagate only in the axial direction, while using a 3-D geometry to magnify the boundary

effect. The domain is discretized by $100 \times 3 \times 3$ points in x , y and z directions. The boundary and initial conditions are

$$\begin{aligned} \text{Boundary conditions} & \begin{cases} u_i(x=0, t) = 0 \\ \sigma_{ij} n_j \text{ on all other surfaces} \end{cases} \\ \text{initial condition} & \begin{cases} v_i(x, t=0) = \delta_{i1} \sin\left(\frac{x\pi}{2L}\right) \\ u_i(x, t=0) = 0 \end{cases} \end{aligned} \quad (32)$$

The uncorrected smoothing domains for SNNI are first considered as shown in Figure 6. The displacement and velocity histories at the middle point $x=5$ are plotted in Figure 7. It is observed that the error starts to accumulate when the wave reflects from the boundary, as shown in Figure 7(a). This is attributed to the fact that smoothing domains of the boundary nodes are extended outside of the problem domain. This is corrected by shifting the boundary smoothing domains inward, as shown in Figure 8. The numerical solution with correction of the boundary smoothing domains agrees well with the analytical solution, as shown in Figure 7b.

Temporal stability of semi-Lagrangian RKPM

This section discusses stability of the semi-Lagrangian RKPM formulation. Under the semi-Lagrangian RKPM formulation, the RK shape functions are constructed at every time-step, which allows the particles to transport in and out of the support of each RK shape function. This gives the flexibility to define material contact and separation at the discrete level. Under this construction, the material time derivative of semi-Lagrangian discretized variables is calculated in accordance with Equations 20 through 24, and the discrete equation of motion is given in Equation 24. Considering a central difference temporal discretization, the following full discrete equation is given.

Using the von Neumann stability analysis for a 1-D wave equation discretized by semi-Lagrangian RKPM, the amplification factor can be obtained as follows.

Consider a wave form of the discrete solution $d_i^n = (\lambda)^n e^{ik(I\Delta X)}$, where k is the wave number and λ is the amplification factor. From Equation 33 the the following equation is obtained for the amplification factor (following Guan et al. 2009).

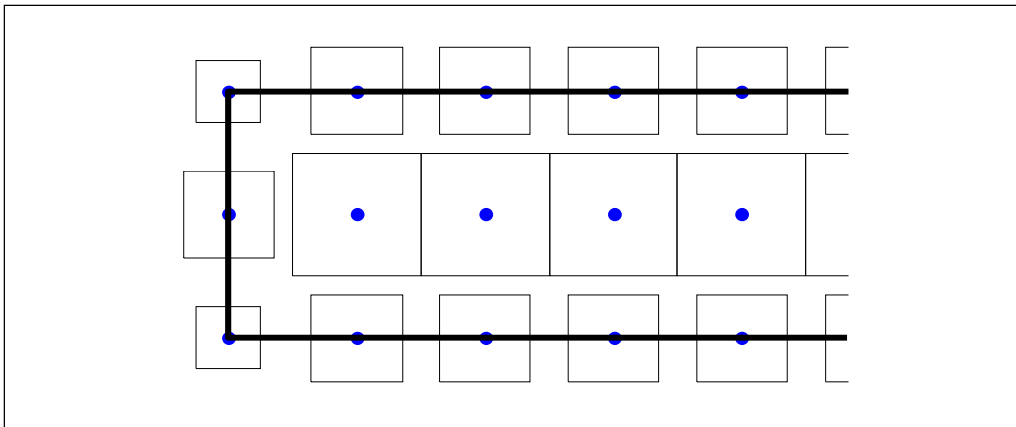


Figure 6. Side view of the smoothing domains on the left end of the rod. Solid thick lines: problem boundary; thin solid lines: boundaries of smoothing domains.

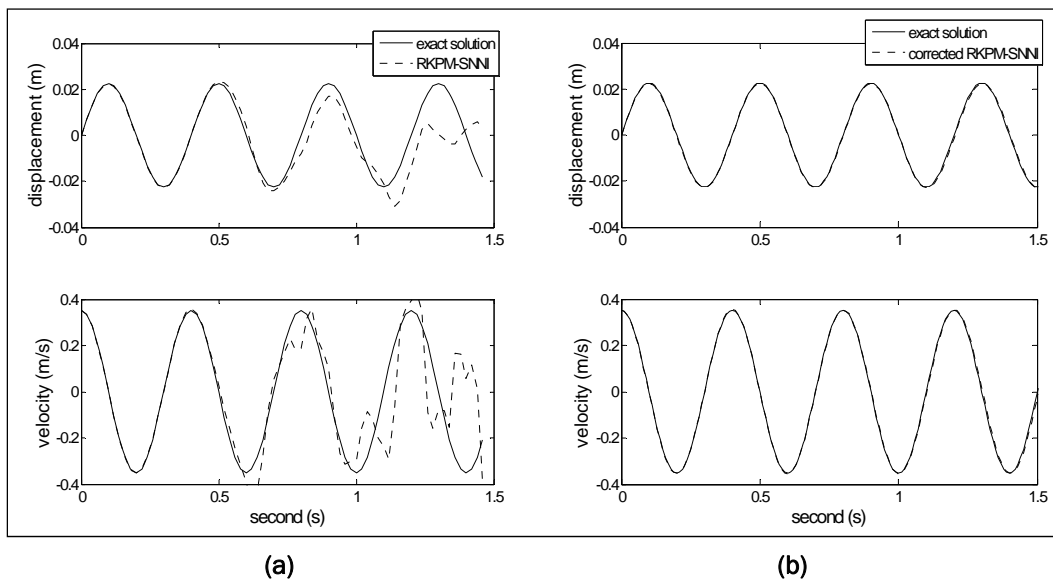


Figure 7. Wave propagation solved by semi-Lagrangian RKPM with SNNI domain integration method: (a) without boundary SNNI smoothing zone correction, (b) with boundary SNNI smoothing zone correction.

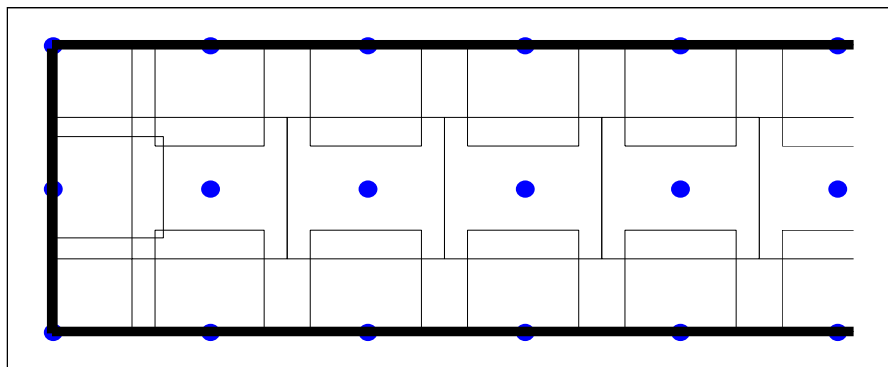


Figure 8. Correction of the boundary smoothing domains.

$$M(d^{n+1} - 2d^n + d^{n-1}) = (\Delta t)^2 \left((f^{ext})^{n+1} - (f^{int})^n - Nv^n \right) \quad (33)$$

$$\begin{aligned} \lambda + 2S_1 + \frac{1}{\lambda} S_2 &= 0 \\ S_1 &= -1 + 2 \frac{\Delta t^2}{\Delta x^2} c^2 A_1 + \rho_I \Delta t \Delta x A_2 \\ S_2 &= 1 - 2\rho_I \Delta x \Delta t \Psi^*(\Delta x) A_2 \\ \Psi^*(\Delta x) &\equiv C(x_I + \Delta x; \Delta x) \phi'_a(\Delta x) \frac{(v_{I+1} - v_I)}{a_I} \end{aligned} \quad (34)$$

Here the coefficients A_1 and A_2 are related to the method of domain integration, and are given in Guan et al. (in preparation) for the case where SNNI is introduced. The contour plot of the amplification factor is shown in Figure 9 for the case where the kernel function support size is chosen to be 1.5 times the nodal distance ($R=1.5$). The temporal stability requires the amplification factor to be bounded by unity, $|\lambda| \leq 1$, as shown in Figure 9, where the horizontal axis is the normalized time-step and the vertical axis is the velocity gradient between two adjacent nodes. The additional parameter α shown in the figure is the ratio between the size of the strain smoothing domain and the nodal distance, Δx . The results show that the stability of semi-Lagrangian RKPM is affected by the velocity gradient. This needs to be considered in the kernel contact algorithms, as will be discussed in Chapter 4.

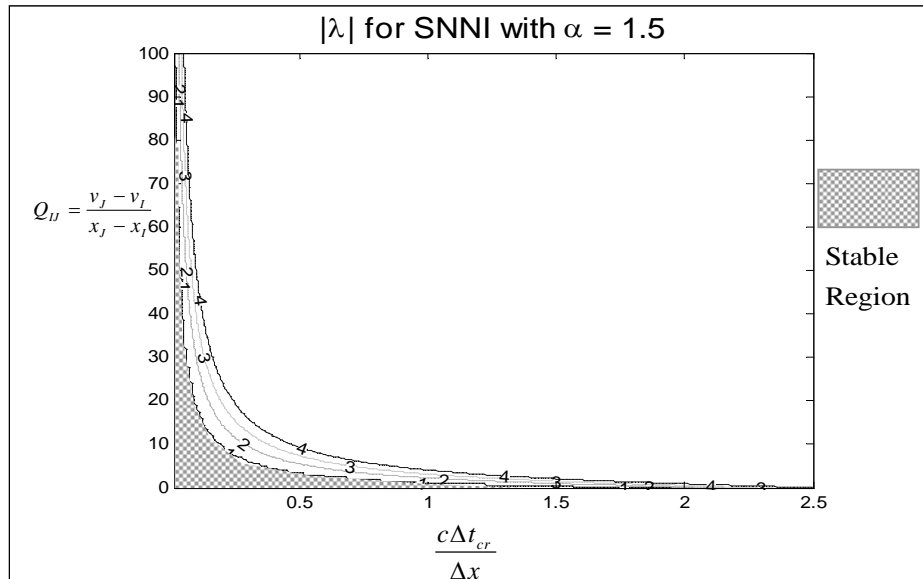


Figure 9. Contour plot of amplification factor of semi-Lagrangian discrete equation with SNNI.

Implementation

In this section, the general coding structure of the transient semi-Lagrangian RKPM formulation is introduced. The flow chart is shown in Figure 10. In semi-Lagrangian RKPM, the shape functions are constructed in the current configuration, which calls for efficient search of neighbors. In this work, a simple bucket search scheme is introduced. Since RK shape functions do not have the kronecker delta property, $\Psi_I(x_J) \neq \delta_{IJ}$, it requires calculation of displacements using shape functions and generalized coordinates (Chen and Wang 2000). By using nodal integration in the semi-Lagrangian RKPM, all state and field variables are stored at nodal points.

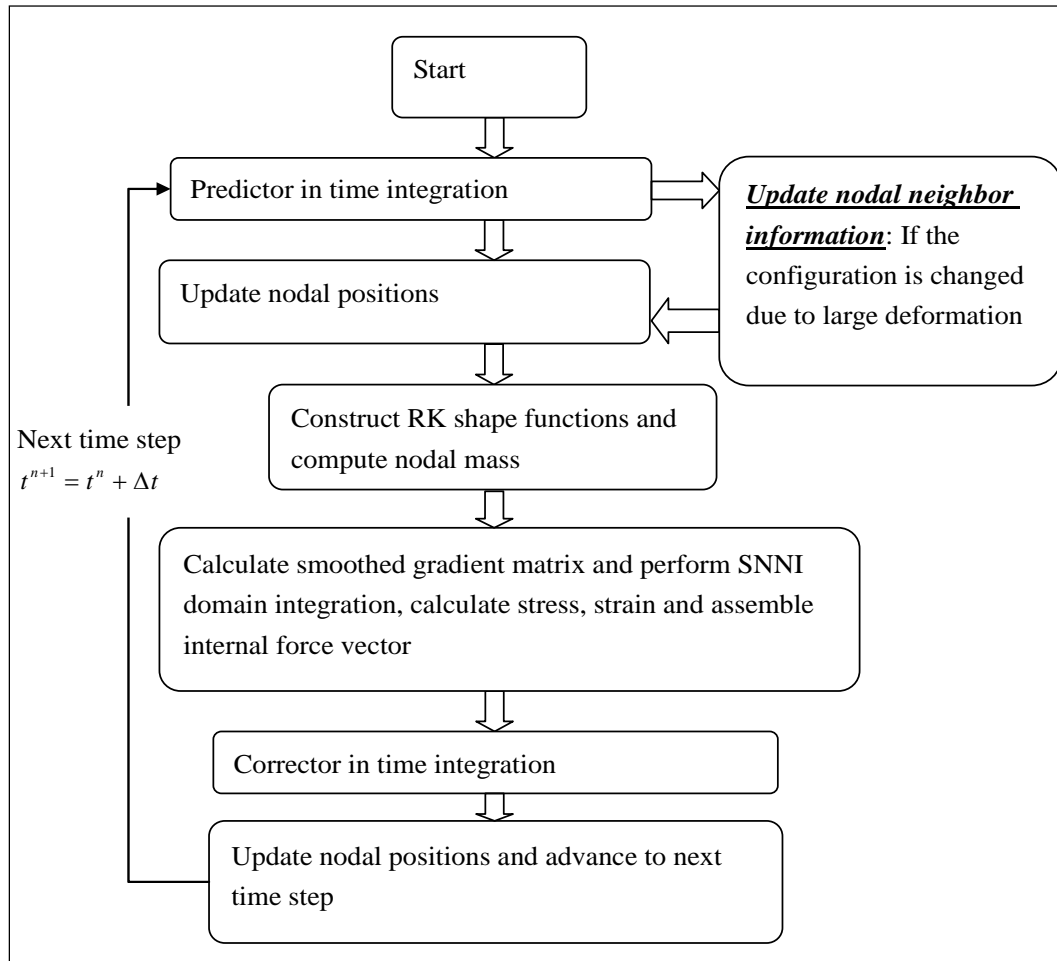


Figure 10. Flow chart of dynamic semi-Lagrangian RKPM code structure.

A major effort in semi-Lagrangian RKPM is the neighbor search at each time-step. Consider a RK approximation of $u(x)$ at x_L , which requires the search of all the nodes whose kernel supports cover x_L as shown in

Figure 11. This group of neighbor nodes for x_L is denoted as $N_L = \{J \mid \varphi_a(x_L - x_J) \neq 0\}$. A two-level bucket search algorithm is introduced. In the first step, nodes located inside a brick domain bounded by $x_L - h$ and $x_L + h$, where $h = (h_x, h_y, h_z)$ with h_i properly selected to be sufficiently larger than the kernel support, are marked as candidate neighbors depicted as open dashed circles in Figure 12. Nodal distances between the candidate neighbors and x_L are then calculated to identify N_L as shown in closed circles in Figure 12. The bucket of candidate neighbors is updated according to the local velocity field in the bucket. As shown in Figure 13, the update time is defined as the time required for the node L to move more than the minimum support size of the candidate neighbors. This requires the velocity of the node L calculated by

$$v(x_L) = \sum_{I \in N_L} \Psi_I(x_L) v_I \quad (35)$$

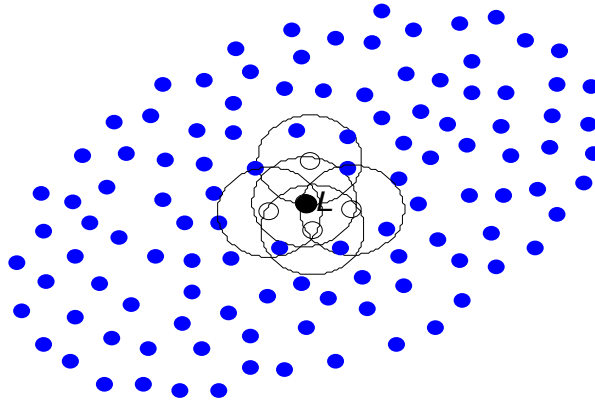


Figure 11. Neighbors of point L marked as black dot.

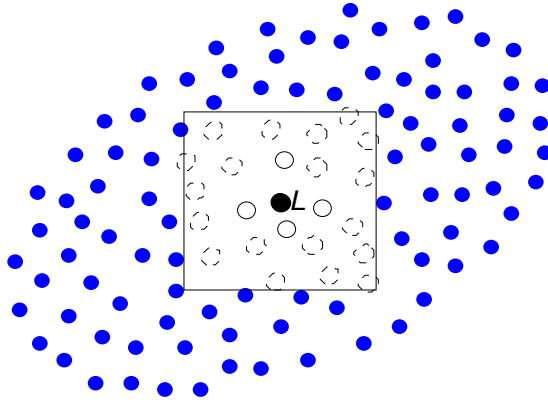


Figure 12. Bucket search of candidate neighbors of point L (open dash circle points).

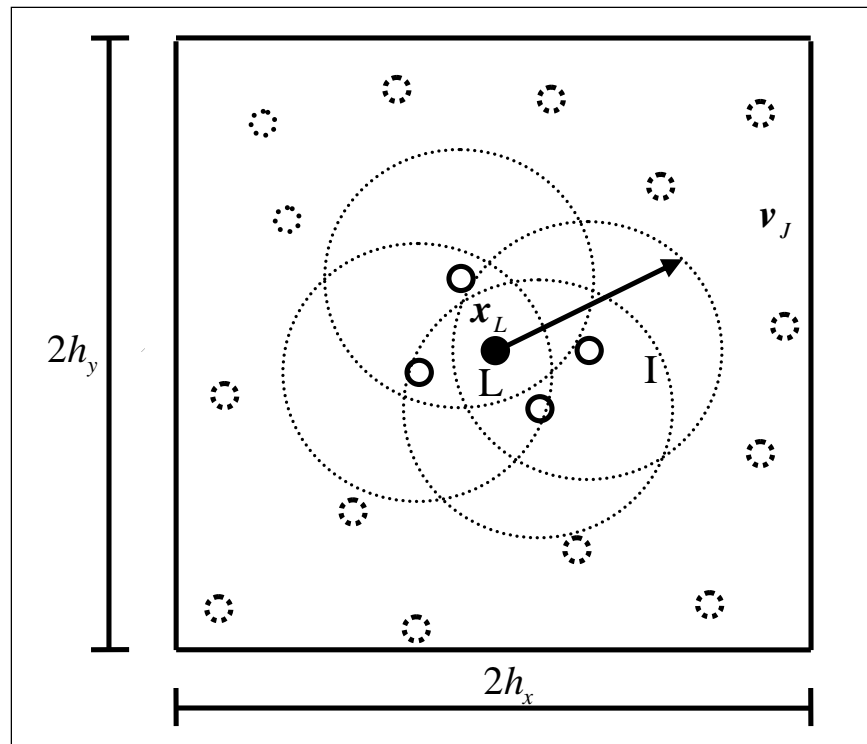


Figure 13. Bucket search scheme and the bucket update.

3 Multiscale Microcrack Informed Damage Model

Damage processes in brittle solids are driven by the distribution of microcracks and their evolution. Explicit modeling of microcracks in brittle solids is computationally infeasible, while classical damage models are phenomenological in nature with a missing link to microscopic properties. A micromechanics-based approach was introduced (Nemat-Nasser and Hori 1999) to obtain homogenized material properties of cracked solids. However, they are limited to certain idealized crack configurations and loading conditions. Alternatively, asymptotic expansion offers a rigorous means for relating physical variables defined at different scales (Bakhvalov and Panasenko 1989; Benssousan 1978; Fish 1997; Guedes and Kikuchi 1990). However, the key step in an asymptotic-type method is solution of the characteristic functions in the microscopic cell, which is typically very time-consuming.

The present work aims at constructing damage models based on thermodynamics of “cracked” microscopic cells and the corresponding “damaged” macroscopic continua. Crack evolution in the microscopic cell is first modeled numerically. Then, corresponding damage evolution functions in the continuum are constructed through a Helmholtz free energy relationship between damaged and undamaged homogenized continua. This approach avoids the tedious solution of characteristic functions in the conventional asymptotic type-methods.

Model problem and homogenization operators

Start with a two-scale representation of the model problem. A heterogeneous solid with domain Ω and boundary Γ containing a distribution of microcracks is considered, as shown in Figure 14. The solid is subjected to surface traction \mathbf{t} on Γ_t and prescribed displacement $\bar{\mathbf{u}}$ on Γ_u , $\Gamma_t \cup \Gamma_u = \Gamma$, and is assumed to undergo static elastic deformation without body force. For a given material point in the macroscopic solid, it corresponds to a microscopic cell microstructure with domain Ω_y containing microcracks with surface, Γ_c . Use \mathbf{x} as the macroscopic coordinate and \mathbf{y} as the microscopic coordinate.

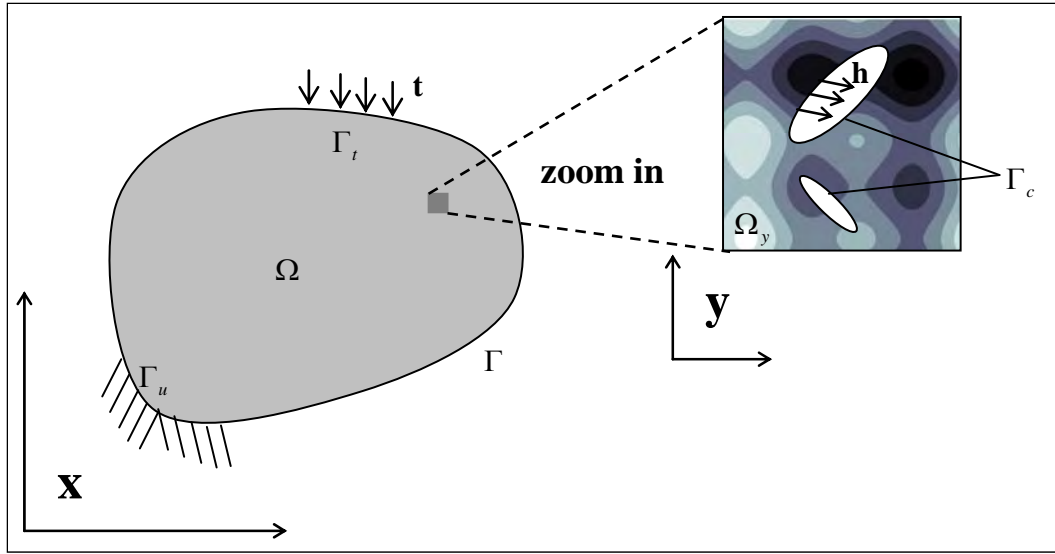


Figure 14. Microscopic and macroscopic structures.

The boundary-value problem is given as

$$\nabla \cdot \boldsymbol{\sigma}^\varepsilon = 0 \quad \text{in } \Omega \quad (36)$$

with the corresponding boundary conditions

$$\boldsymbol{\sigma}^\varepsilon \cdot \mathbf{n} = \mathbf{t} \quad \text{on } \Gamma_t \quad (37)$$

$$\mathbf{u}^\varepsilon = \bar{\mathbf{u}} \quad \text{on } \Gamma_u \quad (38)$$

and the effective traction acting on the crack surface

$$\boldsymbol{\sigma}^\varepsilon \cdot \mathbf{n} = \mathbf{h} \quad \text{on } \Gamma_c \quad (39)$$

where $\boldsymbol{\sigma}^\varepsilon$ is the total stress field, \mathbf{u}^ε is the total displacement field, superscript “ ε ” denotes that the coarse and fine scale responses are embedded in the total solution, \mathbf{n} is the unit outward normal vector on the boundary, and the traction, \mathbf{h} , is applied to the union of crack surfaces, Γ_c

Consider a linear elastic material law

$$\boldsymbol{\sigma}^\varepsilon = \mathbf{C}^\varepsilon : \mathbf{e}^\varepsilon \quad (40)$$

where \mathbf{C}^ε is the heterogeneous constitutive tensor, and \mathbf{e}^ε is the total strain field, where

$$\mathbf{e}^\varepsilon = \frac{1}{2}(\nabla \otimes \mathbf{u}^\varepsilon + \mathbf{u}^\varepsilon \otimes \nabla) \quad (41)$$

Direct simulation of the total scale governing Equations 36 to 39 is time consuming due to the fine-scale microscopic defects and heterogeneities, and an attempt is made to conduct homogenization as shown in Figure 15, where the homogenized stress and strain are defined by the microscopic cell.

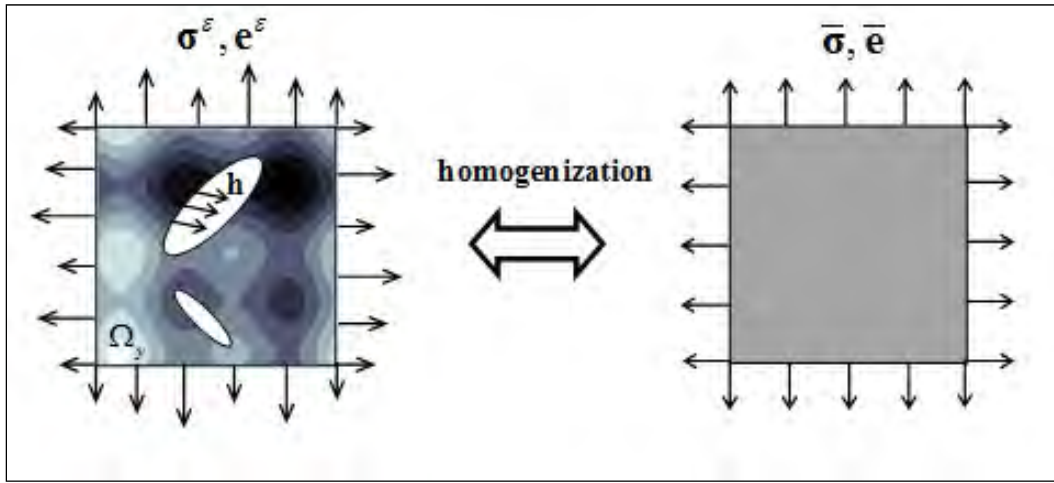


Figure 15. Homogenization of a microscopic cell with fluctuating fields.

The tractions and displacements prescribed on the outer boundary of the microscopic cell, $\partial\Omega_y$, are related to the homogenized stress and strain in the continuum as

$$\bar{\sigma} = \frac{1}{V_y} \oint_{\partial\Omega_y} (\mathbf{t}^\varepsilon \otimes \mathbf{x}) ds \quad (42)$$

$$\bar{\mathbf{e}} = \frac{1}{2V_y} \oint_{\partial\Omega_y} (\mathbf{u}^\varepsilon \otimes \mathbf{n} + \mathbf{n} \otimes \mathbf{u}^\varepsilon) ds \quad (43)$$

where $V_y = \int_{\Omega_y} d\Omega$ is the volume of the microscopic cell. Alternatively, the averaged stress and strain in the microscopic cell are defined as

$$\langle \sigma^e \rangle = \frac{1}{V_y} \int_{\Omega_y} \sigma^e d\Omega \quad (44)$$

$$\langle \mathbf{e}^e \rangle = \frac{1}{V_y} \int_{\Omega_y} \mathbf{e}^e d\Omega \quad (45)$$

where

$$\langle \rangle = \frac{1}{V_y} \int_{\Omega_y} d\Omega \quad (46)$$

The following equation is used to obtain the relationship between homogenized and averaged stresses for the cracked microscopic cell

$$\nabla \cdot (\sigma^e \otimes \mathbf{x}) = \nabla \cdot \sigma^e \otimes \mathbf{x} + \sigma^e \cdot (\nabla \otimes \mathbf{x}) = \sigma^e \quad (47)$$

By substituting Equation 47 into the averaged stress definition in Equation 44, the following equation is used

$$\begin{aligned} \langle \sigma^e \rangle &= \frac{1}{V_y} \int_{\Omega_y} \sigma^e d\Omega = \frac{1}{V_y} \int_{\Omega_y} \nabla \cdot (\sigma^e \otimes \mathbf{x}) d\Omega \\ &= \frac{1}{V_y} \oint_{\partial\Omega_y} (\mathbf{t}^e \otimes \mathbf{x}) ds - \frac{1}{V_y} \oint_{\Gamma_c} (\mathbf{t}^e \otimes \mathbf{x}) ds \\ &= \bar{\sigma} - \frac{1}{V_y} \oint_{\Gamma_c} (\mathbf{t}^e \otimes \mathbf{x}) ds \end{aligned} \quad (48)$$

The second term on the right hand side of Equation 48 vanishes due to equilibrium of the cohesive stresses on the crack surface. Hence, the homogenized stress equals to the averaged stress even in the case of a cracked microscopic cell, that is

$$\bar{\sigma} = \langle \sigma^e \rangle \quad (49)$$

Substituting Equation 41 into averaged strain defined in Equation 45 and considering the divergence theorem, the following is created

$$\begin{aligned}
\langle \mathbf{e}^e \rangle &= \frac{1}{V_y} \int_{\Omega_y} \mathbf{e}^e d\Omega = \frac{1}{2V_y} \int_{\Omega_y} (\nabla \otimes \mathbf{u}^e + \mathbf{u}^e \otimes \nabla) d\Omega \\
&= \frac{1}{2V_y} \oint_{\partial\Omega_y} (\mathbf{u}^e \otimes \mathbf{n} + \mathbf{n} \otimes \mathbf{u}^e) ds - \frac{1}{2V_y} \oint_{\Gamma_c} (\mathbf{u}^e \otimes \mathbf{n} + \mathbf{n} \otimes \mathbf{u}^e) ds \\
&= \bar{\mathbf{e}} - \frac{1}{2V_y} \oint_{\Gamma_c} (\mathbf{u}^e \otimes \mathbf{n} + \mathbf{n} \otimes \mathbf{u}^e) ds
\end{aligned} \tag{50}$$

Consequently the relationship is obtained between homogenized strain and averaged strain as

$$\bar{\mathbf{e}} = \langle \mathbf{e}^e \rangle + \frac{1}{2V_y} \oint_{\Gamma_c} (\mathbf{u}^e \otimes \mathbf{n} + \mathbf{n} \otimes \mathbf{u}^e) ds \tag{51}$$

Here it is shown that the homogenized strain consists of the average strain and the additional strain induced by the displacement jump across the crack surfaces. In other words, macroscopic strain cannot be directly obtained by the averaging of microscopic strain when microcracks exist.

To obtain the homogenized material tensor, the fourth-order influence tensor is defined as

$$\mathbf{e}^e(\mathbf{x}) = [\mathbf{I} - \mathbf{A}^e(\mathbf{x})] : \bar{\mathbf{e}} \tag{52}$$

where \mathbf{I} is the fourth-order identity tensor. Substituting Equation 52 into the stress-strain relation in Equation 40, the following is obtained

$$\boldsymbol{\sigma}^e = \mathbf{C}^e : \mathbf{e}^e = \mathbf{C}^e : [\mathbf{I} - \mathbf{A}^e(\mathbf{x})] : \bar{\mathbf{e}} \tag{53}$$

Using the equivalence between the homogenized stress and averaged stress, obtained is

$$\bar{\boldsymbol{\sigma}} = \langle \mathbf{C}^e : [\mathbf{I} - \mathbf{A}^e(\mathbf{x})] \rangle : \bar{\mathbf{e}} \equiv \bar{\mathbf{C}} : \bar{\mathbf{e}} \tag{54}$$

From the previous equation, the homogenized material response tensor is expressed as

$$\bar{\mathbf{C}} = (\mathbf{I} - \mathbf{D}) : \langle \mathbf{C}^e \rangle \tag{55}$$

where

$$\mathbf{D} = \langle \mathbf{C}^\varepsilon : \mathbf{A}^\varepsilon \rangle : \langle \mathbf{C}^\varepsilon \rangle^{-1} \quad (56)$$

Here \mathbf{D} is a degradation (damage) tensor expressed by the influence tensor, $\mathbf{A}^\varepsilon(\mathbf{x})$.

Remark 3.1

The fourth-order influence tensor $\mathbf{A}^\varepsilon(\mathbf{x})$ represents the interscale relation between properties of the cracked microstructures and properties of the homogenized continua. Micromechanics offer an analytical basis for obtaining the influence tensor, for example, Mori-Tanaka method (Mori and Tanaka 1973), self-consistent method (Budiansky and O'Connell 1976), and differential scheme (Norris 1985). On the other hand, asymptotic expansion based homogenization offers a general approach for calculating the influence tensor, which utilizes the numerical solution of characteristic functions for scale-coupling in the microscopic cell.

Remark 3.2

Using the asymptotic expansion based method, the influence tensor can be obtained from the characteristic tensor $\chi(\mathbf{y})$ as (see Appendix A for detailed derivations)

$$\mathbf{A}^\varepsilon = -\nabla_y^s \chi(\mathbf{y}) \quad (57)$$

where the characteristic tensor $\chi(\mathbf{y})$ is solved from the following boundary-value problem defined in the microscopic cell.

$$\nabla_y \cdot (\mathbf{C}^\varepsilon : \nabla_y^s \chi(\mathbf{y})) = 0 \quad \text{in } \Omega_y \quad (58)$$

$$[\mathbf{C}^\varepsilon : \nabla_y^s \chi(\mathbf{y}) : \nabla_x^s \mathbf{v}^{[0]}(\mathbf{x})] \cdot \mathbf{n} = -[\mathbf{C}^\varepsilon : \nabla_x^s \mathbf{v}^{[0]}(\mathbf{x})] \cdot \mathbf{n} + \mathbf{h} \quad \text{on } \Gamma_c \quad (59)$$

Clearly the numerical solution of the previous boundary-value problem for obtaining the third-order tensor $\chi(\mathbf{y})$ is computationally intensive. This issue is addressed by introducing the energy bridging method as discussed in the next section.

Energy bridging between scales

To establish the relationship between the microcracks induced material degradation and the damaged continuum described by conventional damage mechanics, the Helmholtz free energy (HFE) is employed.

$$\bar{\Psi} = \frac{1}{2} \bar{\sigma} : \bar{\mathbf{e}} \quad (60)$$

According to the second principle of thermodynamics, is

$$\bar{\sigma} = \frac{\partial \bar{\Psi}}{\partial \bar{\mathbf{e}}} \quad (61)$$

$$\mathbf{Y} = - \frac{\partial \bar{\Psi}}{\partial \mathbf{D}} \quad (62)$$

where \mathbf{D} is the damage tensor and \mathbf{Y} is the damage energy release rate (DERR) representing a driving force of damage evolution. Consequently, the damage evolution equation is expressed by the evolution potential, Φ , as

$$\dot{\mathbf{D}} = \dot{\lambda} \frac{\partial \Phi}{\partial \mathbf{Y}} \quad (63)$$

where λ is the consistency parameter. In conventional continuum damage mechanics, HFE is determined experientially. In the present approach, the HFE is obtained through homogenization of the cracked microstructure. The microscopic free energy is defined as

$$\Psi^e = \frac{1}{2} \sigma^e : \mathbf{e}^e \quad (64)$$

where σ^e and \mathbf{e}^e are the microscopic stress and strain. Integrating microscopic HFE in the microscopic cell yields

$$\begin{aligned}
\int_{\Omega_y} \Psi^e d\Omega &= \frac{1}{2} \int_{\Omega_y} \sigma^e : \epsilon^e d\Omega \\
&= \frac{1}{2} \int_{\Omega_y} \frac{1}{2} \sigma^e : (\nabla \otimes \mathbf{u}^e + \mathbf{u}^e \otimes \nabla) d\Omega \\
&= \frac{1}{2} \int_{\Omega_y} \frac{1}{2} [\nabla \cdot (\mathbf{u}^e \cdot \sigma^e) + \nabla \cdot (\sigma^e \cdot \mathbf{u}^e) - \mathbf{u}^e \cdot \nabla \cdot \sigma^e - \nabla \cdot \sigma^e \cdot \mathbf{u}^e] d\Omega \\
&= \frac{1}{2} \int_{\Omega_y} \nabla \cdot (\mathbf{u}^e \cdot \sigma^e) d\Omega
\end{aligned} \tag{65}$$

Note that equilibrium was used without body force. Introducing the divergence theorem in Equation 65 results in

$$\begin{aligned}
\int_{\Omega_y} \Psi^e d\Omega &= \frac{1}{2} \int_{\Omega_y} \nabla \cdot (\mathbf{u}^e \cdot \sigma^e) d\Omega \\
&= \frac{1}{2} \oint_{\partial\Omega_y} \mathbf{u}^e \cdot \sigma^e \cdot \mathbf{n} ds - \frac{1}{2} \int_{\Gamma_c} \mathbf{u}^e \cdot \sigma^e \cdot \mathbf{n} ds \\
&= \frac{1}{2} \oint_{\partial\Omega_y} \mathbf{u}^e \cdot \mathbf{t}^e ds - \frac{1}{2} \oint_{\Gamma_c} \mathbf{u}^e \cdot \mathbf{h} ds
\end{aligned} \tag{66}$$

Here a strain driven homogenization is considered, where the displacement boundary conditions obtained from macroscopic strain are applied to the microscopic cell to compute the local stress field. The local stress field is then averaged, which is the same as the homogenized stress $\bar{\sigma}$ according to Equation 49, and is passed back to the coarse scale. The prescribed boundary displacements on the microscopic cell are obtained from the macroscopic strain by

$$\mathbf{u}^e = \bar{\epsilon} \cdot \mathbf{x} \text{ on } \partial\Omega_y \tag{67}$$

where $\partial\Omega_y$ is the outer boundary of the microscopic cell. Substituting Equation 67 into the first term on the right hand side of Equation 66 is

$$\begin{aligned}
\frac{1}{2} \oint_{\partial\Omega_y} \mathbf{u}^e \cdot \mathbf{t}^e \, ds &= \frac{1}{2} \oint_{\partial\Omega_y} (\bar{\mathbf{e}} \cdot \mathbf{x}) \cdot \mathbf{t}^e \, ds \\
&= \frac{1}{2} \left[\oint_{\partial\Omega_y} (\mathbf{t}^e \otimes \mathbf{x}) \, ds \right] : \bar{\mathbf{e}} \\
&= \frac{V_y}{2} \bar{\boldsymbol{\sigma}} : \bar{\mathbf{e}} = V_y \bar{\Psi}
\end{aligned} \tag{68}$$

Combining Equations 66 and 68 is

$$\bar{\Psi} = \frac{1}{V_y} \left(\int_{\Omega_y} \Psi^e \, d\Omega + \frac{1}{2} \oint_{\Gamma_c} \mathbf{u}^e \cdot \mathbf{h} \, ds \right) \tag{69}$$

The right hand side of Equation 69 is the averaged free energy of the microscopic cell, while the left hand side of Equation 69 is the energy density of the homogenized material. Thus, Equation 69 concludes that the averaged energy of the microscopic cell is equal to the energy density of the homogenized material.

Remark 3.3

The result in Equation 69 is an extension of Hill's theorem (Hill 1963), with addition of the second term on the right hand side resulting from the crack discontinuous displacement field. This result is consistent with the one obtained by (Belytschko et al. 2008) where the power expression of the energy bridging equation was introduced. Further, the energy equivalence in Equation 69 can also be obtained by the asymptotic expansion approach as detailed in Appendix B.

Characterization of parameters in continuum damage mechanics by energy bridging

The Helmholtz free energy relationship is used between the homogenized continuum and the cracked microstructure to derive damage parameters for several commonly used damage models.

One-parameter scalar damage model

The one-parameter damage model (Mazars 1984) is expressed as

$$\bar{\Psi} = (1 - d)\Psi_0 \quad (70)$$

where $\bar{\Psi}$ is Helmholtz free energy computed from the microscopic cell in Equation 69, and Ψ_0 is the effective Helmholtz free energy obtained by

$$\Psi_0 = \frac{1}{2} \bar{\mathbf{e}} : \bar{\mathbf{C}}_0 : \bar{\mathbf{e}} \quad (71)$$

where $\bar{\mathbf{C}}_0$ is the homogenized undamaged material tensor. Then the damage scalar is obtained by

$$d = 1 - \frac{\bar{\Psi}}{\Psi_0} \quad (72)$$

Two-parameter damage model

The two-parameter damage model was extensively studied and widely adopted for description of more complicated damage mechanisms (Faria et al. 1998; Li and Ren 2009; Wu et al. 2006). For geological materials such as sand or soil, the volumetric-deviatoric splitting approach was adopted to describe damage mechanisms driven by pressure and shear. On the other hand, the hydrostatic tension-compression decomposition approach was used for quasi-brittle materials such as concrete and rock (Faria et al. 1998), which is the case demonstrated herein. The framework of the two-parameter damage model is described in Appendix C.

The initially undamaged macroscopic stress is obtained as

$$\bar{\boldsymbol{\sigma}}_0 = \bar{\mathbf{C}}_0 : \bar{\mathbf{e}} \quad (73)$$

The macroscopic stress can be decomposed as

$$\bar{\boldsymbol{\sigma}}_0 = \bar{\boldsymbol{\sigma}}_0^+ + \bar{\boldsymbol{\sigma}}_0^- \quad (74)$$

where $\bar{\boldsymbol{\sigma}}_0^+$ and $\bar{\boldsymbol{\sigma}}_0^-$ are the tensile and compressive stresses, respectively, defined as

$$\bar{\boldsymbol{\sigma}}_0^+ = \sum_i \hat{\sigma}_i H(\hat{\sigma}_i) \mathbf{p}_i \otimes \mathbf{p}_i \quad (75)$$

$$\bar{\sigma}_0^- = \bar{\sigma}_0 - \bar{\sigma}_0^+ \quad (76)$$

where $\hat{\sigma}_i$ and \mathbf{p}_i are the i^{th} eigenvalue and the corresponding eigenvector of $\bar{\sigma}_0$, and $H(\cdot)$ is the Heaviside function.

The macroscopic Helmholtz free energy is then expressed as

$$\bar{\Psi} = (1 - d^+) \Psi_0^+ + (1 - d^-) \Psi_0^- \quad (77)$$

where d^+ and d^- are tensile and compressive damage parameters, respectively, and the corresponding expressions of the effective Helmholtz free energy are

$$\Psi_0^\pm = \frac{1}{2} \bar{\sigma}_0^\pm : \bar{\mathbf{C}}_0^{-1} : \bar{\sigma}_0^\pm \quad (78)$$

Considering the Clausius-Duhem inequality of irreversible thermodynamics, the following can be derived from the Helmholtz free energy in Equation 77

$$Y^\pm = \Psi_0^\pm \quad (79)$$

and

$$d^\pm = 1 - \frac{\partial \bar{\Psi}}{\partial Y^\pm} \approx 1 - \frac{\Delta \bar{\Psi}}{\Delta Y^\pm} \quad (80)$$

where $\bar{\Psi}$ is the Helmholtz free energy calculated from the microscopic cell in Equation 69. By using the finite difference operation in Equation 80, the evolution of damage parameters is obtained.

Fully tensorial damage model

Derivation of the tensorial damage tensor based on the influence tensor $\mathbf{A}^\varepsilon(\mathbf{x})$ according to Equation 56 is limited to special cases if $\mathbf{A}^\varepsilon(\mathbf{x})$ is obtained by the micromechanical methods, and is costly if $\mathbf{A}^\varepsilon(\mathbf{x})$ is calculated using the asymptotic expansion method. By introducing bridging based on Helmholtz free energy, a more efficient approach for

obtaining the damage tensor is introduced. Recalling the definition of the macroscopic Helmholtz free energy in Equation 60 the following appears

$$\bar{\Psi} = \frac{1}{2} \bar{\mathbf{e}} : (\mathbf{I} - \mathbf{D}) : \bar{\mathbf{C}}_0 : \bar{\mathbf{e}} \quad (81)$$

Performing partial differentiation of the Helmholtz free energy in Equation 81 with respect to the fourth-order damage tensor, \mathbf{D} , the damage energy release rate is obtained as

$$\mathbf{Y} = -\frac{\partial \bar{\Psi}}{\partial \mathbf{D}} = \frac{1}{2} \bar{\mathbf{e}} : \bar{\mathbf{C}}_0 : \bar{\mathbf{e}} \quad (82)$$

By taking the derivative of the Helmholtz free energy of the microscopic cell in Equation 69 with respect to the damage energy release rate, \mathbf{Y} , the fourth-order damage tensor is obtained.

$$\mathbf{D} = \mathbf{I} - \frac{\partial \bar{\Psi}}{\partial \mathbf{Y}} \approx \mathbf{I} - \frac{\Delta \bar{\Psi}}{\Delta \mathbf{Y}} \quad (83)$$

Here a finite difference approach could be used in Equation 83 to obtain the fourth-order damage tensor using $\Delta \bar{\Psi}$ and $\Delta \mathbf{Y}$.

Microscopic cell analysis

The essential step in obtaining the damage evolution functions in the proposed method is the microscopic cell analysis. In the present study, the microscopic cell is made of an isotropic linear elastic material with a center crack subjected to boundary conditions as shown in Figure 14. The boundary conditions on the microscopic cell are defined based on the type of damage mechanisms to be captured. The crack is modeled by a cohesive crack model with linear degradation as shown in Figure 14. The crack propagation direction is determined by the maximum hoop stress criterion.

In this work, we consider an enriched reproducing kernel particle method (RKPM) for the microscopic cell analysis. The microscopic cell solution is then used in the homogenization as previously described for characterization of the damage parameter evolution.

In RKPM (Chen et al. 1996; Liu 1995), the approximation of a function u is expressed as

$$u^h(\mathbf{x}) = \sum_I \phi_I(\mathbf{x}) u_I \quad (84)$$

where $\phi_I(\mathbf{x})$ is the reproducing kernel (RK) shape function and u_I is the corresponding coefficient. In the following equations, we use multi-dimensional notation: $\alpha = (\alpha_1, \alpha_2, \dots, \alpha_d)$, $|\alpha| = \sum_{i=1}^d \alpha_i$, $\mathbf{x}^\alpha = x_1^{\alpha_1} \cdots x_d^{\alpha_d}$, $\mathbf{x}_I^\alpha = x_{1I}^{\alpha_1} \cdots x_{dI}^{\alpha_d}$, and d is the spatial dimension. The RK shape functions are constructed using monomials as basis functions expressed as

$$\phi_I(\mathbf{x}) = \varphi_a(\mathbf{x} - \mathbf{x}_I) \left(\sum_{|\alpha| \leq n} (\mathbf{x} - \mathbf{x}_I)^\alpha b_\alpha(\mathbf{x}) \right) \quad (85)$$

where $\varphi_a(\mathbf{x} - \mathbf{x}_I)$ is the kernel function with support size a , $\{(\mathbf{x} - \mathbf{x}_I)^\alpha\}_{|\alpha| \leq n}$ is the set of monomial basis functions, and $\{b_\alpha(\mathbf{x})\}_{|\alpha| \leq n}$ are the coefficients of the basis functions obtained by imposing the following reproducing conditions

$$\sum_I \phi_I(\mathbf{x}) \mathbf{x}_I^\alpha = \mathbf{x}^\alpha, \quad |\alpha| \leq n \quad (86)$$

Obtaining $b_\alpha(\mathbf{x})$ from Equation 86, the RK shape function is constructed

$$\phi_I(\mathbf{x}) = \mathbf{H}^T(\mathbf{0}) \mathbf{M}^{-1}(\mathbf{x}) \mathbf{H}^T(\mathbf{x} - \mathbf{x}_I) \varphi_a(\mathbf{x} - \mathbf{x}_I) \quad (87)$$

where $\mathbf{H}(\mathbf{x}) = \{\mathbf{x}^\alpha\}_{|\alpha| \leq n} = \{1, x_1, \dots, x_d^n\}$ is the vector containing all the basic functions and \mathbf{M} is the moment matrix defined as

$$\mathbf{M}(\mathbf{x}) = \sum_I \mathbf{H}(\mathbf{x} - \mathbf{x}_I) \mathbf{H}^T(\mathbf{x} - \mathbf{x}_I) \varphi_a(\mathbf{x} - \mathbf{x}_I) \quad (88)$$

To consider enrichment of RKPM by a set of enrichment functions, $p_i(\mathbf{x})$, the following reproducing conditions are introduced (Fleming et al. 1997)

$$Q_i(\mathbf{x}) = \sum_I \phi_I(\mathbf{x}) Q_i(\mathbf{x}_I) + p_i(\mathbf{x}) \quad (89)$$

where $Q_i(\mathbf{x})$ is the target function and $p_i(\mathbf{x})$ is the corresponding enrichment. The enrichment is thus expressed as

$$p_i(\mathbf{x}) = Q_i(\mathbf{x}) - \sum_I \phi_I(\mathbf{x}) Q_i(\mathbf{x}_I) \quad (90)$$

The enriched RKPM is given in the following form

$$u^h(\mathbf{x}) = \sum_I \phi_I(\mathbf{x}) u_I + \sum_i k_i \left\{ Q_i(\mathbf{x}) - \sum_I \phi_I(\mathbf{x}) Q_i(\mathbf{x}_I) \right\} \quad (91)$$

For the microscopic cell analysis, the following target functions for enrichment of the crack tip solution (Moes and Belytschko 2002) are considered

$$\begin{cases} [Q_1, Q_2, Q_3, Q_4] = \left[\sqrt{r} \sin\left(\frac{\theta}{2}\right), \sqrt{r} \cos\left(\frac{\theta}{2}\right), \sqrt{r} \sin\left(\frac{\theta}{2}\right) \sin\theta, \sqrt{r} \cos\left(\frac{\theta}{2}\right) \sin\theta \right] & \text{for LEFM} \\ [Q_1, Q_2, Q_3] = \left[r \sin\left(\frac{\theta}{2}\right), r^{\frac{3}{2}} \sin\left(\frac{\theta}{2}\right), r^2 \sin\left(\frac{\theta}{2}\right) \right] & \text{for Cohesive Crack Model} \end{cases} \quad (92)$$

The functional for the microscopic cell problem is expressed as

$$\Pi = \frac{1}{2} \int_{\Omega_y} \varepsilon_{ij} C_{ijkl} \varepsilon_{kl} d\Omega - \int_{\Gamma_t} u_i \bar{t}_i d\Gamma + \frac{\alpha}{2} \int_{\Gamma_u} (u_i - \bar{u}_i)(u_i - \bar{u}_i) d\Gamma \quad (93)$$

where α is the penalty parameter for imposing the essential boundary conditions. Introducing the enriched RK approximation in Equation 91 into the stationary condition of Equation 93, we have

$$(\mathbf{K} + \alpha \mathbf{K}_u) \mathbf{U} = \mathbf{f} + \alpha \mathbf{f}_u \quad (94)$$

where \mathbf{K} is the stiffness matrix, \mathbf{f} is the force vector, and \mathbf{K}_u and \mathbf{f}_u are the terms associated with imposition of essential boundary conditions. For the simulation of solids, the penalty parameter α is chosen to be $10^3 - 10^6 E$ where E is the elastic modulus.

Numerical examples

In the aforementioned homogenization calculation of damage parameters, modeling of the microscopic cell with microcracks propagation is first

performed. The microscopic cell analysis results are then processed according to the given homogenization procedures to obtain the evolution of damage parameters. It is noted that the homogenized damage evolution functions need to be properly scaled with respect to the ratio between dimensions of the microscopic cell and mesh to avoid the “numerical size effect.” This is discussed in the following section.

A notched beam under three point bending, as shown in Figure 16, is to be modeled by the proposed methods. This problem was extensively studied both experimentally (Petersson 1981) and numerically (de Borst 1986; Meyer et al. 1994). The overall behavior of the beam is governed by the Mode I crack initiated at the vertex of the notch. Hence the microscopic cell model with an evolving Mode I crack is considered for generation of the damage evolution function. In this example, we consider the two-parameter damage model as previously given with the compressive damage evolution suppressed due to the bending condition and moderate beam thickness. The material properties for elastic modulus and Poisson’s ratio are 30 GPa and 0.2, respectively. Tensile strength of the material is $f_u = 3.33$ MPa, and fracture energy of the cohesive crack is $G_f = 124$ N/m (de Borst 1986).

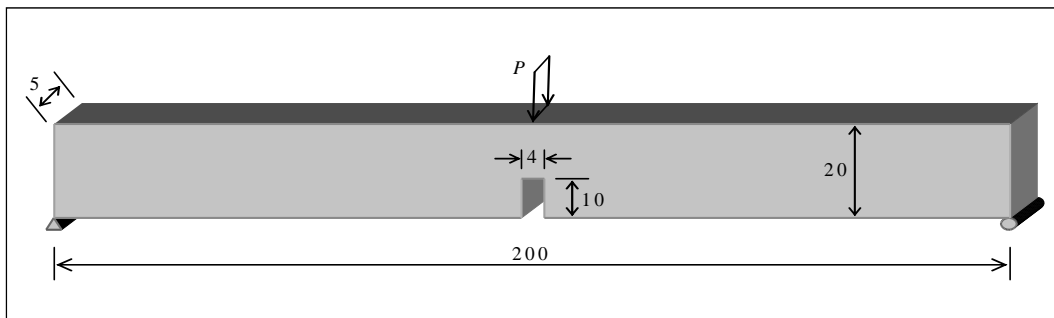


Figure 16. Notched beam subjected to three-point bending (unit: cm).

Characterization of damage evolution functions

The microscopic cell geometry with initial crack and boundary conditions are shown in Figure 17. We consider a microscopic cell subjected to uniform tension with a centered-crack propagating perpendicular to the loading direction. In this study, the initial crack length is set to be one-tenth of the microscopic cell dimension. Based on the numerical method described earlier, we first obtain the stress and strain fields in the microscopic cell at different loading stages. Normal stresses in the direction of loading at different stages of crack propagation are shown in Figure 18. The homogenized stress and strain are shown in Figure 19(a).

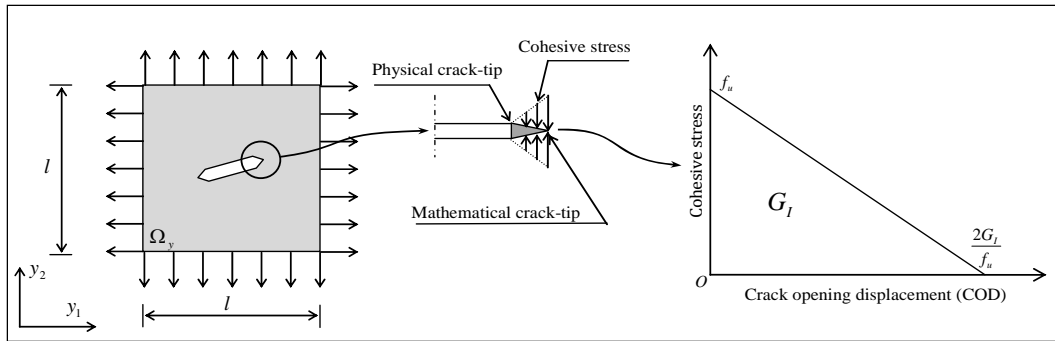


Figure 17. Microscopic cell problem and cohesive crack model.

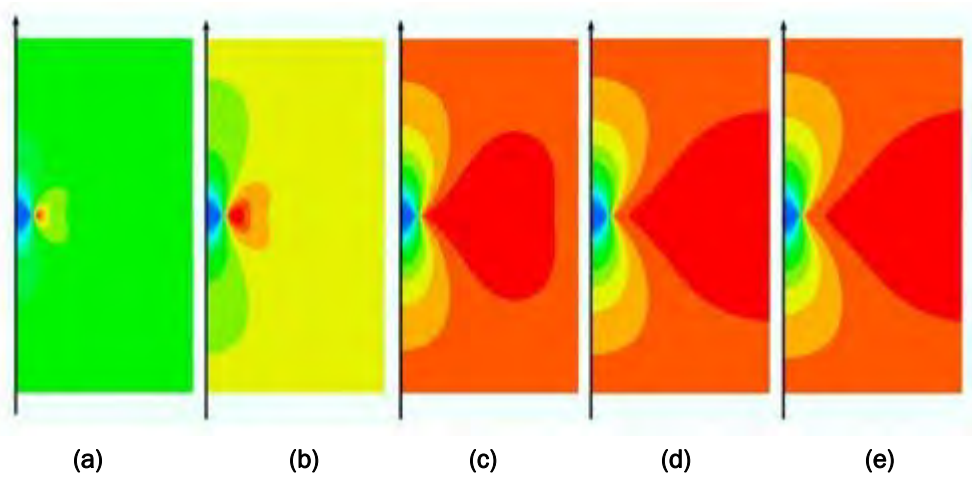


Figure 18. Normal stress contours (in direction of loading) at different loading stages.

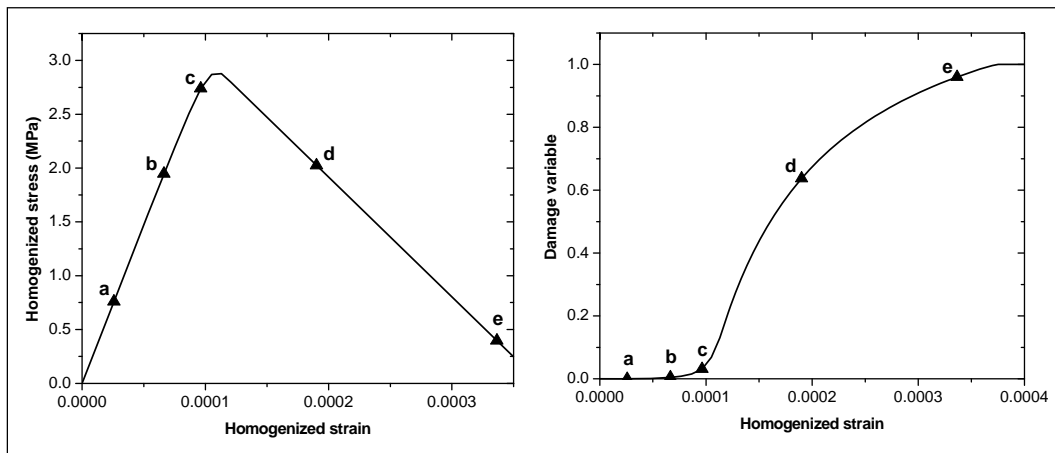


Figure 19. (a) Homogenized stress and strain and (b) tensile damage parameter calculated by the microscopic stress and strain fields, where a, b, c, d and e denote the corresponding homogenized stresses, strains and damage parameters calculated based on the stress fields (a), (b), (c), (d) and (e) shown in Figure 18, respectively.

The energy bridging Equation 69 is employed to calculate the damage variable as a function of deformation as previously discussed. The homogenized tensile damage evolution is shown in Figure 19(b).

Here we study the size effect by considering various sizes of microscopic cells which correspond to structural models with coarse, medium and fine meshes. For this purpose, define a dimensionless parameter, λ , as the ratio between the microscopic length parameter, l_{mic} , and the macroscopic length parameter, l_{mac} . Here we consider the dimension of the microscopic cell, l , and height of the beam, h , as the two scale parameters and define their ratio as

$$\lambda = \frac{l_{mic}}{l_{mac}} = \frac{l}{h} \quad (95)$$

It is observed in Figure 20 that the homogenized stress-strain curves are strongly affected by the size of the microscopic cell. The cohesive law employed in the microscopic analysis of crack propagation involves a length scale, which is the crack opening displacement that corresponds to zero stress ($2G_c / f$ in Figure 17), called the critical crack opening displacement. This length scale does not scale with the microscopic cell, and thus leads to different homogenized stress-strain curves based on different cell dimensions. As the cell dimension increases, the homogenized strain corresponding to the critical crack opening displacement decreases, and yields strain softening with a larger negative slope as shown in Figure 20. Computationally, the macroscopic mesh dimension is used to represent the averaged material behavior within the mesh. Thus, if a cohesive law is used in a microscopic cell for obtaining the homogenized stress-strain curve for a macroscopic calculation, the corresponding microscopic cell dimension needs to be dimensionally equivalent to the mesh dimension when strain softening exists. Unfortunately this is practically tedious for arbitrary mesh geometry. Therefore, a scaling law will be introduced in the following section so that the homogenized stress-strain curves for different mesh points are scaled based on a “reference microscopic cell analysis.”

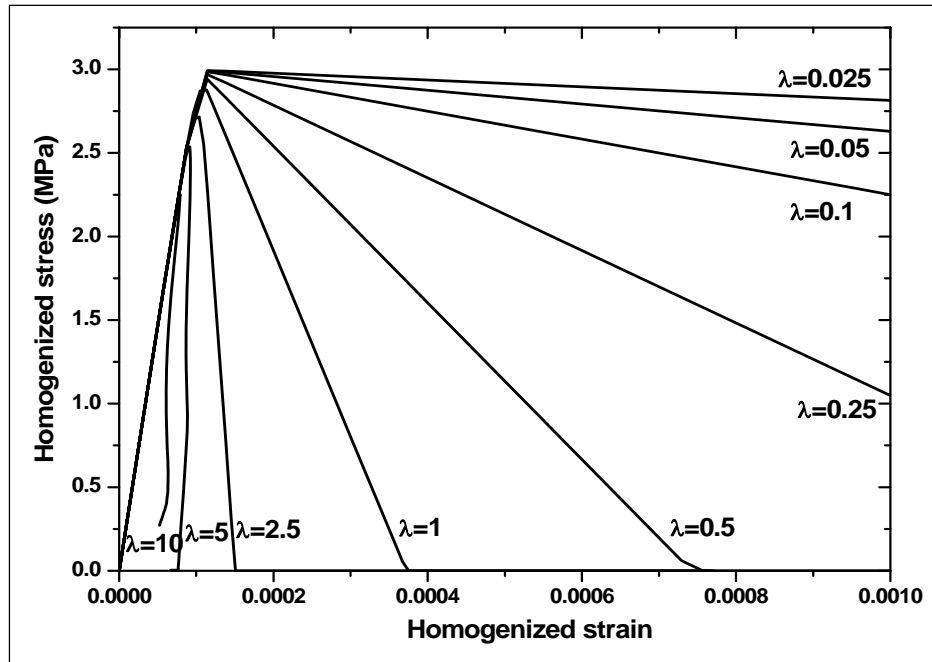


Figure 20. Homogenized stress-strain curve.

It is also noted that as the microscopic cell size increases, the energy dissipation capacity of the microscopic cell (the area under the stress-strain curve) decreases. The reason is that the energy dissipated by the cohesive crack propagation is dominated by the elastic energy within the microscopic cell as its size increases. For the microscopic cell with a dimension exceeding the dimension of the macroscopic solid, its elastic energy becomes greater than the cohesive crack opening energy, hence the snap-back behavior is observed as shown in Figure 20 for $\lambda = 5, 10$. Figure 21(a) demonstrates the size dependence of the calculated nominal strength that can be well fitted to the size effect law proposed in (Bazant 1984)

$$\sigma_N = \frac{Bf_u}{\sqrt{1+\beta}}, \quad \beta = \frac{l}{l_0} \quad (96)$$

where f_u is the tensile strength of concrete, l is the specimen dimension, and B and l_0 are material parameters identified by experimental data or numerical simulation. This size-dependent property is due to influence of the internal length scale, i.e., the crack opening displacement characteristic length, which does not scale with the overall dimension of the microscopic cell and specimen. The scale dependence of rupture strain, ε_u , is also shown in Figure 21(b), where a size effect law for ε_u can also be extracted from the numerical results.

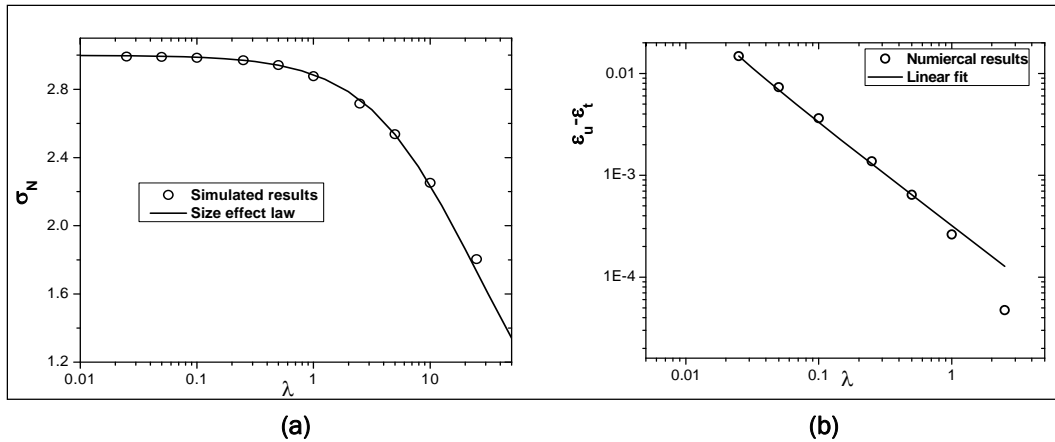


Figure 21. Size dependence of microscopic cells: (a) nominal strength; (b) difference between rupture strain ϵ_u and peak strain ϵ_t .

For microscopic cells with different dimensions and with the center crack dimension defined in proportion with the microscopic cell dimension, the homogenized damage evolution curves takes different paths from 0 to 1, as can be seen in Figure 22. Note that a critical size l_c for the microscopic cell exists ($\lambda < 0.05$ in Figure 22). This inherent critical size represents the constraint on the discretization of the macroscopic structure.

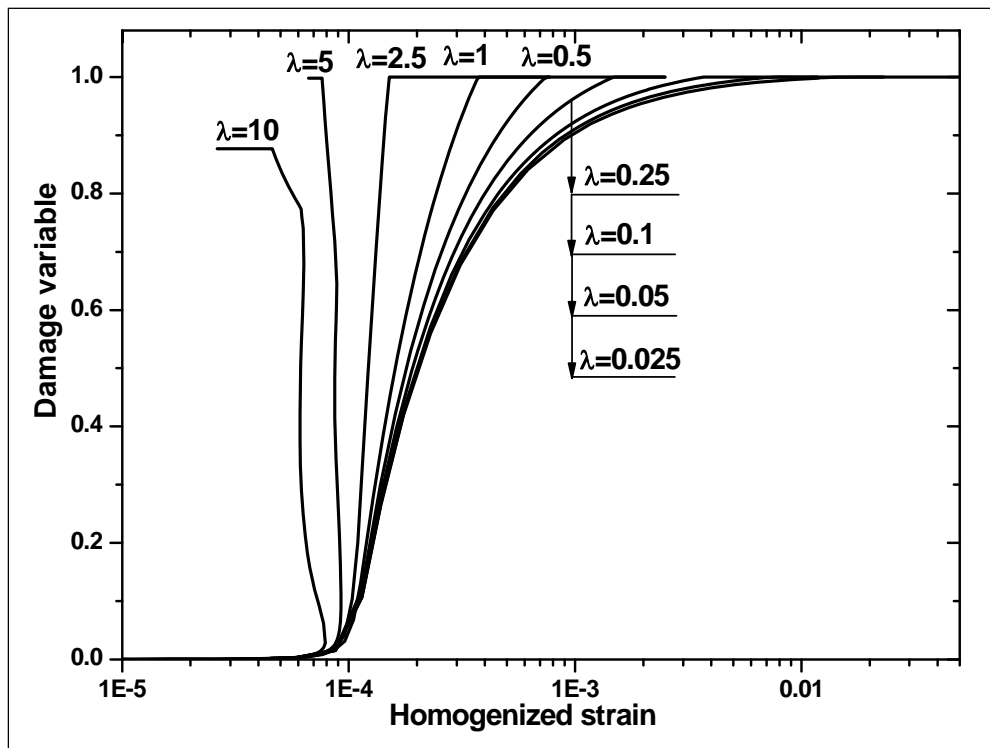


Figure 22. Microcracks informed damage evolutions.

Remark 3.4

Besides the dimension of the microscopic cell, the characterized macroscopic damage evolution is also affected by the criteria of the microcrack propagation. While cohesive energy was employed for this work as the crack propagation criterion, for general applications it should be carefully investigated according to the key characteristics of material behavior.

Mesh insensitive solution by scaled damage evolution functions

The characterized tensile damage evolution equation for the two-parameter damage model is employed in the structural level analysis based on continuum damage mechanics. Due to softening behavior of the material response, the arc-length method is used for the nonlinear analysis. To study mesh sensitivity of the multiscale analysis, coarse, medium and fine meshes are constructed for the notched beam as shown in Figure 23.

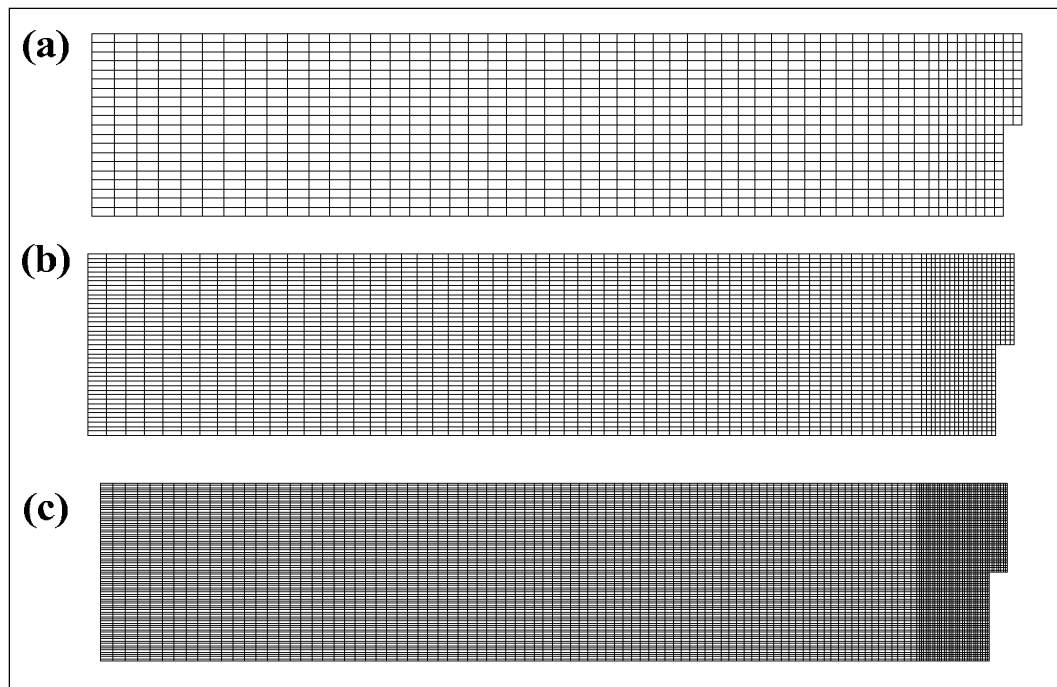


Figure 23. Finite element mesh with different levels of refinement: (a) coarse mesh; (b) medium mesh; (c) fine mesh.

In the conventional damage models, the damage evolution curves are directly used in the structural analysis without consideration of the relationship between microstructure dimensions and mesh size. Figure 24 shows a strong mesh dependency induced by this standard procedure where only

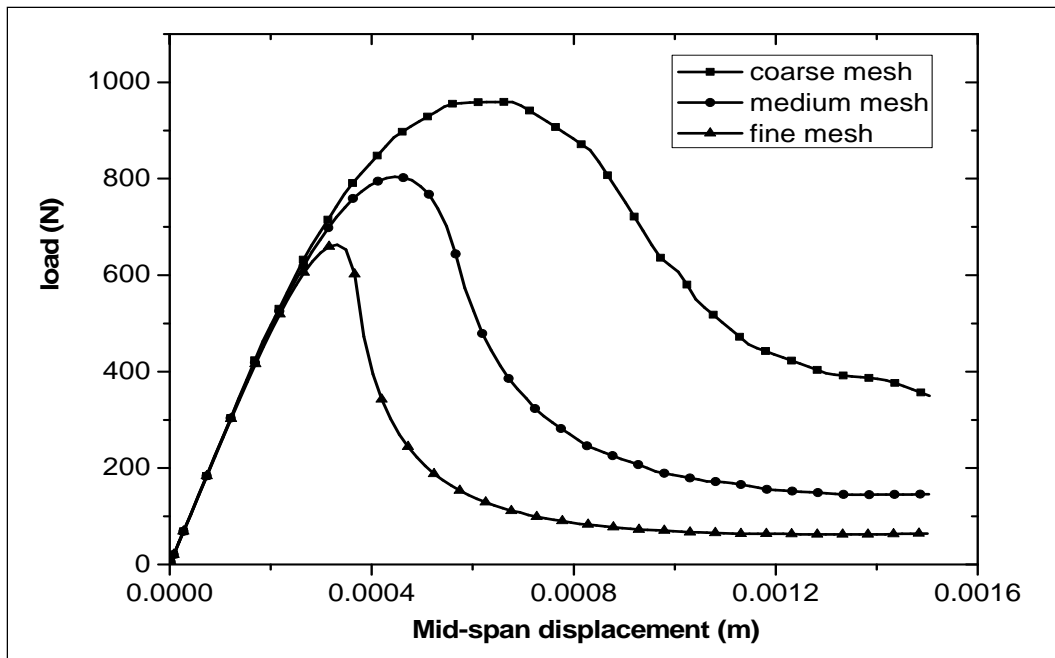


Figure 24. Mesh dependent load-displacement responses using inconsistent microscopic cell.

one microscopic cell is used to characterize the damage evolution equation without use of the scaling law in Equation 96 and linear fit of Figure 21(b). With the proposed method, the microcracks induced damage evolution curve is first characterized by the cracked microscopic cell simulation results. By introducing the scaled damage evolution curves in Figure 22 according to the mesh dimension, the mesh independent results are obtained. The agreement between numerical results with different mesh refinements and the benchmark results (Abaqus 2005) is shown in Figure 25. The stress and strain contours representing damage evolution in the structures are shown in Figure 26 and Figure 27.

Remark 3.5

The macroscopic mesh is a numerical representation of the solids included within its domain, and the stress-strain relation introduced in the quadrature points describes the homogenized behavior of the solid within the mesh. For an elastic solid, the homogenized stress-strain curve is insensitive to the mesh dimension, and thus, no mesh dependency issues exist for elastic problems. On the other hand, the softening solid typically involves length scales in the material laws, for example, the ones constructed by homogenization of microscopic fracture analysis with cohesive law introduced in this work. When the length scales in the material laws do not scale properly with the representative domain of the

macroscopic quadrature points, mesh dependent results arise. In the present work, the mesh dependency in the softening problem is removed by adopting a scaling law to a “reference homogenized stress-strain curve” obtained from a reference microscopic cell analysis.

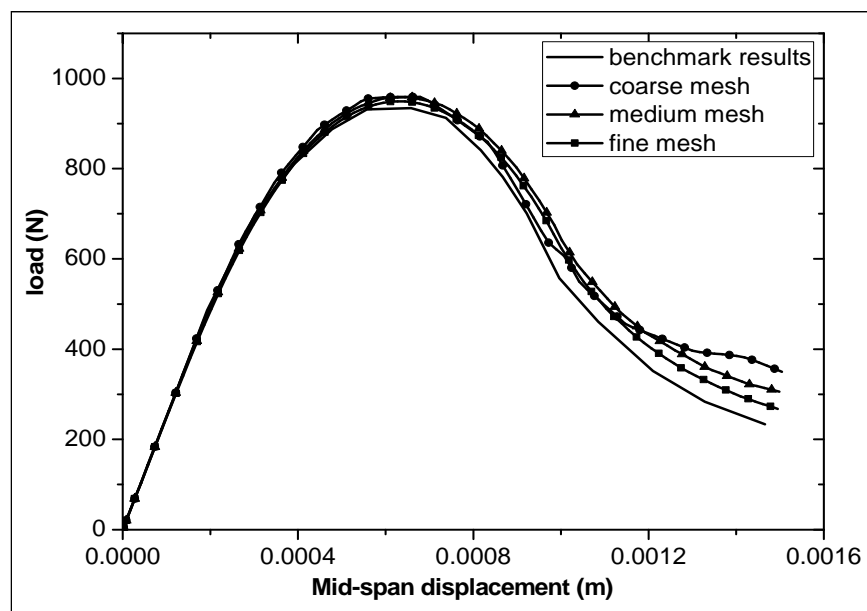


Figure 25. Mesh independent load-displacement responses using consistent microscopic cell.

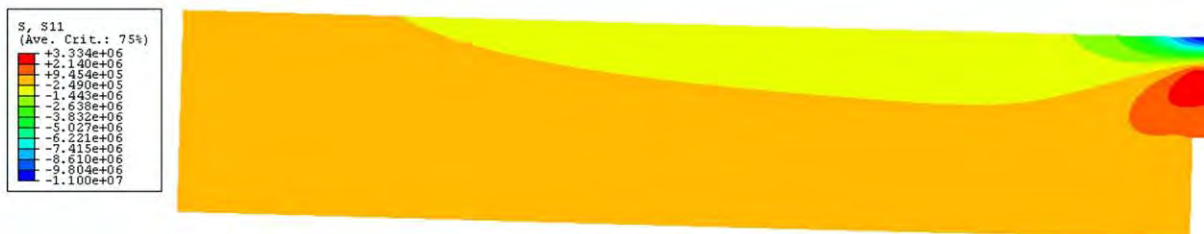


Figure 26. Contour of normal stress in horizontal direction.



Figure 27. Contour of normal strain in horizontal direction.

4 Enhanced Frictional Natural Kernel Contact Algorithm for Impact Modeling

Kernel contact algorithm

Conventional contact algorithms, such as the penalty method, require the potential contact surfaces to be pre-defined. However, for penetration problems, contact surfaces are changing continuously and they cannot always be defined a priori. In this study, a kernel contact algorithm was introduced that utilizes the interaction of kernel functions between contacting bodies to naturally serve as the impenetration condition.

Consider a semi-Lagrangian discretization of a continuum by a set of RKPM points, as shown in Figure 28, with each point carrying nodal volume A_I , mass m_I , kernel function $\varphi_a(x - x_I)$, and state and field variables. The interaction between RKPM points (Figure 28c) via the overlap of kernel supports induces a stress

$$\bar{\sigma}(\mathbf{x}) = \sum_I \mathbf{D} \bar{\mathbf{B}}_I(\mathbf{x}) \mathbf{d}_I \quad (97)$$

where \mathbf{D} is an artificial material response tensor introduced between two contacting bodies, and $\bar{\mathbf{B}}_I(\mathbf{x})$ is the smoothed gradient of the shape function.

The layer of the artificial material serves as a medium to transmit the contact forces.

An elastic-perfect plastic material model in the contact layer is introduced to represent the frictional contact condition without imposing kinematic constraints. The yield function is defined as

$$f(\boldsymbol{\tau}) = \|\boldsymbol{\tau}\| - \mu |\hat{\sigma}_{11}| \quad (98)$$

where $\boldsymbol{\tau} = [\hat{\sigma}_{12} \quad \hat{\sigma}_{13}]$, $\|\boldsymbol{\tau}\| = (\boldsymbol{\tau} \cdot \boldsymbol{\tau})^{1/2}$, and $\hat{\sigma}$ is the projected Cauchy stress tensor onto the local coordinate in which the 1-direction is in alignment with the outward normal of the contact surface, and 2- and 3- directions are in alignment with two mutually orthogonal vectors lying in the contact surface (Figure 28d).

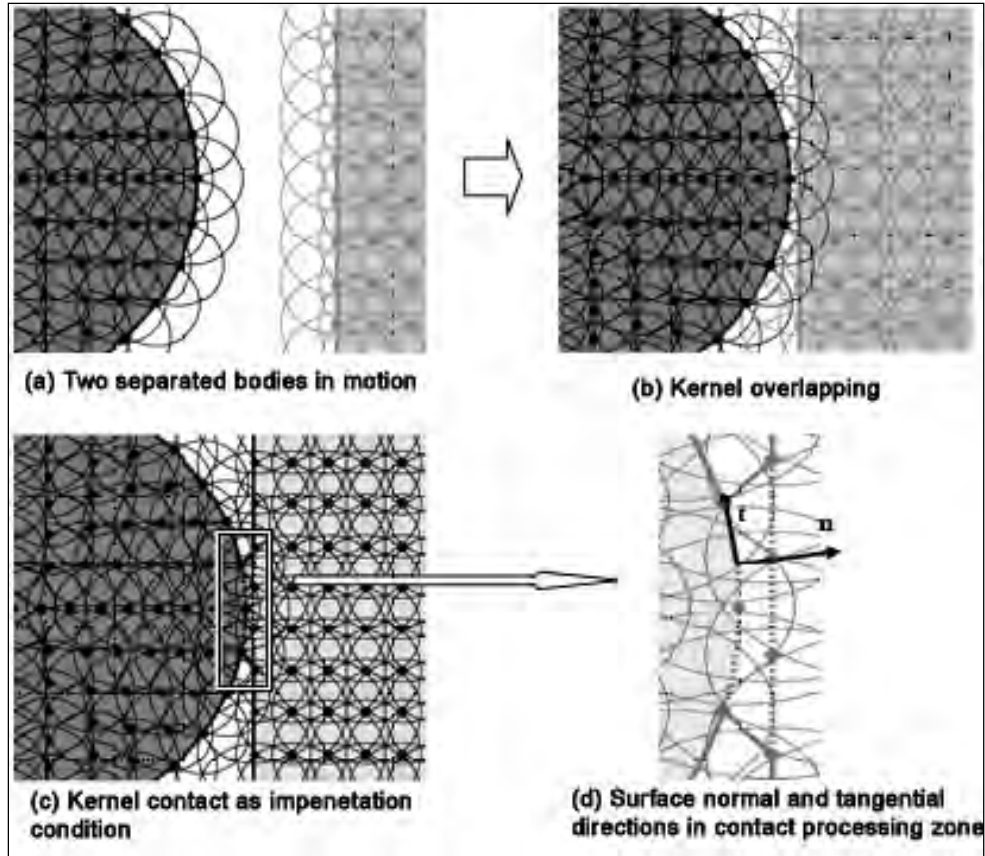


Figure 28. Kernel contact algorithm by kernel interaction between contacting bodies.

As such, the yield stress as $\mu|\hat{\sigma}_{11}|$ mimics the friction stress induced by the normal stress $\hat{\sigma}_{11}$, and the sliding condition is represented by the yield condition in the plastic model.

$$\begin{aligned} f(\tau) &< 0, \text{ stick condition (elastic)} \\ f(\tau) &= 0, \|\tau\| = \mu|\hat{\sigma}_{11}| \text{ sliding condition (plastic)} \end{aligned} \quad (99)$$

With isotropic hardening and perfect plasticity assumptions, this plasticity model represents the Coulomb's friction law.

If SCNI or SNNI is introduced for the domain integration, the internal force acting on point I is

$$\mathbf{f}_I = \sum_{J \in N_I} \bar{\mathbf{B}}_I^T(\mathbf{x}_J) \bar{\boldsymbol{\sigma}}(\mathbf{x}_J) A_J \quad (100)$$

where $N_I = \{J | \varphi_a(\mathbf{x}_I - \mathbf{x}_J) \neq 0\}$ is the set containing neighbors of point I .

In the previous equation, the total force acting on point I is obtained by summing up all pair interactions between point I and its neighbors. This property is applied to the interaction between contacting bodies as follows

$$\mathbf{f}_I = \sum_{J \in N_I} \bar{\mathbf{B}}_I^T(\mathbf{x}_J) \bar{\boldsymbol{\sigma}}(\mathbf{x}_J) A_J, \quad \forall J \in G_I \text{ and } J \notin G_I \text{ if } \mathbf{n}(\mathbf{x}_J) \cdot \bar{\boldsymbol{\sigma}}(\mathbf{x}_J) \cdot \mathbf{n}(\mathbf{x}_J) < 0 \quad (101)$$

where G_I is the group of points discretizing the body that particle I belongs to, and $\mathbf{n}(\mathbf{x}_J)$ is the unit contact surface normal. The unit normal vector will be defined by a level-set method in the next section. In this approach, when two bodies are approaching each other, the pair-wise interactions due to overlapping kernel functions serve as a natural impenetration condition as shown in Figure 28c. The radius of kernel support determines the numerical length scale in the normal contact. The stick and slip conditions can be calculated based on the tangential stress $\mathbf{n} \cdot \boldsymbol{\sigma} \cdot \mathbf{t}$ in the contact processing zone. Since the contacting bodies exhibit high velocity gradients across the contact surface, stability conditions given in Chapter 2 are crucial for the kernel contact algorithm to be stable.

Level set algorithm for determination of surface normal

The determination of contact surface using point-based discretization of contacting bodies in the RKPM requires additional effort. The accuracy of surface normal estimation at discrete points based on nodal data is crucial for contact force calculation. In this section, a level set method is introduced to estimate the contact surface normal under the RK-based kernel contact framework.

Consider the discretization of a level set function

$$\phi(\mathbf{x}) = \sum_I \Psi_I(\mathbf{x}) C_I, \quad I \in G_1 \cup G_2 \quad (102)$$

where G_K is the group of points contained in body K , and C_I is the level set nodal value associated with the RK shape function Ψ_I (Figure 29a).

The level set nodal value is defined as

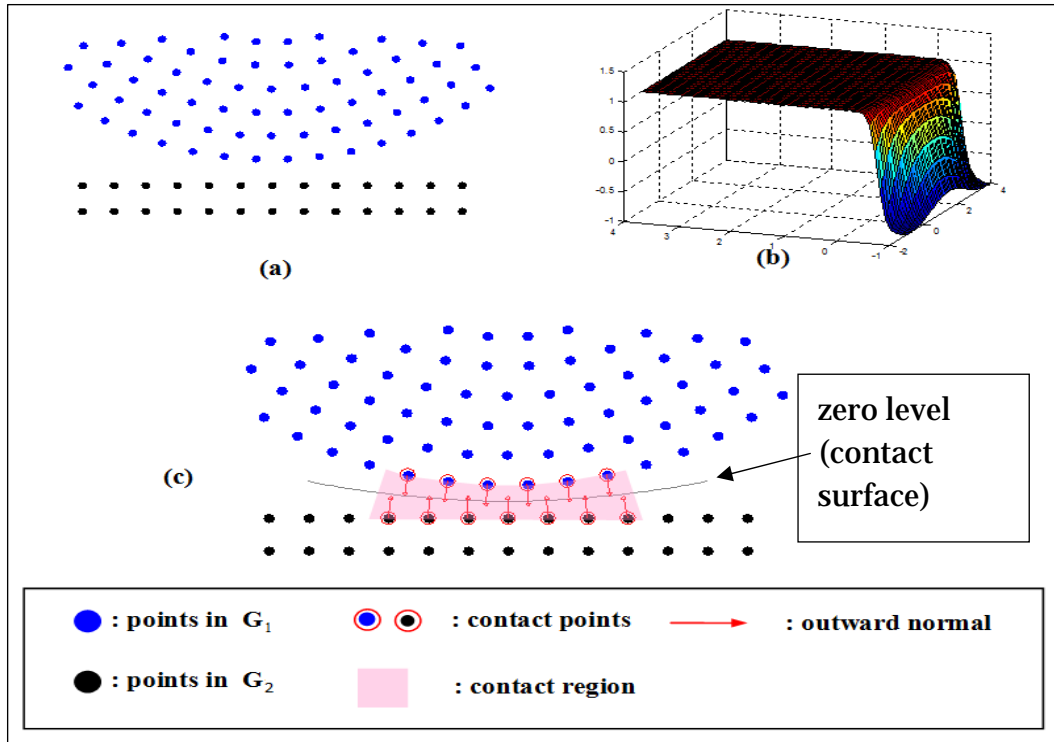


Figure 29. Level set algorithm to identify contact nodes and obtain normal vector of the contact surface.

$$C_I = \begin{cases} 1 & \text{if } I \in G_1 \\ -1 & \text{if } I \in G_2 \end{cases} \quad (103)$$

The level set function in Equation 102 gives a zero level set between these two bodies, which serves as the contact surface, as can be seen in Figure 29b and 29c. The contact surface outward normal, shown in Figure 29c, then can be estimated by

$$\mathbf{n} = -\nabla \phi(\mathbf{x}) / \|\nabla \phi(\mathbf{x})\| \quad (104)$$

Note that the gradient operator in Equation 104 can be replaced by the smoothed gradient operator described in Chapter 2. The contact force can be therefore applied to the contact points following the frictional kernel contact algorithm described in the previous section.

Numerical examples

Several numerical examples solved by the frictional natural kernel contact algorithm are presented in this section to demonstrate the accuracy of the proposed method.

Elastic collision of two bodies

Consider a two-body elastic contact problem as illustrated in Figure 30. The two bodies have the same discretizations and same material properties (Young's modulus and mass density). Body 1 is prescribed with initial velocity of 500 m/sec and Body 2 is initially at rest. First of all, the natural kernel contact algorithm is examined by the case with same support sizes of the two bodies. Numerical results of the two-body elastic collision are presented in Figure 31. As observed from the results, the contact of two bodies is handled properly with the proposed natural kernel contact algorithm, whereas both linear momentum and total energy are conserved during the contact process.

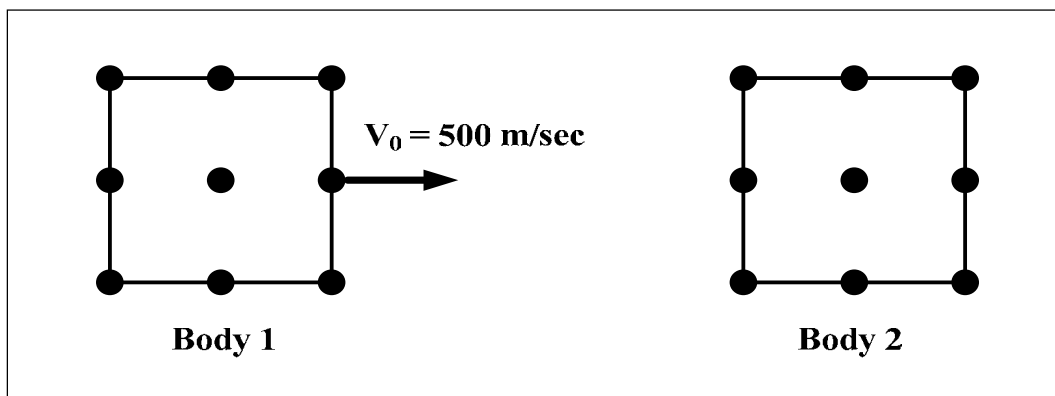


Figure 30. Geometric schematic of two-body elastic contact.

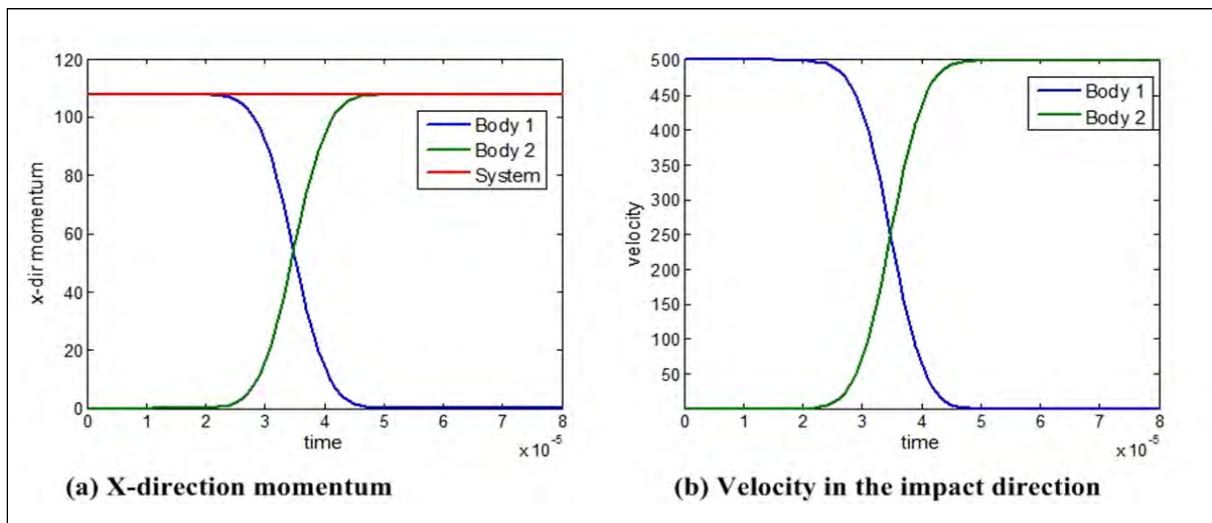


Figure 31. Numerical results of two-body elastic contact with same properties and support sizes.

To demonstrate the effect of tensile contact force correction which is the condition as indicated in Equation 101, another two-body contact problem with masses $m_1 = m$ and $m_2 = 4m$, and normalized support sizes $a_1 = 2.0$ and $a_2 = 1.75$ is investigated. Figure 32 shows the numerical results with and without correction of tensile contact force. It is clear that the pulling back effect due to non-physical tensile contact force between two bodies can be eliminated by introducing the tensile force correction, and the post-contact velocities of two bodies are close to the theoretical values.

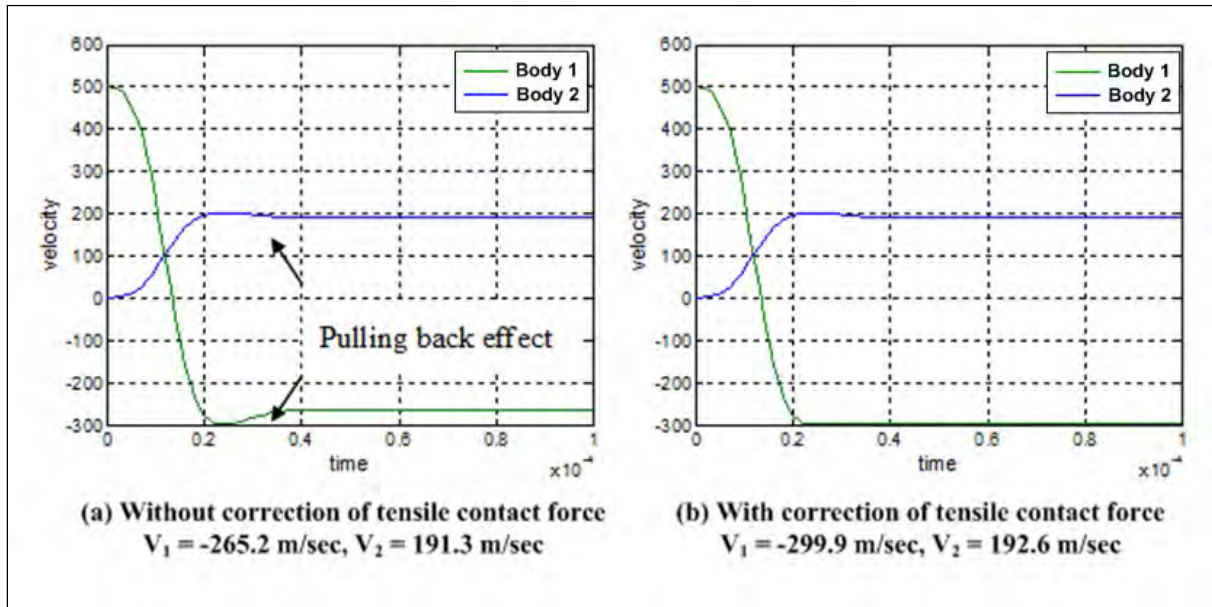


Figure 32. Numerical results of two-body elastic contact with $m_1 = m$, $m_2 = 4m$ and $a_1 = 2.0$, $a_2 = 1.75$.

Sliding block on a rigid surface

An elastic block resting on a rigid surface is illustrated in Figure 33. Both the rigid surface and flexible body are discretized by RKPM particles. After the block rests on the rigid wall and reaches equilibrium, the rigid surface rotates an angle of 60 deg and the block begins to slide. Frictional coefficients $\mu = 0.0$ and $\mu = 0.2$ are considered. Figure 34 shows the numerical results obtained by RKPM simulation for the case $\mu = 0.2$, and the numerical predictions of the displacement of the elastic body compared with analytical solutions are illustrated in Figure 35 for both $\mu = 0.0$ and $\mu = 0.2$. It is observed that the numerical solutions have good agreement with the analytical solutions.

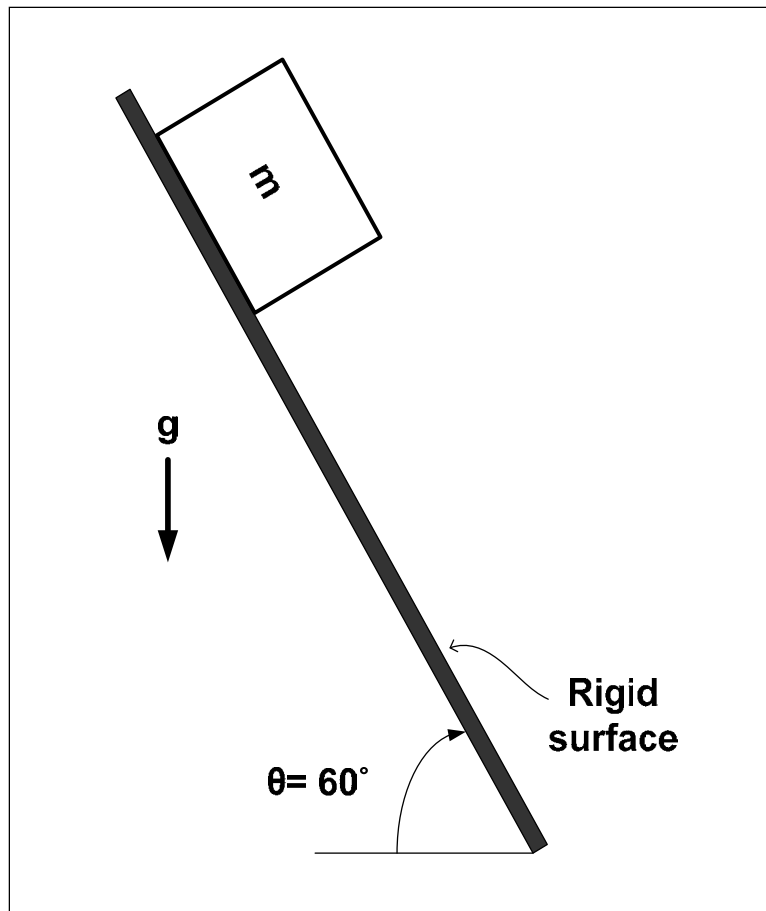


Figure 33. Schematic of an elastic block resting on a rigid surface subject to gravity.

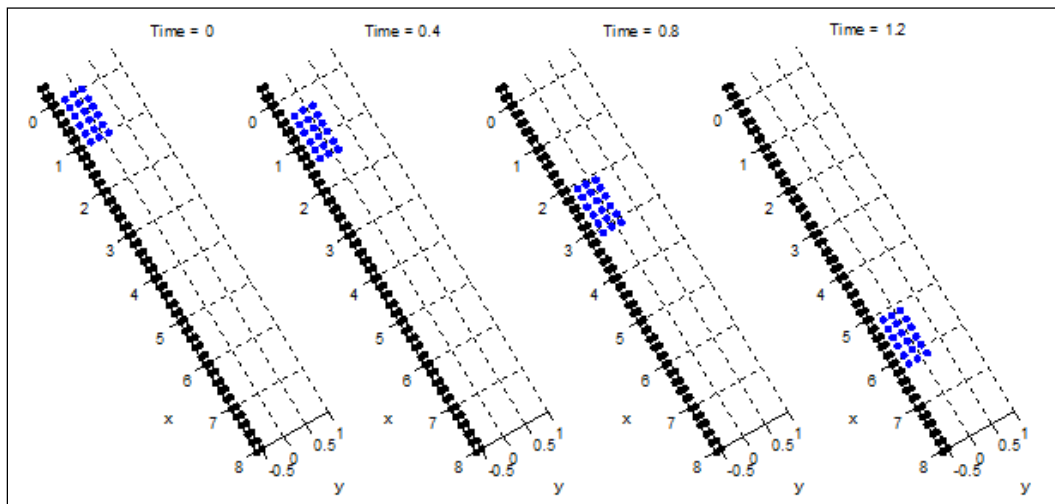


Figure 34. Sliding block problem with the enhanced natural kernel contact algorithm and level set identification of contact surface normal ($\mu = 0.2$).

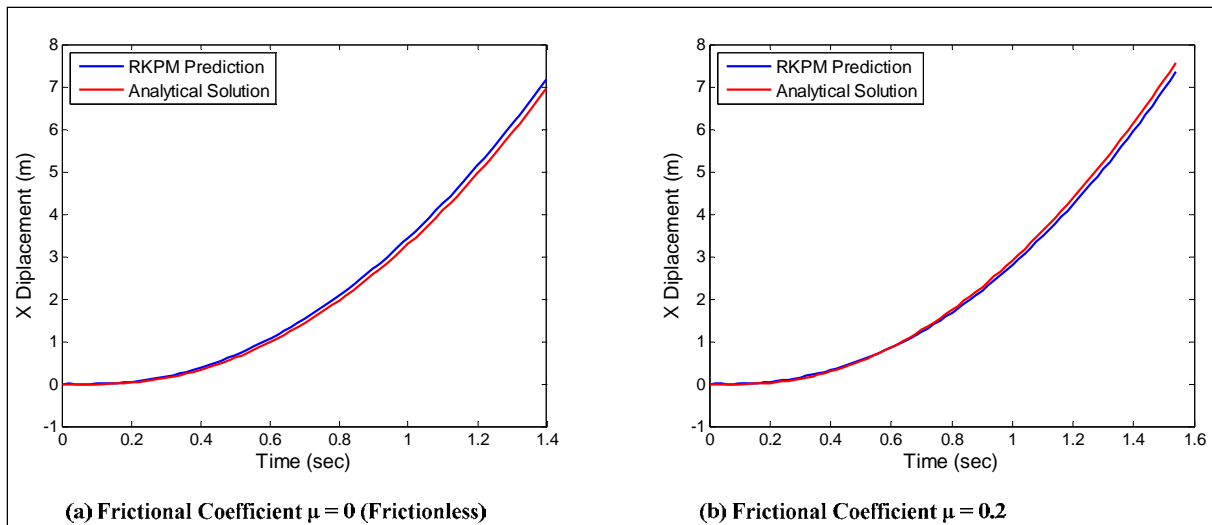


Figure 35. Comparison of block displacement in the sliding block problem with the natural kernel contact algorithm and level set identification of contact surface normal.

Dynamic Hertz contact

The dynamic Hertz contact problem is analyzed with an elastic ball impacting toward a rigid surface as illustrated in Figure 36. Figure 36 also shows the RKPM discretization of the elastic ball and rigid wall. The numerical solution of contact radius is compared with analytical solution (Timoshenko and Goodier 1934) as shown in Figure 37. As seen from the results, the proposed kernel contact algorithm with contact surface identification via level set method is effective for the dynamic contacts.

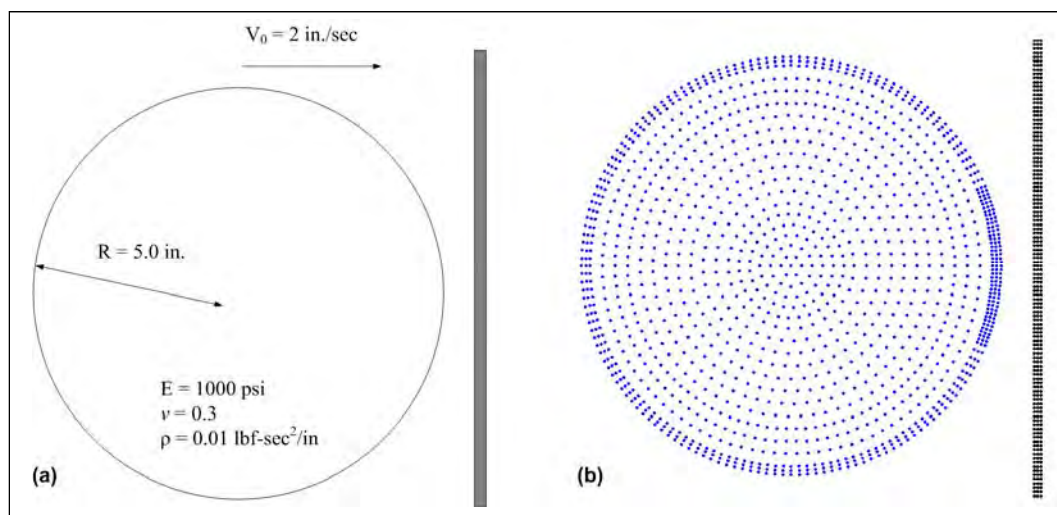


Figure 36. Hertz contact problem: (a) problem statement and (b) RKPM discretization.

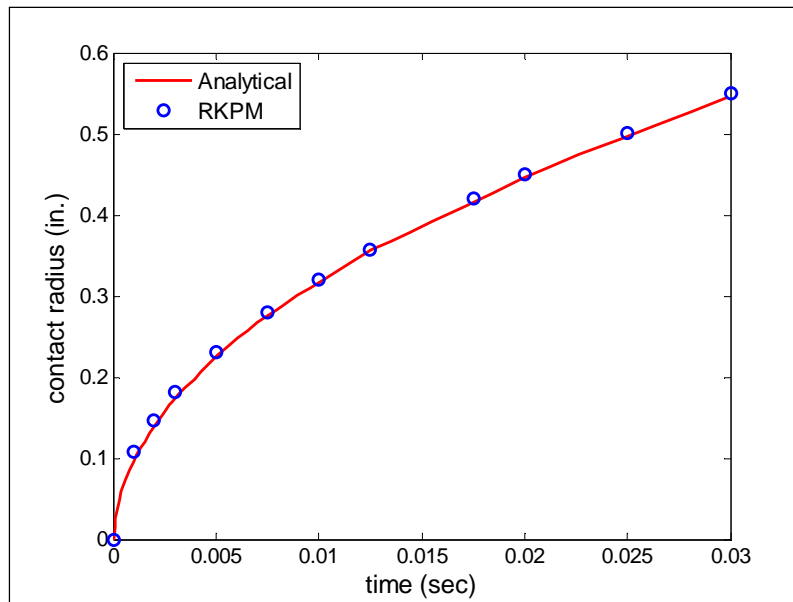


Figure 37. Numerical result of contact radius compared to analytical solution (Timoshenko and Goodier 1934).

Dynamic contact of elastic ring

Analyzed here is an elastic ring with Young's modulus $E = 10$ GPa and Poisson's ratio $\nu = 0.4$ impacting on a rigid surface with the initial velocity $v_0 = 50$ m/sec as depicted in Figure 38. Both gravitational forces and frictions are ignored in the simulation. The progressive impact processes for the contact surface normal determined by level set algorithm are presented in Figure 39. Figure 40 shows the comparison of the impact and reflected angles between the two algorithms of surface normal calculation, one by nodal orientation between two particles and the other one by level set algorithm as introduced in the previous section. It is clear that the simple computation of contact surface normal by level set algorithm provides fairly accurate surface normal for impact modeling.

Next, the dynamic contact of two elastic rings is analyzed as shown in Figure 41. The rings are made of the same material properties as the previous one-ring problem. The two rings are moving toward each other with an initial velocity $v_0 = 50$ m/sec. The progressive contact processes and total energy of the system are illustrated in Figures 42 and 43, respectively. It is seen that the contact of these two elastic rings is properly handled with the proposed kernel contact algorithm.

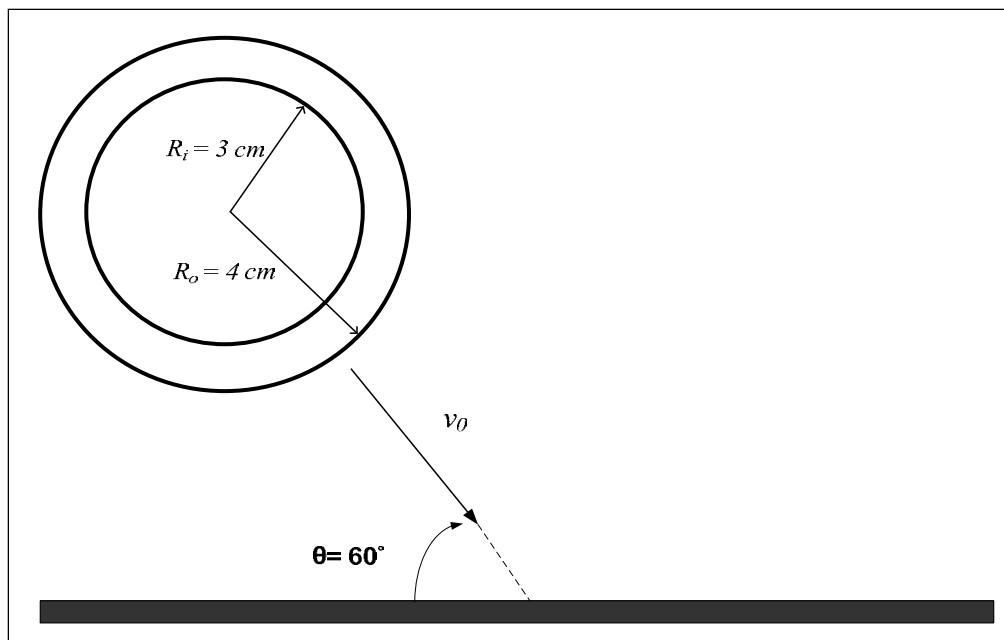


Figure 38. Geometry of an elastic ring impacting on a rigid surface.

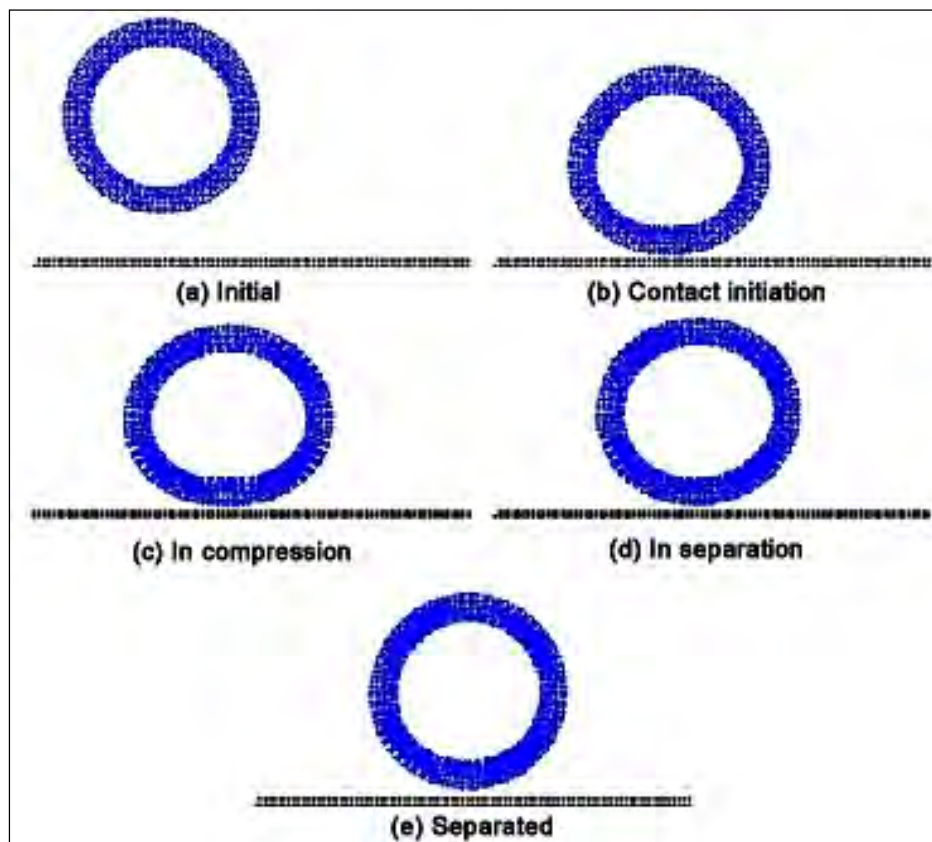


Figure 39. Impact of an elastic ring on a rigid surface by natural kernel contact algorithm.

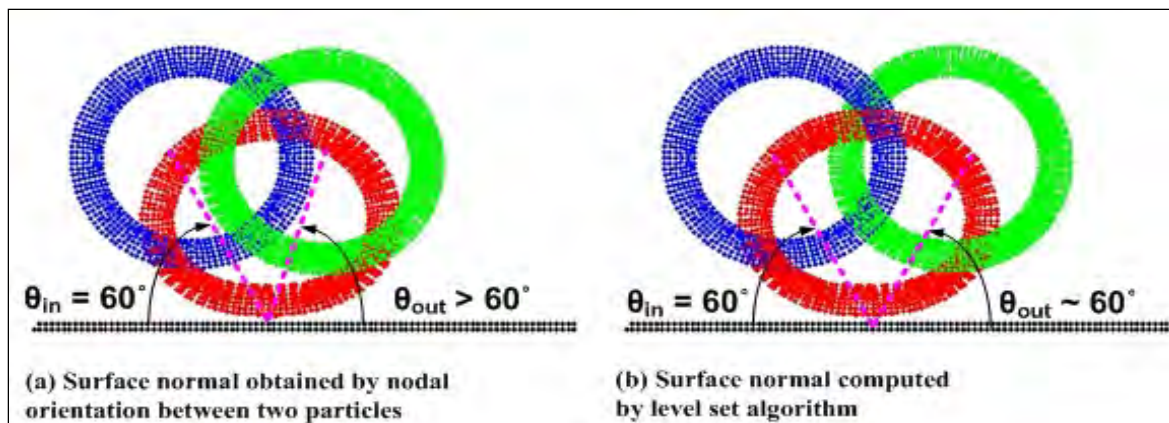


Figure 40. Comparison of impact and reflected angles between two algorithms for determination of contact surface normal.

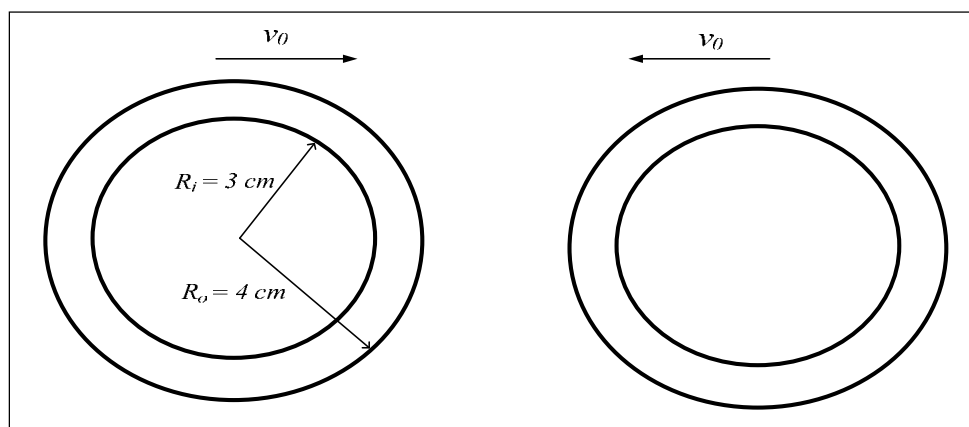


Figure 41. Geometry of two elastic rings.

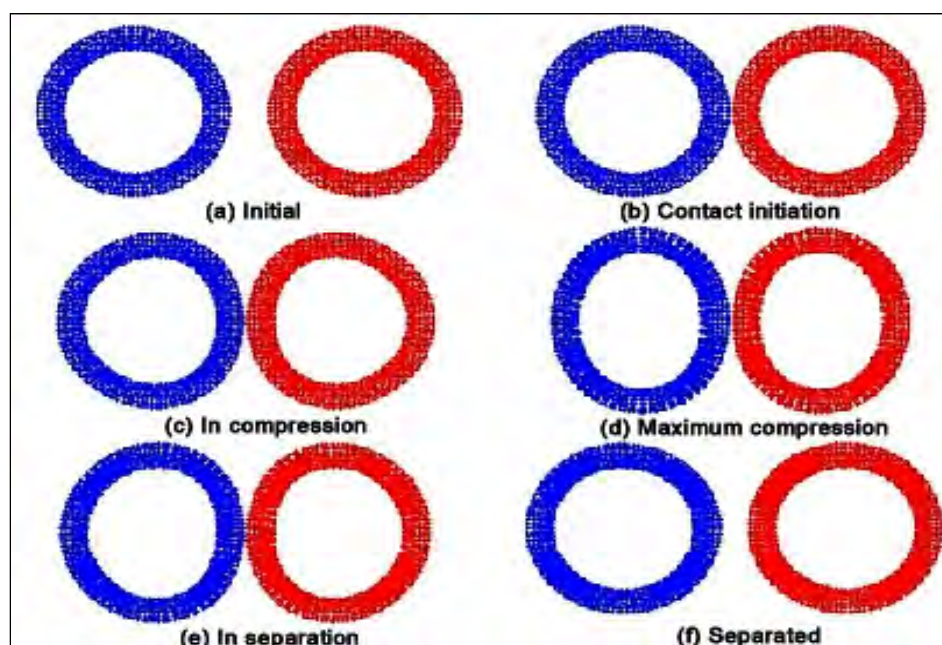


Figure 42. Impact of two elastic rings using natural kernel contact algorithm.

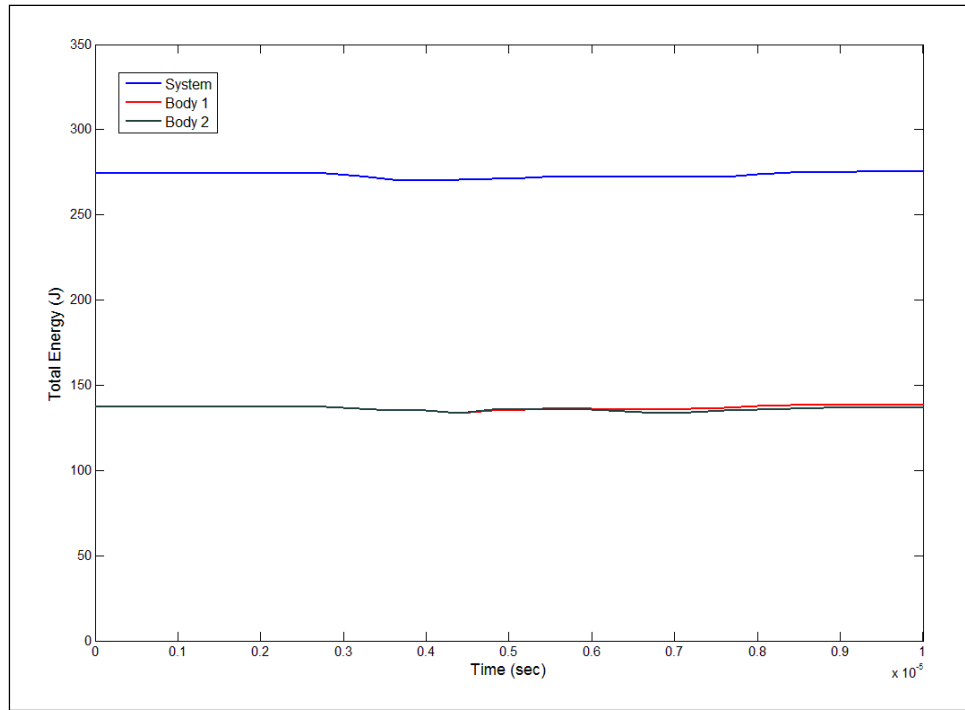


Figure 43. Time-history of total energy for the two-ring impact problem.

Cylindrical aluminum bar impacting a rigid wall

This classical impact problem with available experimental and numerical results (Taylor 1948; Wilkins and Guinan 1973) is used to test the performance of the proposed contact algorithm for plastic deformation. The initial radius and initial height of the aluminum cylindrical bar are 0.391 and 2.346 cm, respectively. The material properties of the cylinder are: density $\rho = 2700 \text{ kg/m}^3$, Young's modulus $E = 78.2 \text{ GPa}$, Poisson's ratio $\nu = 0.3$, and J2 plasticity with yield strength $\sigma_y = 0.29 \text{ GPa}$. The initial impact velocity is 373 m/sec and the rigid surface is assumed to be frictionless. Perfect plasticity and strain-hardening elasto-plasticity with the following hardening rules are considered for this problem

$$H(\bar{e}^p) = 0 \quad (105)$$

$$K(\bar{e}^p) = \sigma_T (1 + 125 \bar{e}^p)^{0.01} \quad (106)$$

where \bar{e}^p is the effective plastic strain, and H and K are the plastic modulus and yield stress, respectively (Chen et al. 1996).

Both the aluminum bar and rigid plate are discretized by the RKPM particles in three-dimensions (29,788 RKPM particles) as illustrated in Figure 44. The contact between the aluminum bar and the rigid wall is handled by the frictional natural kernel contact algorithm, and the problem is modeled by the semi-Lagrangian formulation with SNNI nodal integration.

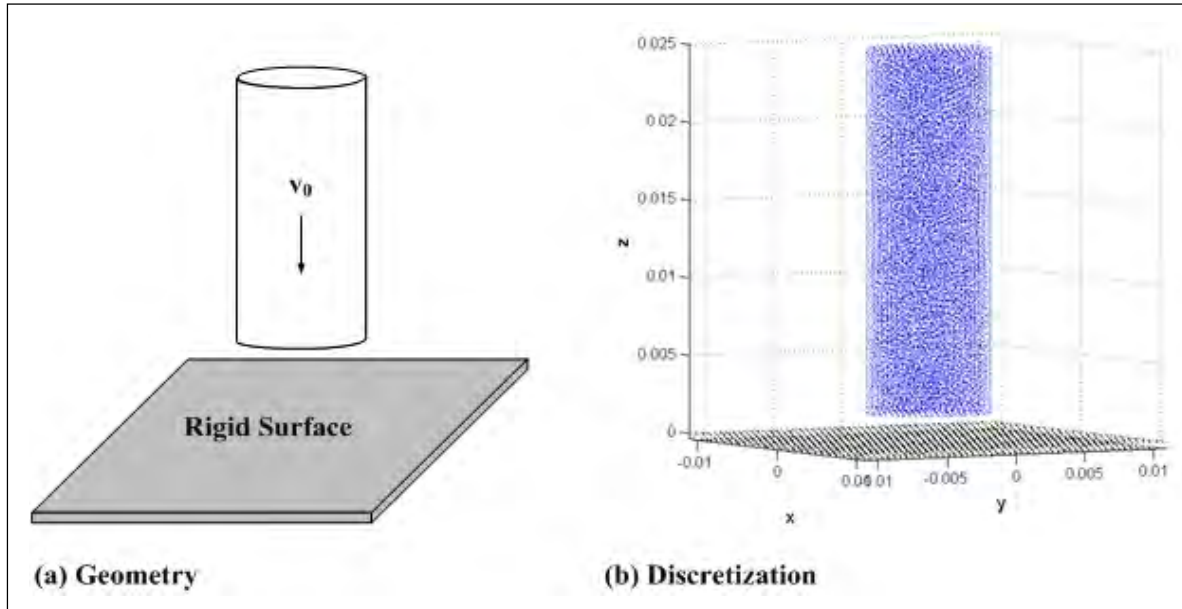


Figure 44. Schematic of Taylor bar problem and corresponding RKPM discretization.

Table 1 summarizes the comparison of deformed heights and radii between RKPM predictions and experimental measurement. The deformed configurations of the aluminum bar at different time frames for both hardening and perfect plasticity materials obtained by RKPM SNNI semi-Lagrangian calculation are shown in Figure 45. This study also compares Lagrangian RKPM results reported by Chen et al. (1996). Note that for problems with moderate level of deformation, such as in this impact problem, the semi-Lagrangian method is at best as good as the Lagrangian method. The results in Table 1 show that the semi-Lagrangian RKPM results are very close to the Lagrangian RKPM results, indicating the robustness of the proposed semi-Lagrangian approach.

Table 1. Comparison of deformed geometries for Taylor bar impact problem.

	Perfect Plasticity		Hardening		
	RKPM Lagrangian (Chen 1996)*	RKPM Semi- Lagrangian SNNI	RKPM Lagrangian (Chen 1996) ^a	RKPM Semi- Lagrangian SNNI	Experiment (Wilkins and Guinan 1973)
Height (cm)	1.454	1.442	1.645	1.642	1.651
Radius (cm)	1.051	1.025	0.837	0.819	NA

^a Axisymmetric model with 11×31 particles was analyzed in (Chen 1996).

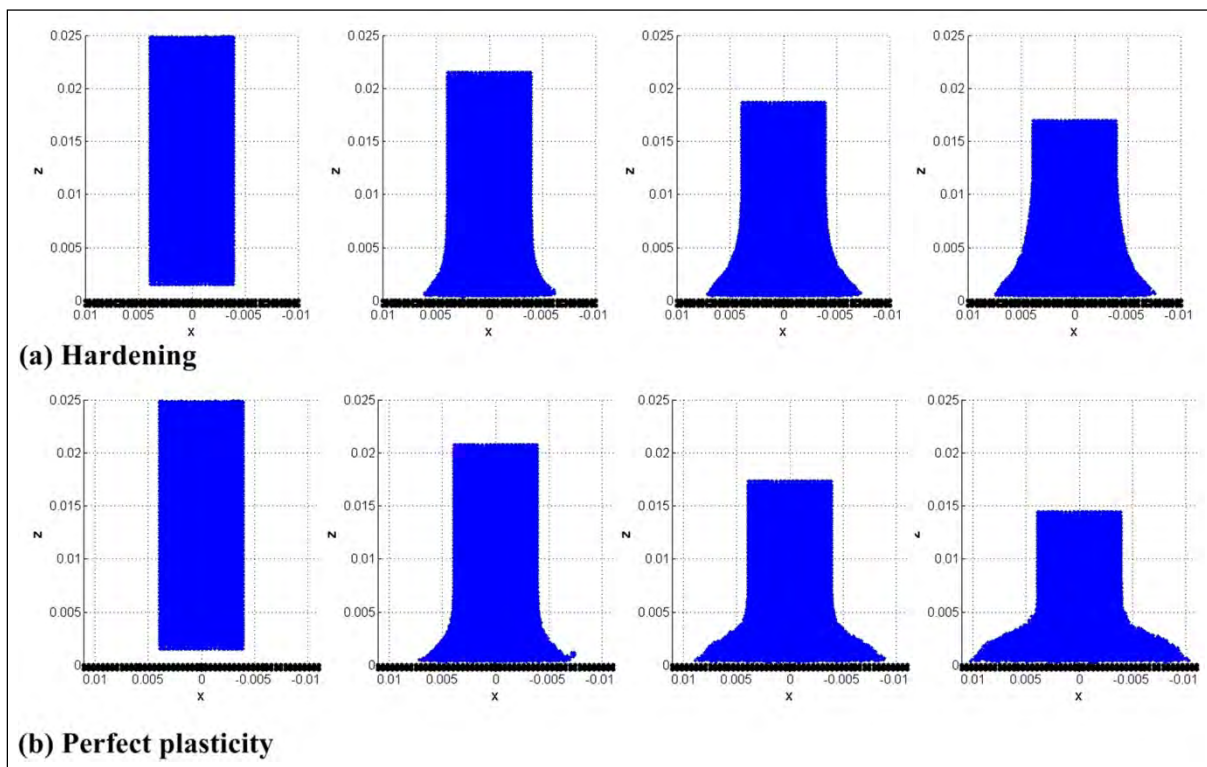


Figure 45. Cylindrical impact deformations predicted by the semi-Lagrangian SNNI RKPM.

5 V&V Penetration Study

An extensive verification and validation (V&V) study was conducted to validate performance of the Nonlinear Meshfree Analysis Program (NMAP) parallel code (Chi et al., in preparation) for penetration modeling. The V&V problem set consisted of 18 simulations that followed penetration experiments (Boone, in preparation) conducted in ERDC's Fragment and Small Arms laboratory. Results from two experiments were provided by ERDC at the beginning of the V&V study, and results from five additional tests were provided approximately half-way through the V&V effort. The remaining 11 experiments were modeled blindly. Calculations were jointly performed on the UCLA Hoffman2 cluster and systems at the ERDC DoD Super Computing Resource Center.

Experimental setup

The penetration experiments were conducted by firing a spherical projectile into a thin-panel concrete target with an impact angle of zero-degree obliquity. Impact velocity, projectile size, and panel thickness were varied to obtain terminal ballistic conditions ranging from strong overmatch (i.e., projectile exited the panel with significant residual velocity) to stopping the projectile. Three steel projectile sizes were used, with diameters of 7.9 mm (32 grain mass), 11.1 mm (86 grain mass), and 12.7 mm (129 grain mass). All projectiles were made from American Society for Testing and Materials (ASTM) A681 (2008), Grade 200 hardened S2 tool steel with material properties provided by ERDC and given in Table 2.

Table 2. Spherical steel projectile properties.

Property	Value ^a
Tensile strength, ultimate	2,150 MPa
Tensile strength, yield	2,000 MPa
Elongation at break	7% in 50 mm
Bulk modulus	140 GPa
Shear modulus	80 GPa

^a Material property data provided by ERDC.

The target panels were nominally 305 mm × 305 mm in planimetric dimension, with thicknesses of approximately 12.7 mm, 25.4 mm or

38.1 mm. All panels were produced using CorTuf ultra high-strength concrete (Williams et al. 2009). The CorTuf material was reinforced with approximately 30-mm long, hooked-end Bekaert Dramix® ZP305 steel fibers. Due to the length of the steel fibers with respect to the panel thicknesses, a certain amount of preferential fiber orientation (in the plane of the panels) occurred. However, the degree of preferential orientation was not quantified.

In each experiment the projectile was fired from an un-rifled barrel; therefore no rotational velocity was induced. The target panels were mounted in a support fixture and were held in place by clamping all four edges between a pair of metal plates. Rubber strips were placed between the plates and panel to avoid stress concentrations resulting from the uneven concrete surfaces. The grip of the plates onto the panels was approximately 25 mm on all sides. With the exception of Trial 2 and Run 15, projectiles were fired at the center of the CorTuf targets. In Trial 2 and Run 15, the projectiles were fired to impact the panels in the top right and bottom right quadrants, respectively. In both cases the projectile impacted approximately 75 mm from the panel edges. Quantification of the experimental results included measurement of the impact and exit velocities, impact and exit crater sizes, tunnel size, and post-test projectile mass.

A CorTuf target panel mounted into the test support fixture is shown in Figure 46.

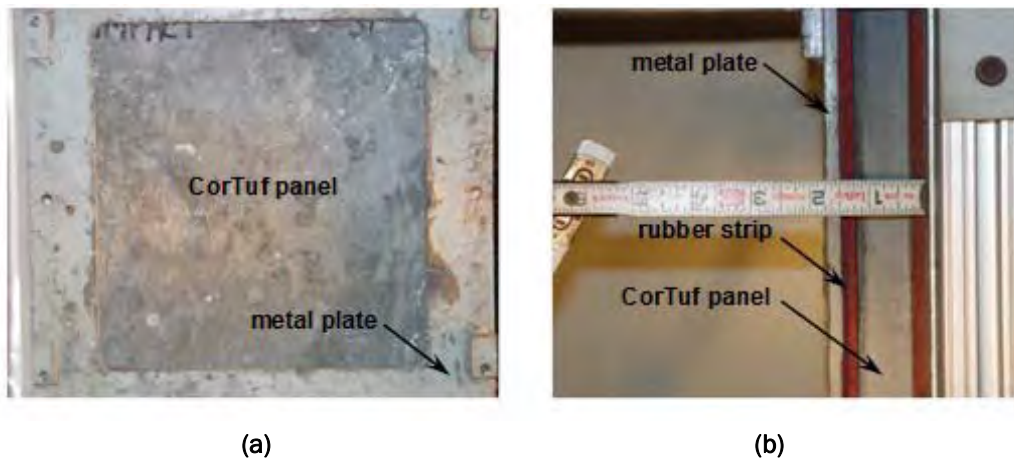


Figure 46. CorTuf panel mounted in test support fixture, (a) front view (impact face) and (b) side view.

NMAP model

To construct the NMAP models, the 12.7-mm-, 25.4-mm-, and 38.1-mm-thick panels were discretized using 107,811; 190,000; and 357,309 nodes, respectively. Nodal spacing in the plan dimensions was increased from the center toward the outer edges, with a maximum change in nodal spacing of 4% between each node. Nodal spacing was held constant through the panel thickness as summarized in Table 8. The projectiles were discretized using 561; 1,163; and 1,517 nodes for the 32-grain, 86-grain, and 129-grain projectiles, respectively. The optimum discretization for each panel and projectile size was studied, which is discussed in the following section. Boundary conditions were applied to the panels by fixing nodal displacements along all panel edges.

The projectiles were modeled using a J2 plasticity model with isotropic hardening. Material yield stress was modified to account for the so-called dynamic increase factor (DIF) associated with strain-rate effects. A DIF of either 1.2 or 1.5 was used depending on projectile impact velocity, which is discussed in the following section. Material model parameters used for the projectile are given in Table 3. The CorTuf panels were modeled using the MIDM (microcrack informed damage model)-enhanced AFC model (Ren et al. 2011), with selected experiments also modeled with the original AFC model (Adley et al. 2010). AFC model parameters for the CorTuf material were provided by ERDC and are given in Table 4.

Table 3. J2 material model parameters for projectile.

Parameter	Value
Young's modulus, E	200 GPa
Poisson's ratio, ν	0.26
Yield stress, σ_y^a	2400 MPa/3000 MPa
Hardening modulus, H	2500 MPa
Density	7806 kg/m ³

^a DIF=1.2/DIF=1.5.

Determination of optimal parameters for V&V modeling

The following parametric study was conducted to determine optimum parameters for modeling the V & V penetration problems. This study was carried out in order to provide guidelines for the user to efficiently perform numerical analysis of impact problems. Numerical studies are provided to illustrate the choice of optimal parameters.

Table 4. AFC model parameters for CorTuf panel.

Parameter	Value
G (shear modulus)	18.457 GPa
C1	1016.3 MPa
C2	908.65 MPa
C3	0.0125
C4	0.10382
C5	792.89 MPa
Q1	artificial bulk viscosity not used
Q2	artificial bulk viscosity not used
PMIN	6.8947 MPa
C6	172.37 MPa
C7	0.00781
C	7919.2 MPa
D	-29.205 GPa
S	187.10 GPa
C9	77.958 GPa
C10	0.24863
D1	$4.0597 \times 10^{-10} \text{ Pa}^{-1}$
AN	$1.7345 \times 10^{-9} \text{ Pa}^{-1}$
TXETXCR	0.625
PRECRIT	0.177×10^{22}
HMIN	1
RHO (density) ^a	2267.4 kg/m ³
DAMP	0.0001
FC (tensile strength for MIDM)	6.8947 MPa

^a 2267.4 kg/m³ was value used in model; density reported by ERDC was 2557 kg/m³.

- **Discretization of the two bodies:**

Discretization and support size discrepancies between the contacting bodies were studied to determine the effect on the numerical solution. Two studies are conducted on two elastic bodies impacting each other. Body 1 of mass m_1 has initial velocity v_1 . Body 2 of mass m_2 is initially at rest. Assuming an initial velocity, v_1 , of 500 m/s, analytical results for the velocity of the bodies after contact can be obtained by

$$V_1 = \frac{(m_1 - m_2) v_1 + 2m_2 v_2}{m_1 + m_2} = -300 \quad (107)$$

$$V_2 = \frac{(m_1 - m_2)v_2 + 2m_2v_1}{m_1 + m_2} = 200 \quad (108)$$

The first study investigates the impact of two elastic bodies with the same discretization, as described in Figure 47. Velocity history of the two bodies is shown in Figure 48. This study reveals that if the two bodies are discretized by the same nodal density and support size, the numerical results from the contact algorithm are consistent with the analytical solution. Nevertheless, for a small penetrator, using the same nodal density for projectile and panel leads to a very fine discretization of the panel and is not efficient. Therefore, a compromise is made by selecting a coarser nodal density for the panel.

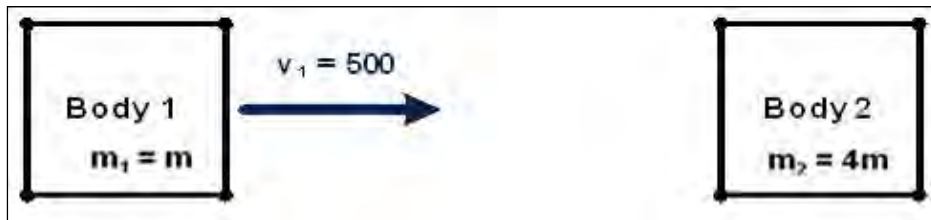


Figure 47. Study 1 problem statement.

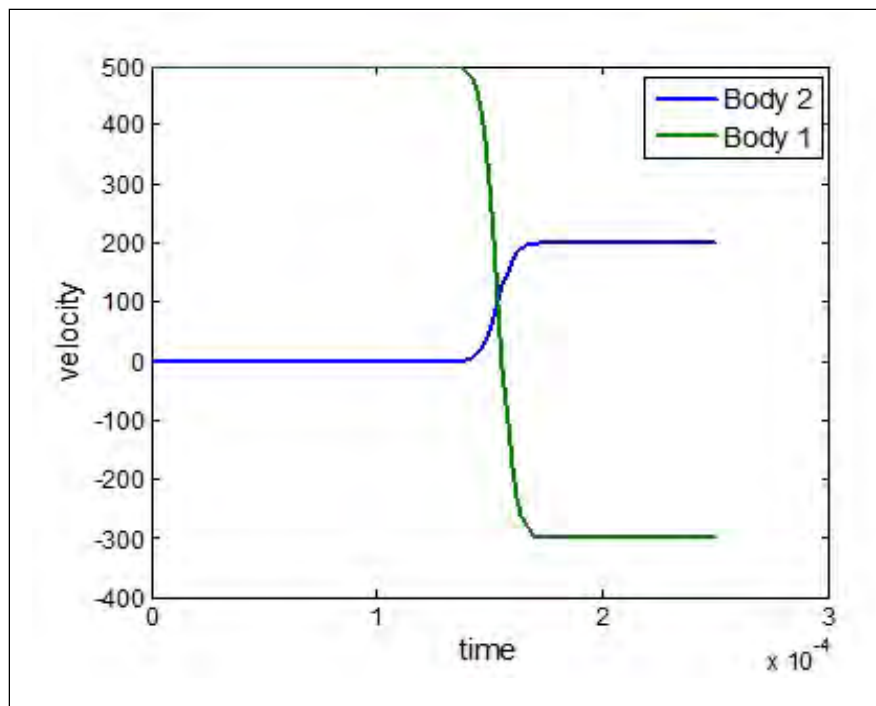


Figure 48. Velocity histories of Study 1.

In the second study, the case of two elastic bodies with different discretizations is modeled as illustrated in Figure 49. The effect of support size on the numerical results is summarized in Table 5. The results from this second study reveal that similar support size for both bodies should be used even when using different discretizations. Conservation of linear momentum for each support size ratio is observed (see Figure 50), but conservation of energy is not satisfied for large support size discrepancies as shown in Figure 51.

Table 5. Effect of support size on numerical result in terms of velocity.

Support Size ^a	V ₁	V ₂
2.0 : 1.0	-152	163
2.0 : 1.5	-294	199
2.0 : 1.8	-299	200

^a Support size Body 1: support size Body 2.



Figure 49. Study 2 problem statement.

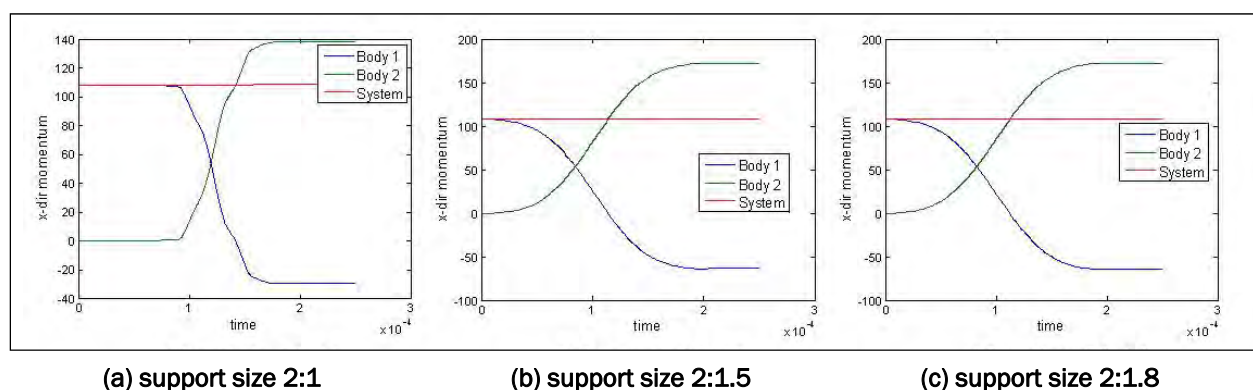


Figure 50. Linear momentum history.

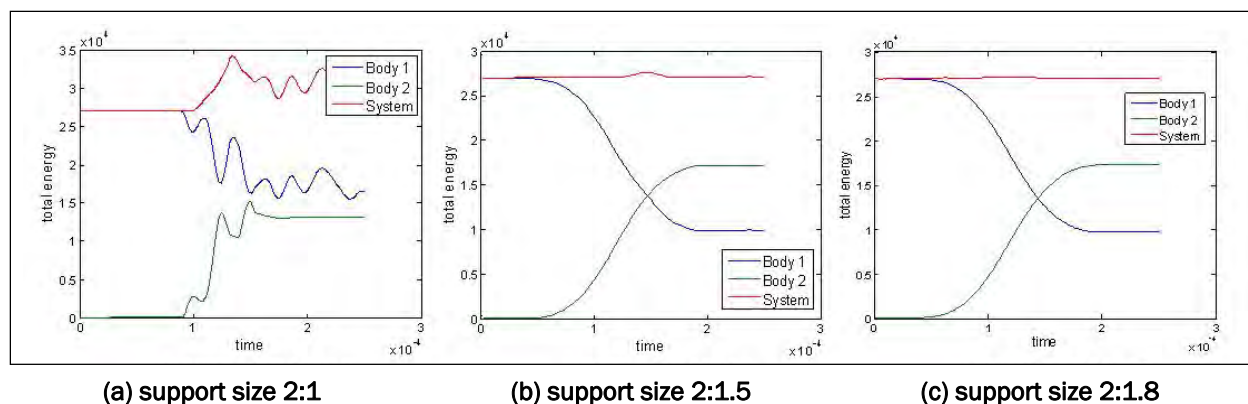


Figure 51. Energy history.

Next, a study was conducted with four V&V problems to select the optimal nodal distance ratio between the projectile and panel. A minimum nodal distance for the panel particles is defined using the time-step obtained from the Courant-Friedrichs-Lewy (CFL) condition and the elastic and plastic wavelength. The one obtained considering the elastic wavelength is the most conservative. In this discretization, a nodal distance of approximately 1 mm was used for projectile, which gives a ratio of about 0.0268 between nodal distance and the elastic wavelength for the system. The numerical study in Table 6 shows that the suitable projectile and panel discretization near the contacting surfaces corresponds to a nodal spacing in the panel of approximately 1.4 to 1.5 times the nodal spacing in the projectile. The selected discretization of the different projectile sizes according to this ratio is shown in Table 7.

Table 6. Effect of discretization on exit velocity.

Nodal Distance Ratio	1:1.8 ^a		1:1.4 ^a		1:1.2 ^a		Experiment Results
	Number of Particles	Exit Velocity (m/sec)	Number of Particles	Exit Velocity (m/sec)	Number of Particles	Exit Velocity (m/sec)	Exit Velocity (m/sec)
Trial 1 Impact velocity = 1708 m/sec	183,346	511.50	358,472	571.10	620,278	448.00	684.58
Trial 2 Impact velocity = 577 m/sec	101,019	12.76	201,163	-2.19	346,763	5.83	0
Run 4 Impact velocity = 1718 m/sec	130,892	570.50	268,781	646.00	519,917	560.13	791.56
Run 5 Impact velocity = 239.27 m/sec	59,610	12.11	124,157	3.72	190,894	9.78	0

^a Projectile nodal spacing:panel nodal spacing in contact area.

Table 7. Discretization of projectile.

Projectile Size	Nodal Distance (m)	Discretization
32-grain – 7.9 mm	0.0008897	561 particles
86-grain – 11.1 mm	0.0009698	1163 particles
129-grain – 12.7 mm	0.0009969	1517 particles

- **Time-step study**

The stability analysis showed that the critical time-step size in semi-Lagrangian RKPM is related to the velocity gradient, which gives a time-step approximately one-tenth of that from the CFL condition (see Figure 9). This yields a much more restrictive stability condition for contact-impact problems compared to the CFL condition. Since the stability condition provides an estimate of the critical time-step based on the result of 1-D VonNeumann analysis with uniform discretization, additional numerical experiments were performed on the critical time-step for penetration modeling. The Trial 1 penetration test is used to investigate the effect of time-step on velocity history, as shown in Figure 52. For the discretization used in the V&V problems, the CFL time-step restriction is approximately 2×10^{-7} sec. Therefore a time-step of 2×10^{-8} sec (one tenth of CFL time-step) is adopted for the low-impact velocity cases. For the high-impact velocity cases, a smaller time-step of 1×10^{-8} sec (one-twentieth of CFL time-step) is used to capture the impact.

- **Dynamic Increase Factor (DIF)**

Material yield stress of the projectile is increased by a DIF to account for strain-rate effects. With a lack of strain rate information and experimental data about the projectile material in the V&V problems, the DIF is defined following Rule and Jones's study (Rule and Jones 1998). This study describes a revised Johnson-Cook model and provides experimental data for the material behavior of steel at high strain rate, as shown in Figure 53. A DIF of 1.2 is applied to the yield stress of low-impact velocity projectiles with velocity less than 610 m/sec and a DIF of 1.5 is applied to the yield stress of high-impact velocity projectiles with velocity greater than 610 m/sec. This adjustment of the yield stress of the projectile is included in input file *NMAP_input.DAT*. A rate-dependent constitutive model, such as the Johnson-Cook model, will be considered in future study.

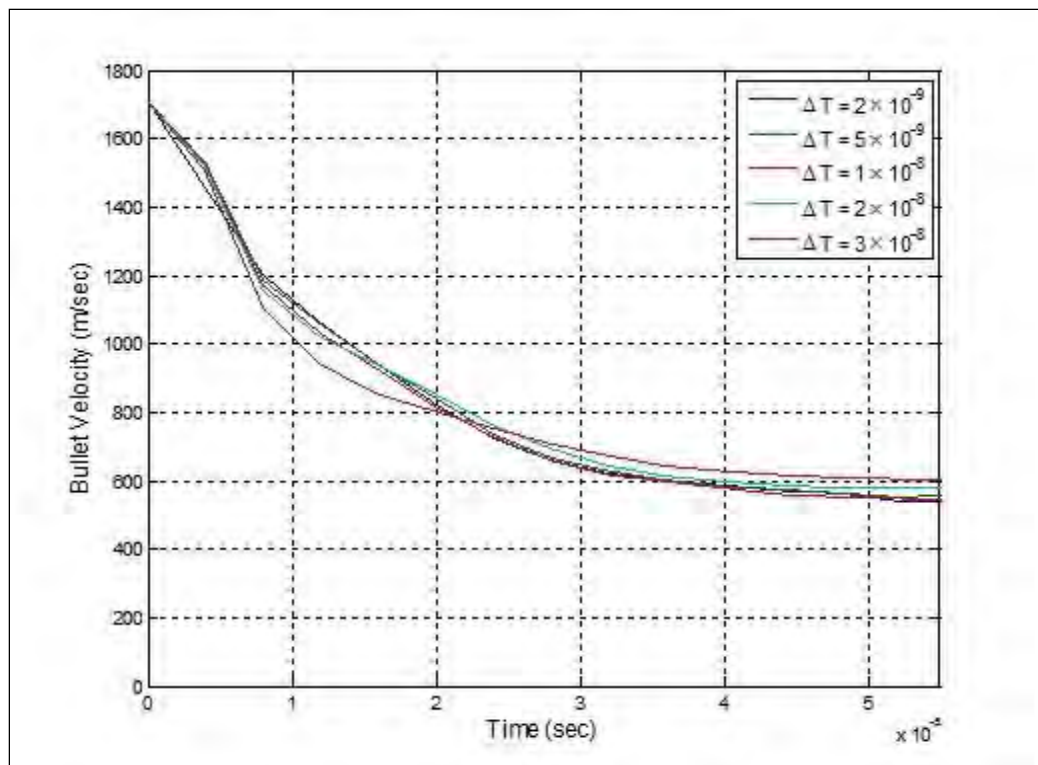


Figure 52. Time-step effect on the velocity history.

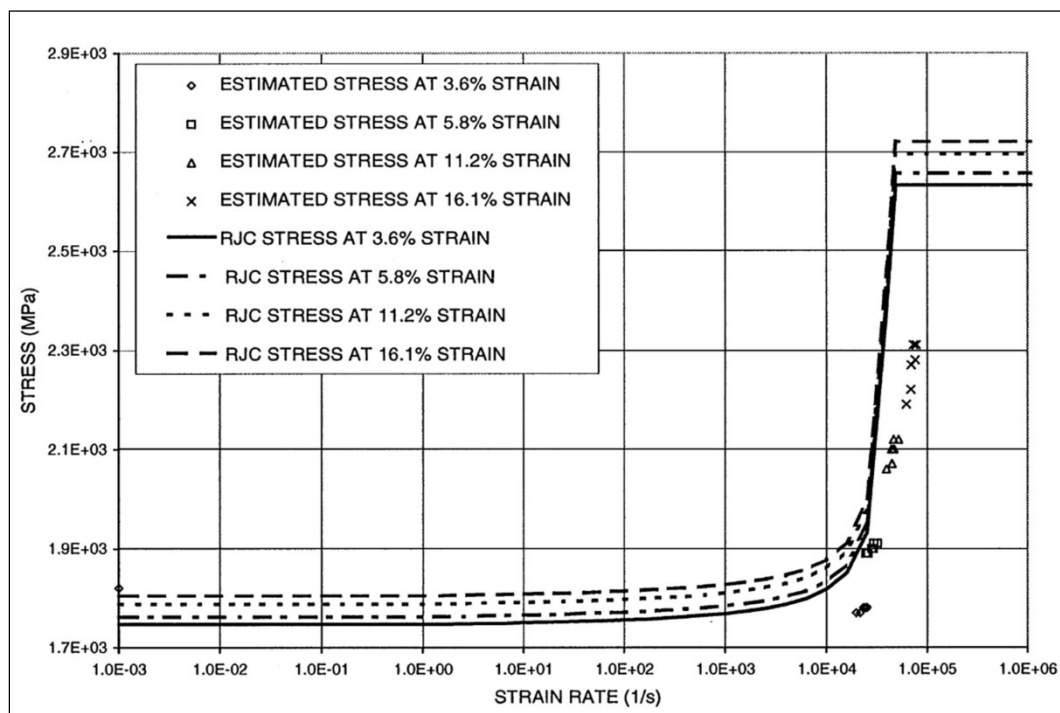


Figure 53. Yield stress versus strain rate for steel (Rule and Jones 1998).

- **Boundary layer correction:**

The numerical contact surface implemented in NMAP should agree with the physical contact surface in order to define the contact event as accurate as possible. A correction of the discretization of the two bodies is done by shrinking half of the length of the boundary element, as illustrated in Figure 54. The outer nodes of the two bodies are moved inward with adjustment of nodal volume.

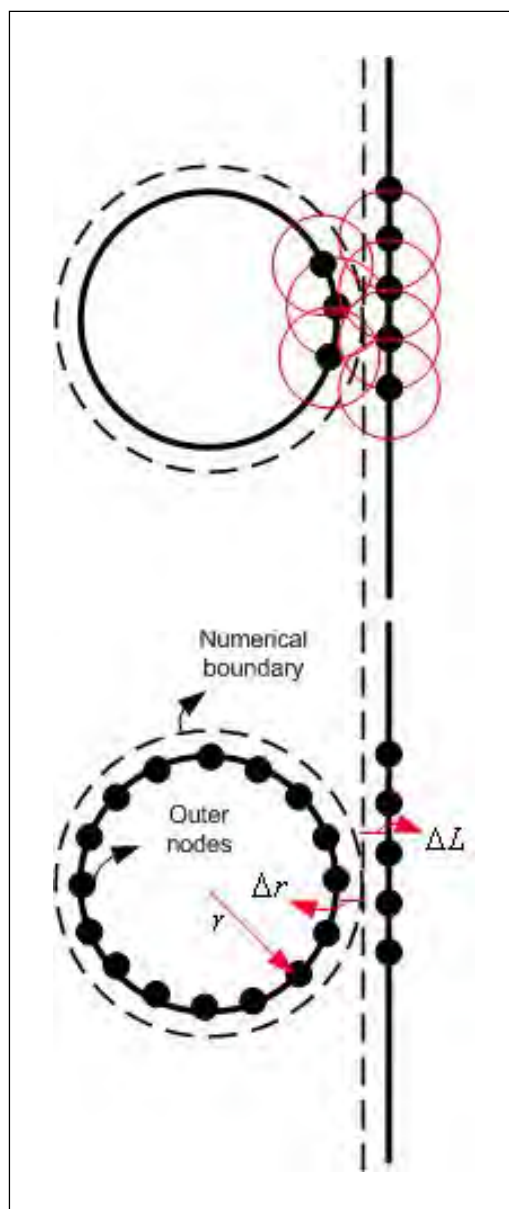


Figure 54. Boundary layer correction.

- **Support size increase of bullet's inner particles:**

Preliminary studies of penetration simulation by NMAP revealed a nonphysical separation of groups of particles during projectile deformation as the result of improper support size, as shown in Figure 55. This phenomenon is called the kernel support instability, which is a numerical instability due to insufficient kernel support coverage of neighboring particles. Consider the group of the first layer of particles on the surface of the projectile to be the “outer particles,” and the remaining particles to be the group of “inner particles.” A remedy to the kernel support instability is undertaken by increasing the kernel support size of the inner particles (Figure 56) in the projectile such that it covers the outer particles. In this manner, it recovers kernel support stability in the projectile under high-velocity impact.

An increase of the support size of the projectile inner particles by a factor of 1.5 has been numerically verified as the optimal adjustment. This support size adjustment was done by using a MATLAB program that modifies the input file *input_dila.DAT*.

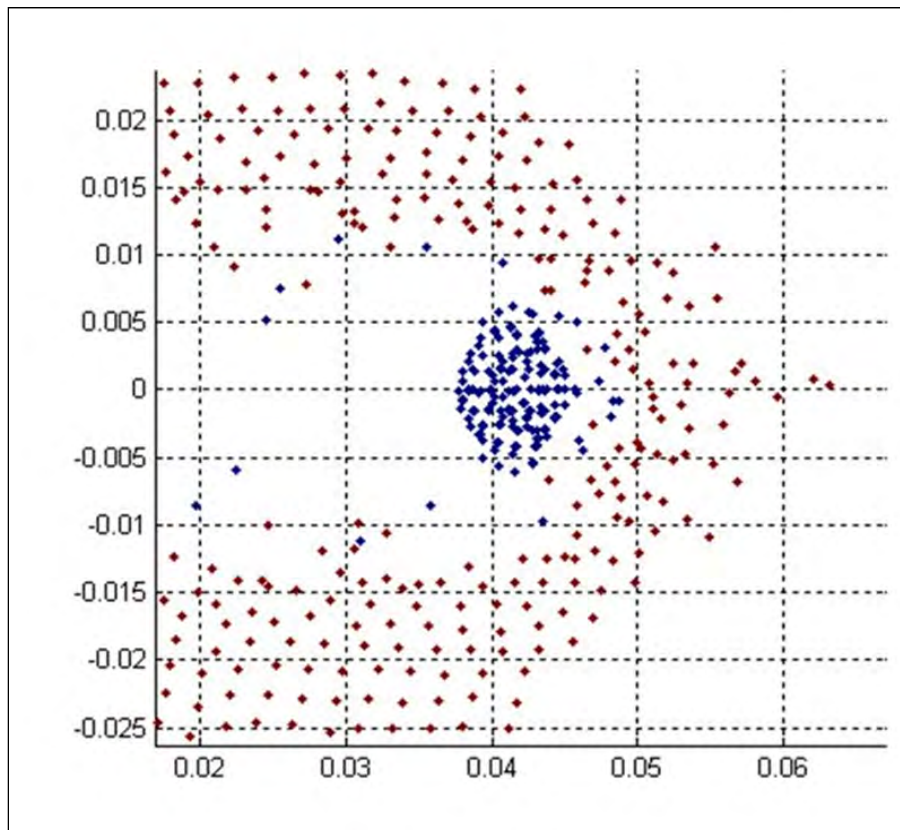


Figure 55. Projectile deformation without support size adjustment.

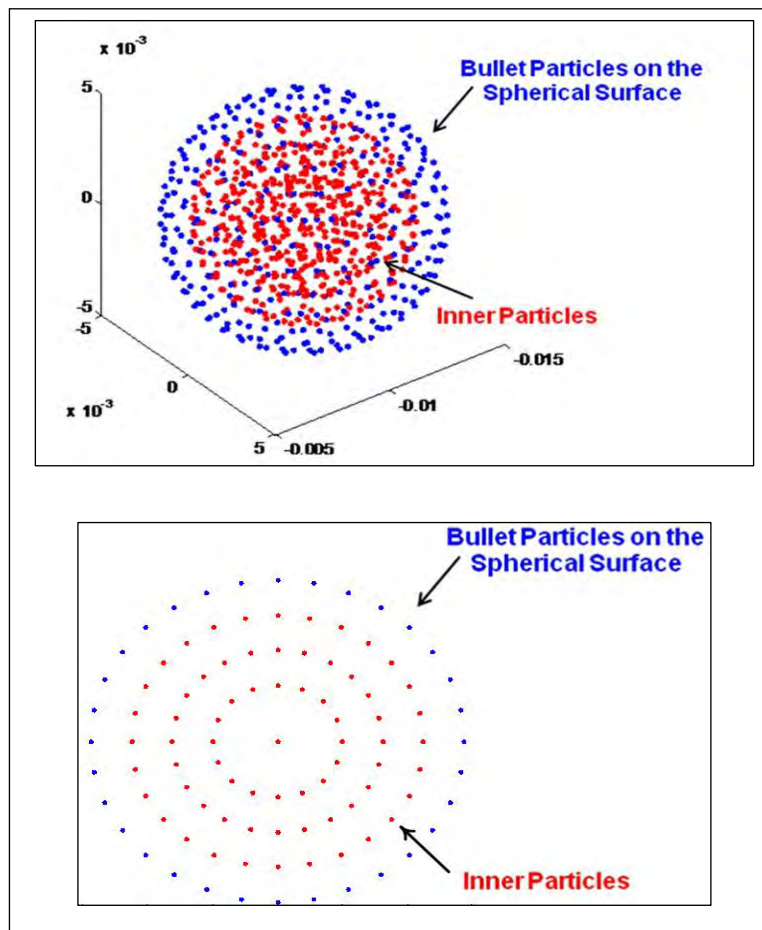


Figure 56. Projectile discretization and cross section.

- **Optimal smoothing zone:**

The optimal smoothing zone for SNNI is defined by half of the nodal distance, as shown in Figure 57. This parameter is implemented directly in the latest version of NMAP.

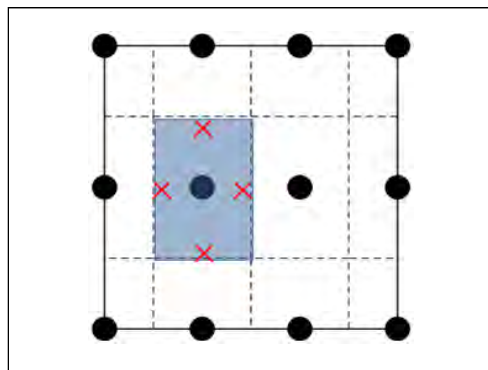


Figure 57. Smoothing zone for SNNI (smoothing zone shaded).

- **Summary of the parametric study:**

Table 8 provides the summary of guidelines for modeling the V&V penetration problems using NMAP.

Table 8. Summary of selected parameters.

Panel Discretization	$1.2 \times 10^{-3} \sim 1.5 \times 10^{-3}$ m (corresponding to non-dimensional wave number 0.045~0.056 ^a)
Bullet Discretization	Nodal distance ratio between discretization in bullet and panel, 1 : 1.4~1.5
Time-step Size	$\Delta T \leq 1/10 * CFL$
Boundary Layer Correction	Move the discretized bullet surface inward by half of nodal spacing
Dynamic Increase Factor (applied to the bullet)	DIF = 1.5 for $V_{\text{impact}} > 610$ m/sec DIF = 1.2 for $V_{\text{impact}} < 610$ m/sec
Support Size Adjustment	Increase by a factor of 1.5 for bullet's inner particles
Smoothing Zone Size	Coefficient * Nodal distance, Coefficient = 0.5

^a The non-dimensional wave number is normalized by the major wavelength of the system. The non-dimensional wave number smaller than 0.1 gives an accurate result when RKPM with SCNI is used (You et al. 2002), which is used as a reference for SNNI. More investigation on the stability condition will be made in the near future.

Summary of numerical simulation of V&V problems

Eighteen penetration experiments were conducted by ERDC and are compared to NMAP simulations. Comparison of exit velocities and velocity reductions for each test are given in Table 9. Figures 58 to 60 provide a comparison of the V&V experimental data and the NMAP numerical results for each size of projectile, 32-grain, 86-grain and 129-grain, respectively. Figure 61 (a), (b) and (c) represent respectively the impact face, exit face and hole of the damaged panel of Run 1. Each figure was obtained by removing all particles that have tensile damage greater than 0.8, and velocity greater than 5 m/sec. Since the panel is discretized with layers of particles through the thickness, the layer that presents the smallest crater is used to specify the hole in the panel. For analysis, the arrows drawn on each figure are measured, and extreme values are considered as minimum and maximum dimensions of the impact crater, exit crater, and hole. These are summarized in Table 10. Projectile and panel mass loss and crater debris weights are shown in Table 11. The mass loss criterion in the

Table 9. Exit velocity comparison.

		Pre-Test				Post-Test			
Run#	Test #	Panel	Projectile	Actual Panel Thickness (in.)	Impact Velocity (ft/s)	Exit Velocity (ft/s)	Velocity Reduction (%)	Exit Velocity (ft/s) NUMERICAL	Velocity Reduction (%) NUMERICAL
4	090806-02	Nominal 1.5" Thick	129 gr 1/2" sphere	1 5/8	5636	2597.00	53.92%	2119.42	62.39%
8	090819-01			1 9/16	1337	0.00	100.00%	4.56	99.66%
15	090527-06		86 gr 7/16" sphere	1 7/16	2616	50.00	98.09%	-14.27	100.00%
trial 1	091013-03			1 9/16	5604	2246.00	59.92%	1873.69	66.57%
7	091014-02		32 gr 5/16" sphere	1 9/16	6718	177.00	97.37%	697.83	89.61%
3	090806-01			1 9/16	1985	0.00	100.00%	2.33	99.88%
14	090917-01	Nominal 1" Thickness	129 gr 1/2" sphere	1	1582	75.00	95.26%	21.52	98.64%
13	090904-02		86 gr 7/16" sphere	1	3657	1787.00	51.13%	1051.84	71.24%
9	090819-02			1	1767	0.00	100.00%	5.51	99.69%
12	090904-01			1	884	0.00	100.00%	13.06	98.52%
trial 2	090911-03			1 1/16	1892	0.00	100.00%	-7.19	100.00%
16	091014-01		32 gr 5/16" sphere	1 1/16	6521	1284.00	80.31%	2464.57	62.21%
11	090903-01			1 1/16	3015	80.00	97.35%	36.22	98.80%
6	090807-02	Nominal 1/2" Thickness	129 gr 1/2" sphere	9/16	1516	654.00	56.86%	383.20	74.72%
2	090805-02			5/8	377	0.00	100.00%	26.57	92.95%
10	090902-03		86 gr 7/16" sphere	9/16	859	0.00	100.00%	67.03	92.20%
1	090805-01		32 gr 5/16" sphere	11/16	2868	976.00	65.97%	296.59	89.66%
5	090807-01			17/32	785	0.00	100.00%	12.20	98.45%

Convert inches to millimeters as (·)×25.4.

Convert feet per second to meters/second as (·)×0.3048.

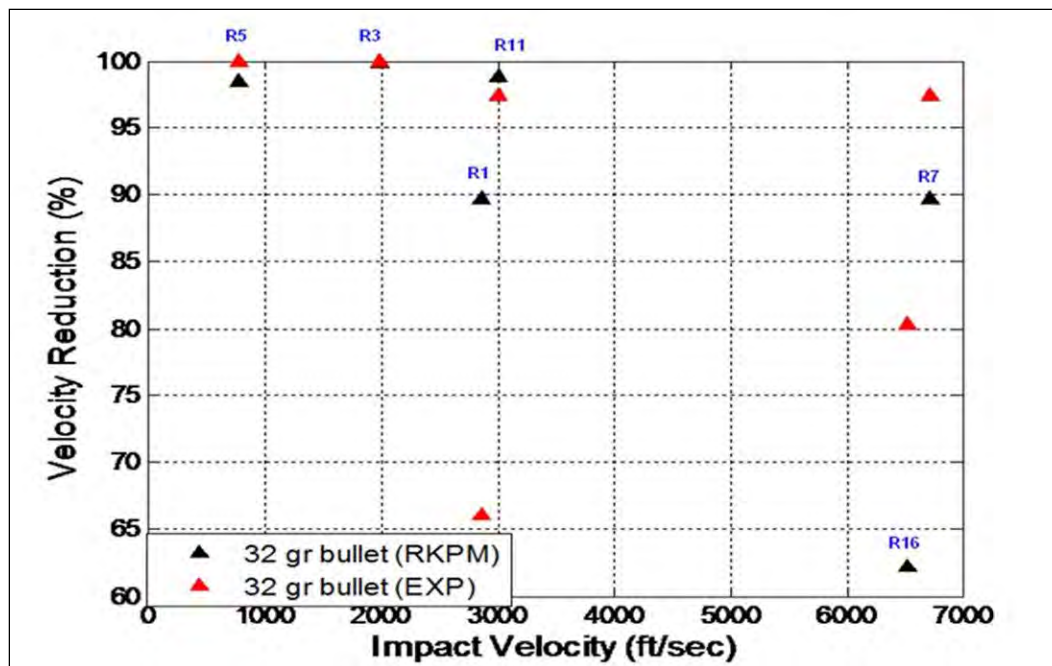


Figure 58. Comparison of velocity reduction for V&V tests using 32-grain projectiles.

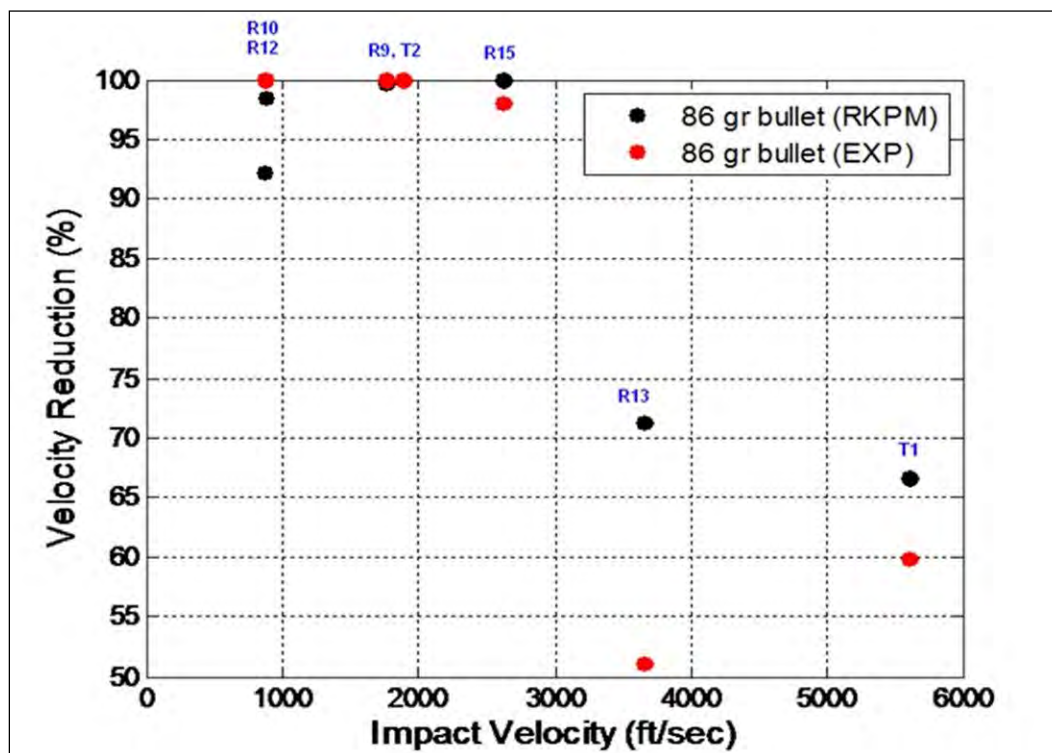


Figure 59. Comparison of velocity reduction for V&V tests using 86-grain projectiles.

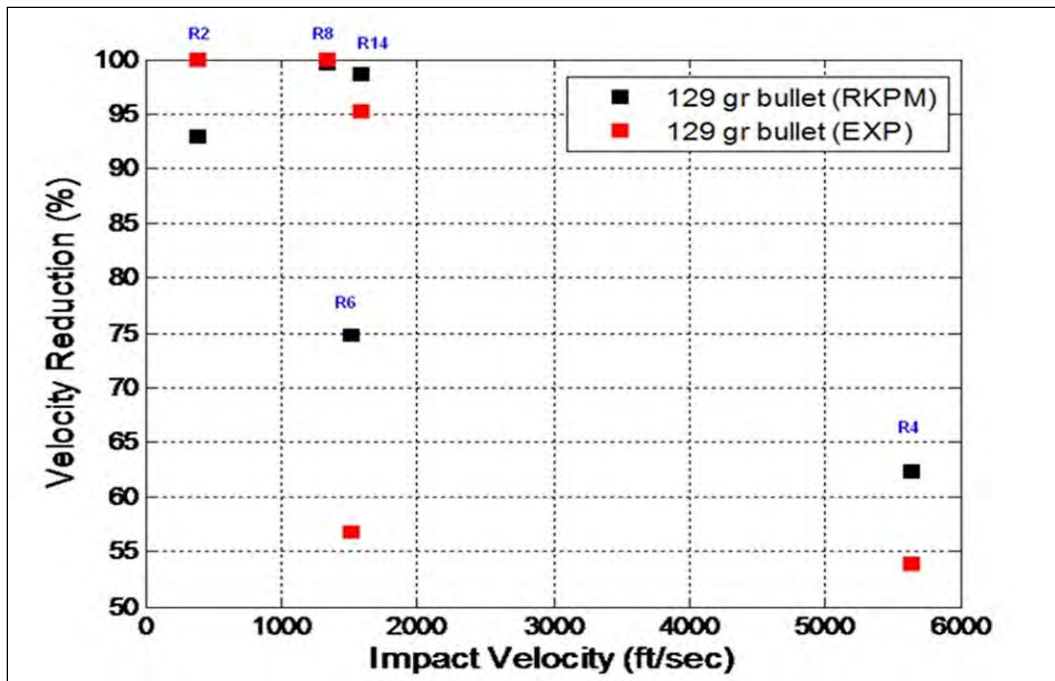


Figure 60. Comparison of velocity reduction for V&V tests using 129-grain projectiles.

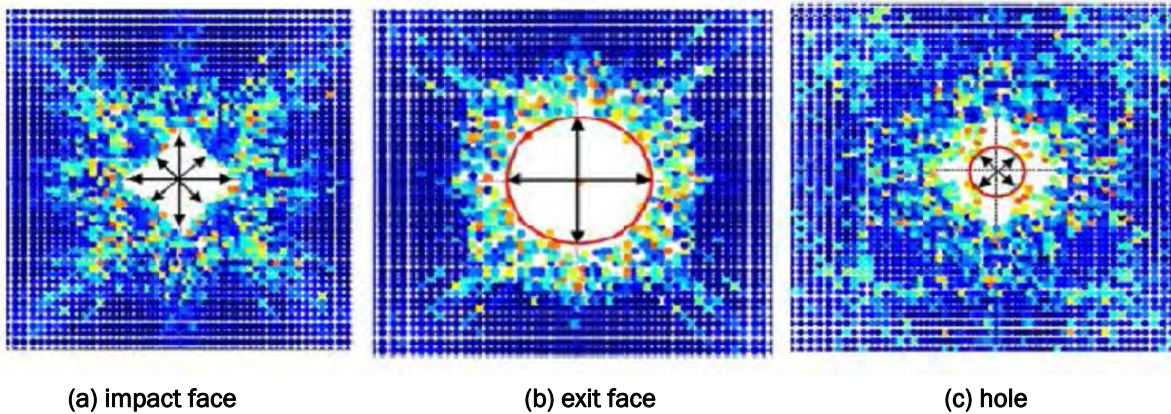


Figure 61. Illustration of measurement of crater sizes and hole dimensions.

panel is defined by removing all particles that have tensile damage greater than 0.8, and velocity greater than 5 m/sec. No damage criterion is defined for the projectile. Therefore, the mass loss of the projectile is measured by removing the particles that separate from the projectile during the impact process.

Velocity histories and damage patterns are presented for four V&V tests (Runs 6, 7, 10 and 16). Run 6 describes the impact of a 129-grain projectile of low initial velocity onto a thin panel of nominal 12.7-mm thickness. Run 7 describes the impact of a 32-grain projectile of high initial velocity onto a

Table 10. Crater and hole diameter comparison.

		Post-Test											
Run#	Test #	Impact Crater Diameter MIN (in.)	Impact Crater Diameter MAX (in.)	Exit Crater Diameter MIN (in.)	Exit Crater Diameter MAX (in.)	Hole Diameter MIN (in.)	Hole Diameter MAX (in.)	Impact Crater Diameter MIN NUMERICAL (in.)	Impact Crater Diameter MAX NUMERICAL (in.)	Exit Crater Diameter MIN NUMERICAL (in.)	Exit Crater Diameter MAX NUMERICAL (in.)	Hole Diameter MIN NUMERICAL (in.)	Hole Diameter MAX NUMERICAL (in.)
4	090806-02	4 1/8	5 1/8	4 1/8	4 1/4	1 1/4	1 9/16	2 23/31	4 1/96	4 41/76	6 37/93	1 3/26	1 10/71
8	090819-01	2 1/32	2 3/16	5/16	3	0	0	1 5/6	2 28/73	15/29	3 19/58	13/27	53/94
15	090527-06	2 3/4	2 3/4	3 3/4	3 3/4	1/2	1/2	2 9/73	2 41/42	3 60/67	3 9/10	67/87	27/35
trial1	091013-03	4 3/16	4 5/8	4 7/8	5 3/4	1	1 1/16	4 33/65	5 5/22	5 14/29	5 55/58	1 41/55	3 1/4
7	091014-02	4 1/2	4 9/16	4 1/2	4 1/2	5/8	3/4	2 1/17	4 15/71	4 9/14	4 59/62	11/12	85/86
3	090806-01	1 7/8	2 1/4	0	0	0	0	1 37/73	2 21/50	2 1/41	2 37/69	0	0
14	090917-01	1 15/16	2 13/16	3 3/4	3 15/16	1/2	5/8	2 7/95	3 37/94	3 31/55	3 25/39	9/13	49/58
13	090904-02	3 3/16	3 1/2	3 7/18	3 11/16	7/8	1	2 63/67	3 31/72	3 77/90	4 7/11	1 16/77	1 13/51
9	090819-02	2 1/8	2 7/16	2 13/16	3 1/16	7/16	9/16	2 21/73	2 27/85	3 7/67	3 17/32	4/7	47/79
12	090904-01	1 9/16	1 5/8	1/4	4 7/16	0	0	1 35/54	1 20/27	9/41	3 29/54	27/49	11/19
trial2	090911-03	2 5/16	2 13/16	3 7/16	4 1/4	7/16	1/2	1 80/83	2 13/27	3 3/13	3 30/61	23/28	39/47
16	091014-01	3 3/8	4 5/16	3 5/16	4 3/8	7/8	1 1/6	2 58/61	3 56/97	4 7/96	4 8/15	1 5/36	1 13/85
11	090903-01	2 9/16	2 11/16	3 1/8	3 5/8	7/16	9/16	1 31/41	2 39/50	2 39/40	3 30/49	55/64	11/12
6	090807-02	1 11/16	1 13/16	2 5/8	2 11/16	9/16	5/8	1 49/96	1 69/77	1 9/11	2 17/20	60/73	81/98
2	090805-02	13/16	13/16	5/8	4	0	0	1 7/80	1 13/49	2 53/83	2 32/45	41/77	25/41
10	090902-03	1	1 5/8	2 9/16	3 3/16	1/2	9/16	2 4/25	2 9/28	1 42/47	2 1/17	8/11	35/46
1	090805-01	1 5/8	1 7/8	2	2 1/8	1/2	5/8	1 9/19	1 63/76	1 34/37	2 1/11	46/81	43/68
5	090807-01	13/16	13/16	1 11/16	2 1/4	0	0	1 1/5	1 20/99	1 13/27	1 3/5	32/63	13/25

Table 11. Projectile and panel mass loss and crater debris weight comparison.

Run#	Test #	Post-Test							
		Projectile Mass POST-test (grains)	Panel Weight POST-test (lb.)	Impact Crater Debris weight (lb.)	Exit Crater Debris weight (lb.)	Total Debris weight (lb.)	Projectile Mass POST-test NUMERICAL (grains)	Panel Weight POST-test NUMERICAL (lb.)	Total Debris weight NUMERICAL (lb.)
4	090806-02	127.3		0.152	0.2767487	0.429	127.9	17.895	0.207
8	090819-01	128.5		0.011	0.001	0.012	127.9	18.053	0.031
15	090527-06						86.5	16.632	0.090
trial 1	091013-03	85		~0.10	~0.32	0.420	86.5	17.469	0.714
7	091014-02	11	20.192	0.116	0.292	0.409	30.5	17.933	0.125
3	090806-01	31.3		0.006	0.000	0.006	30.4	17.663	0.042
14	090917-01	128.1	12.81	0.015	0.117	0.131	127.9	11.434	0.060
13	090904-02	85.3		0.047	0.123	0.170	86.5	11.487	0.113
9	090819-02	85.8		0.015	0.094	0.109	86.5	11.525	0.063
12	090904-01	86		0.006	0.003	0.010	86.5	11.630	0.020
trial 2	090911-03	85.9		~0.02	~0.14	0.160	86.5	12.237	0.056
16	091014-01	13	13.386	0.047	0.143	0.190	30.5	12.204	0.114
11	090903-01			0.019	0.076	0.096	30.5	12.394	0.043
6	090807-02	128.5		0.007	0.053	0.060	127.9	4.887	0.106
2	090805-02	128.3		0.001	0.003	0.005	127.9	7.316	0.017
10	090902-03	85.9		0.008	0.048	0.056	86.5	6.586	0.020
1	090805-01	31.2		0.012	0.032	0.044	30.5	8.019	0.040
5	090807-01						30.4	6.243	0.010

thick panel of nominal 38.1-mm thickness. Run 10 describes the impact of an 86-grain projectile of low impact velocity onto a thin panel of nominal 12.7-mm thickness. Run 16 describes the impact of a 32-grain projectile of high impact velocity onto a panel of nominal 25.4-mm thickness. The velocity history curves of Runs 6, 7, 10 and 16 are shown in Figures 62, 64, 66, and 68, respectively.

The damage patterns on the impact face and exit face of Runs 6, 7, 10 and 16 are also provided in Figures 63, 65, 67, and 69, respectively. Provided is a comparison of the craters between the numerical simulation and the experimental observation.

Comparisons between macroscale and multiscale AFC models

In this study, two sets of V&V tests are adopted for comparison. Since in this study the same dimensions for both projectiles and panels are used but with different impact velocities, the comparison is identified based on the impact velocity of the projectiles.

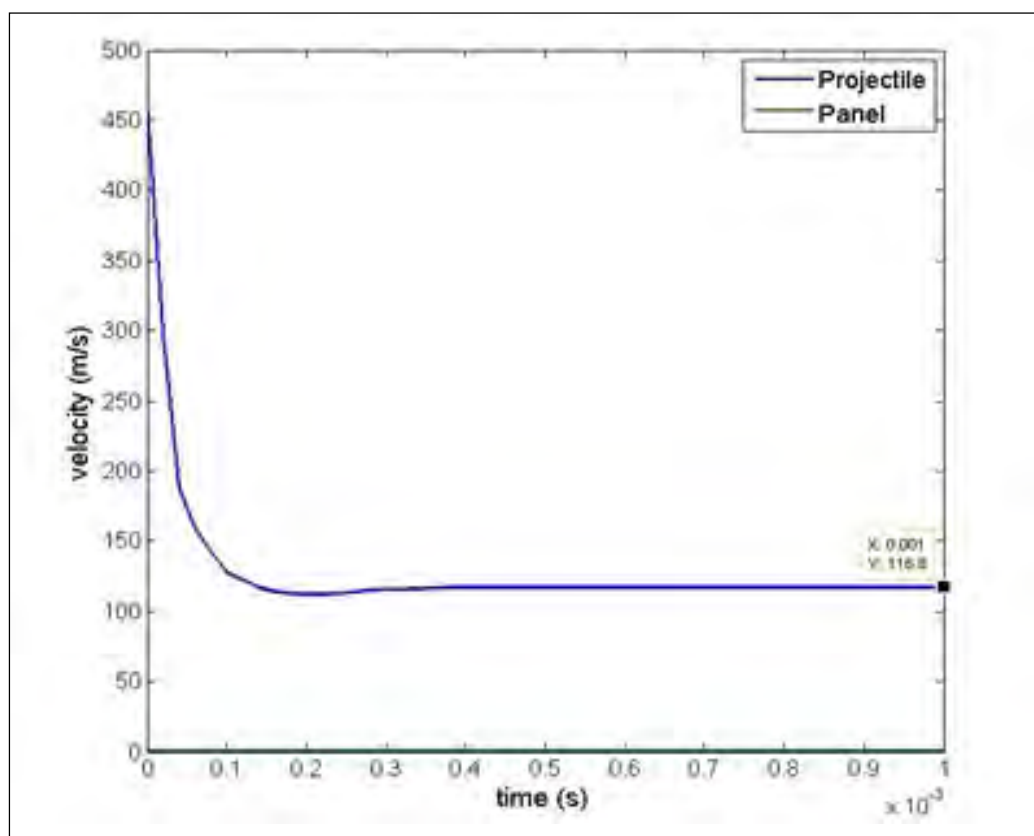


Figure 62. Velocity history of Run 6.

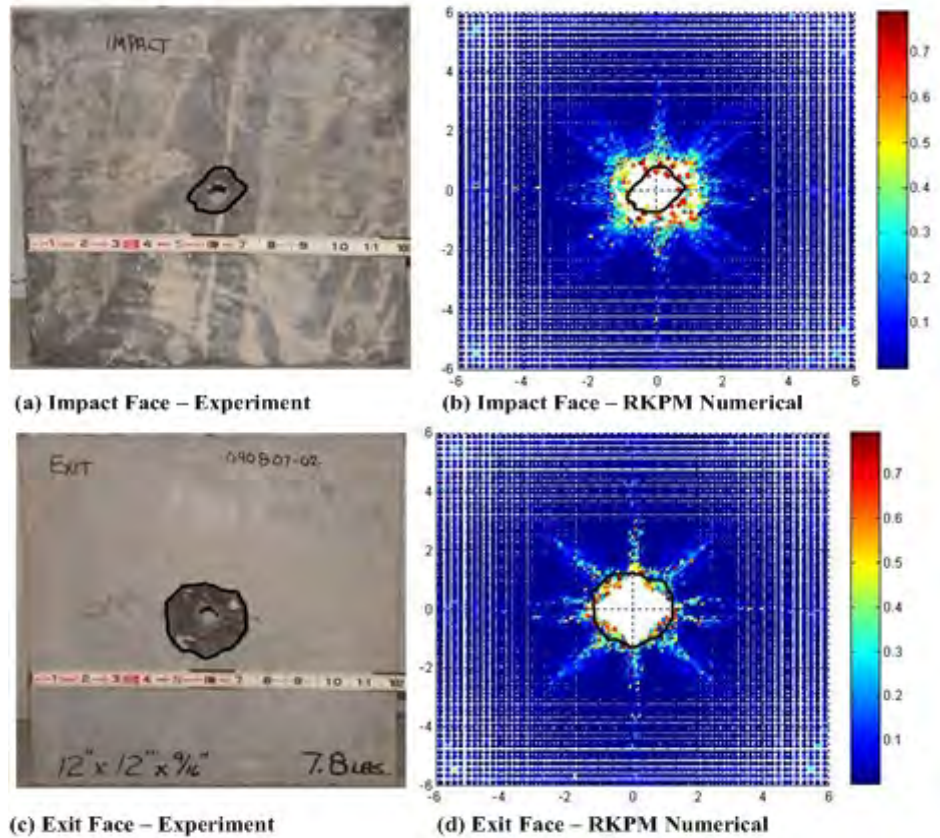


Figure 63. Comparison of damage pattern for Run 6.

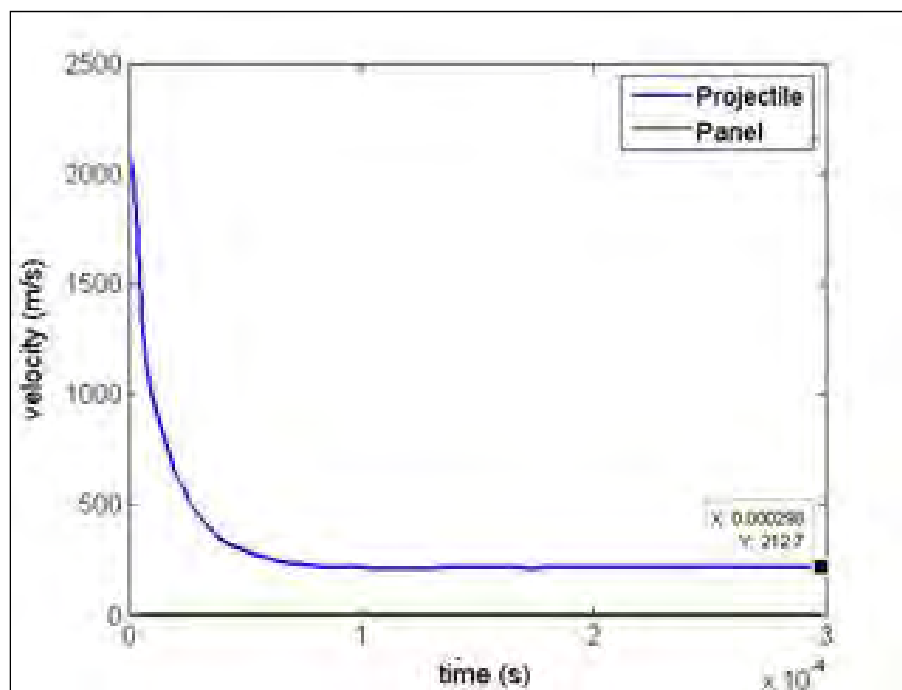


Figure 64. Velocity history of Run 7.

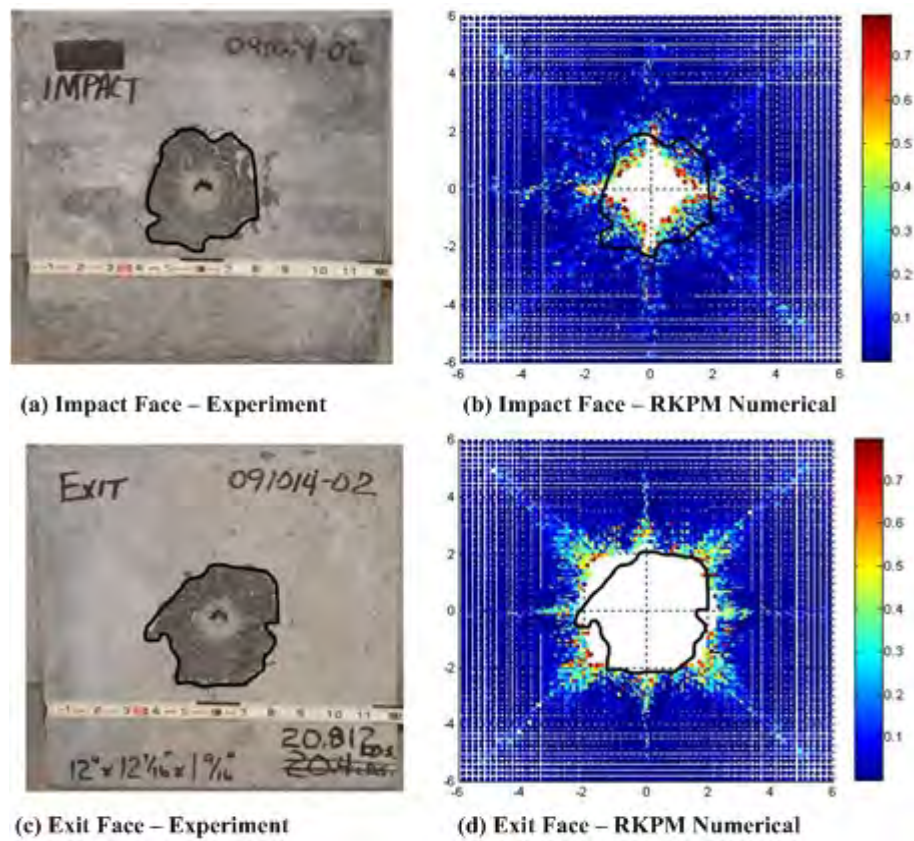


Figure 65. Comparison of damage pattern for Run 7.

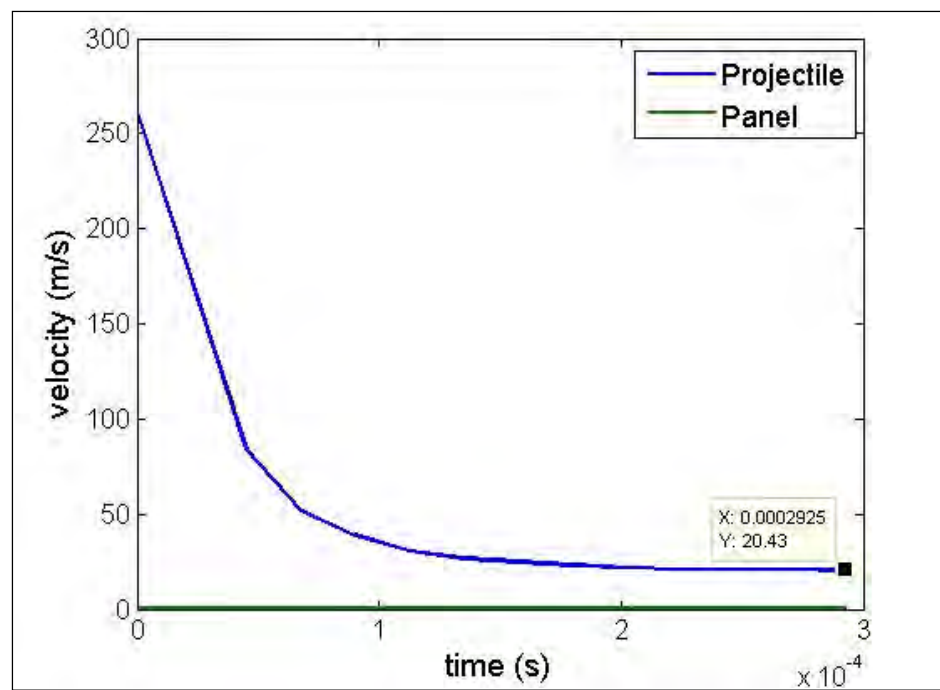


Figure 66. Velocity history of Run 10.

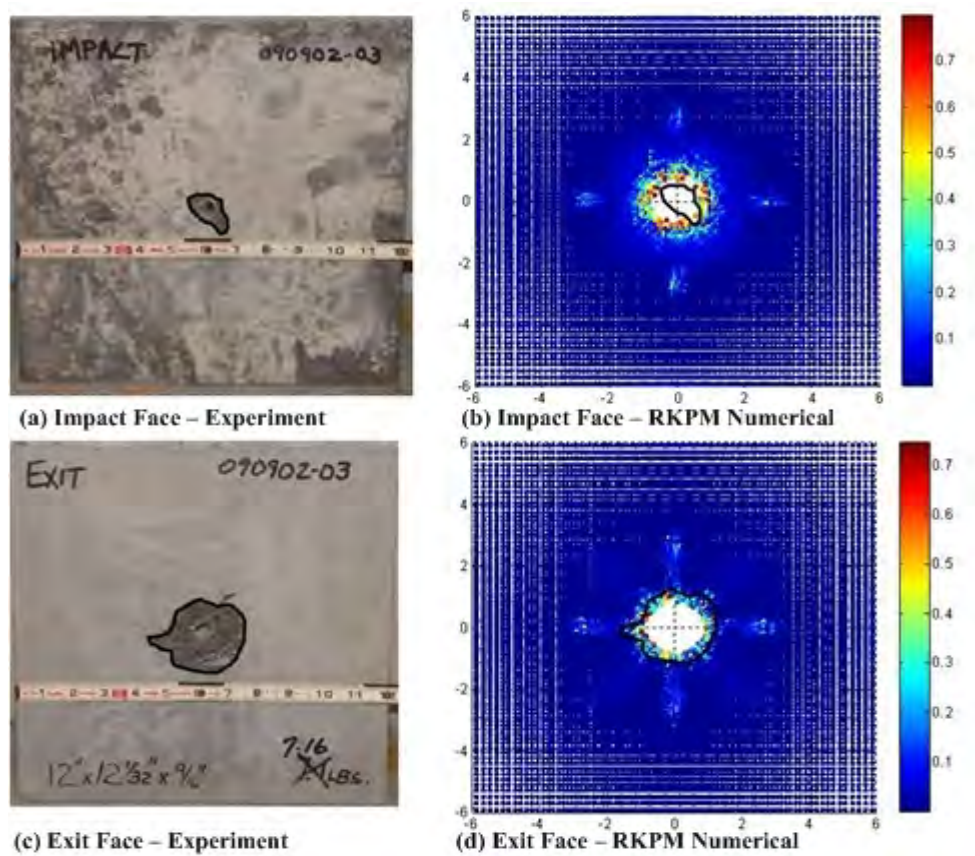


Figure 67. Comparison of damage pattern for Run 10.

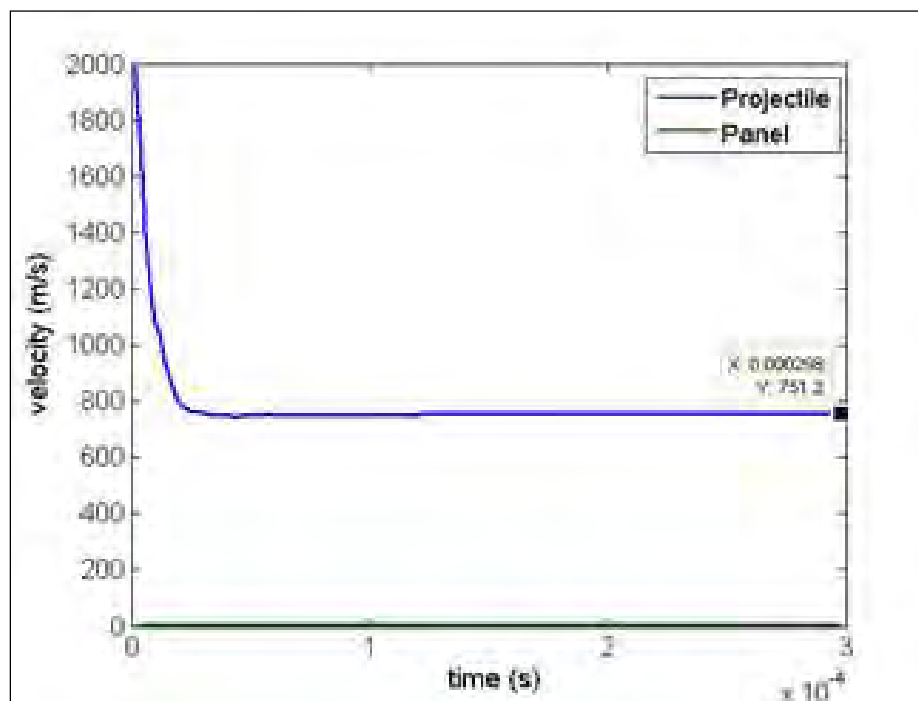


Figure 68. Velocity history of Run 16.

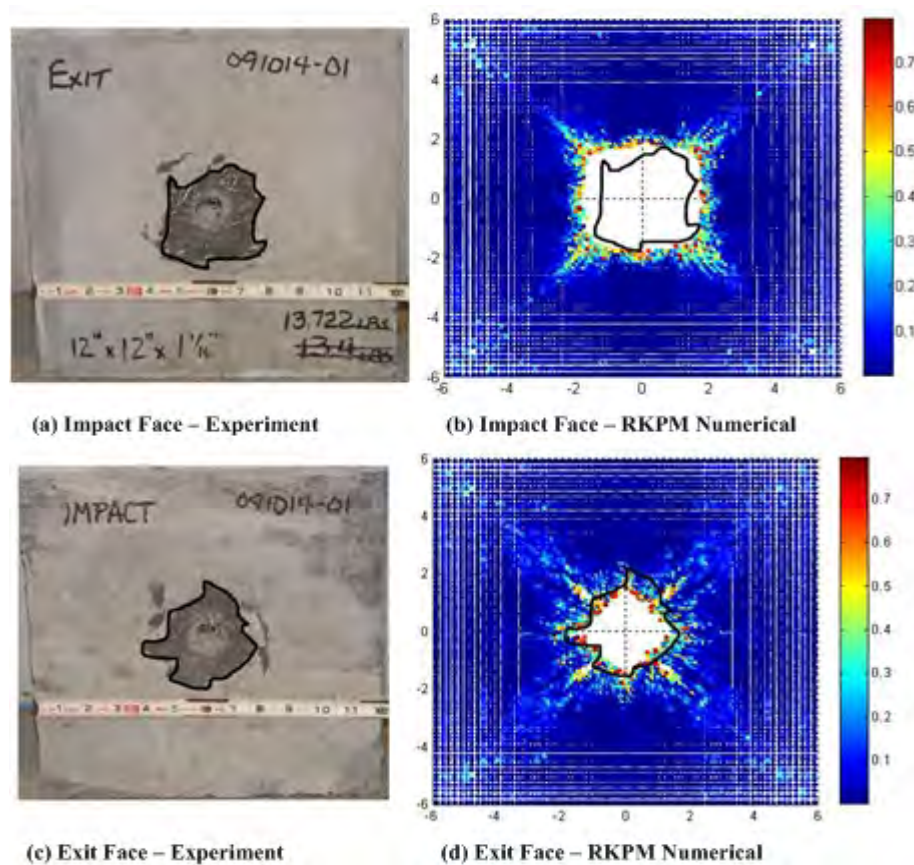


Figure 69. Comparison of damage pattern for Run 16.

Different damage patterns of multiscale and macroscale AFC models are given in Figures 70 through 74. Table 12 lists the corresponding exit velocities. For the multiscale AFC model, the damage patterns include shear and tensile damage, while only shear damage is considered in macroscale AFC model. Therefore, the figures only exhibit the shear damage pattern for both the macroscale and multiscale AFC models. Hence, the multiscale AFC model is expected to generate a larger damage region than the macroscale AFC model. As the impact wave of the projectile propagates to the back of the concrete panel, then bounces back, it causes tensile damage and therefore induces a larger damage zone in the exit face. As can be seen in Figures 70 through 74, the multiscale AFC model predicts larger craters than those predicted by the macroscale AFC model. For Run 7, the diagram of the multiscale AFC model seems to generate a smaller crater than the macroscale one. This is because the tensile damage patterns are not drawn in the comparison.

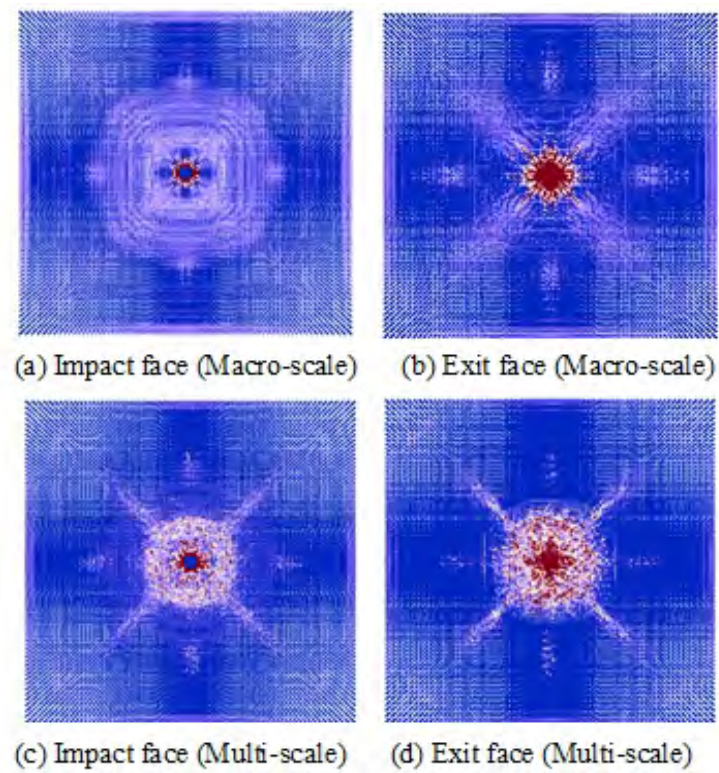


Figure 70. Damage pattern of Run 12.

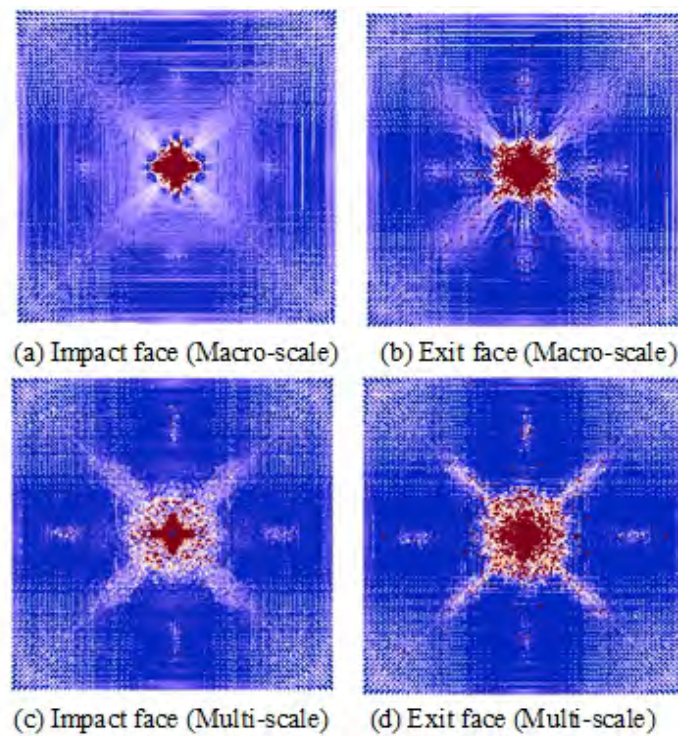


Figure 71. Damage pattern of Run 9.

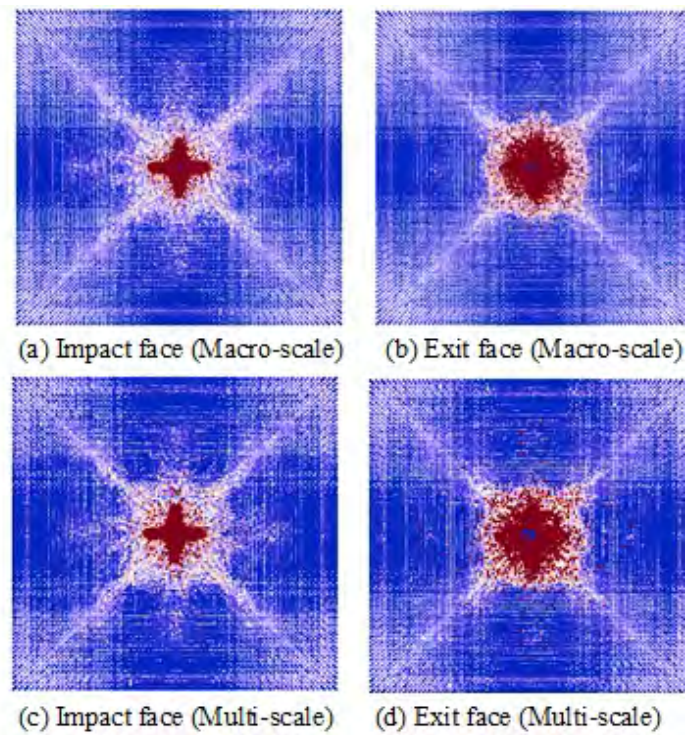


Figure 72. Damage pattern of Run 13.

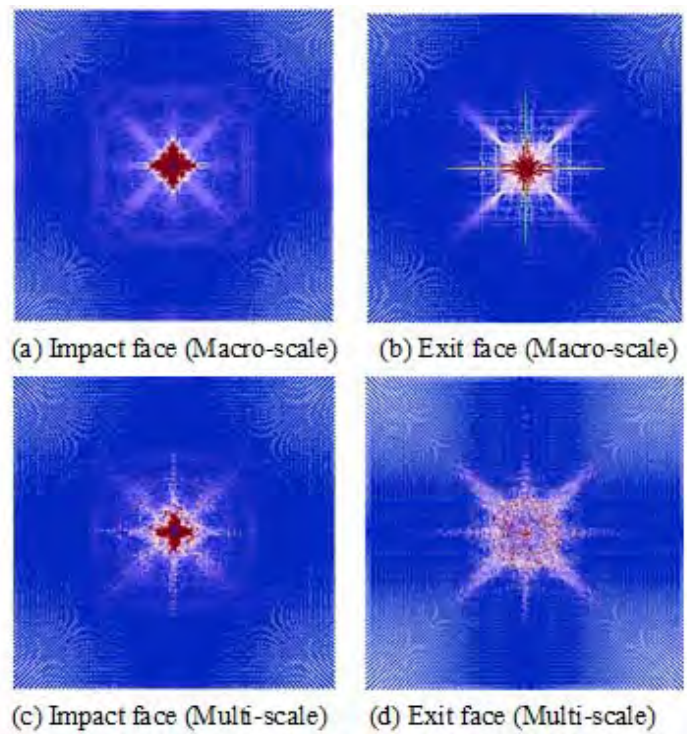


Figure 73. Damage pattern of Run 3.

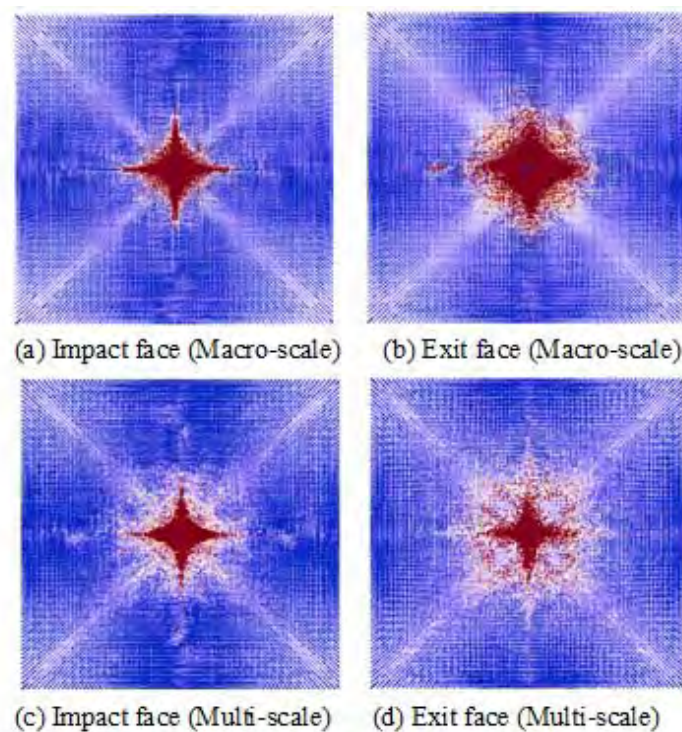


Figure 74. Damage pattern of Run 7.

Table 12. Comparisons of exit velocity between macroscale, multiscale AFC models and experimental measurement.

	Macroscale AFC Model (m/s)	Multiscale AFC Model (m/s)	Experiments (m/s)
Run 12	-2.62	3.98	0.00
Run 9	-0.29	1.68	0.00
Run 13	350.60	320.60	544.68
Run 3	0.65	0.71	0.00
Run 7	129.98	212.70	53.95

Empirical formula extracted from penetration V&V numerical and experimental data

Figure 75 illustrates the typical velocity reduction characteristics obtained from the numerical simulations using an 86-grain projectile with various panel thicknesses and impact velocities. Here, a general formula is constructed for describing the projectile velocity reduction based on numerical and experimental data of the V&V problems. To formulate the relationship among the three parameters, i.e., velocity and size of the projectile and the panel thickness two types of criteria are considered for

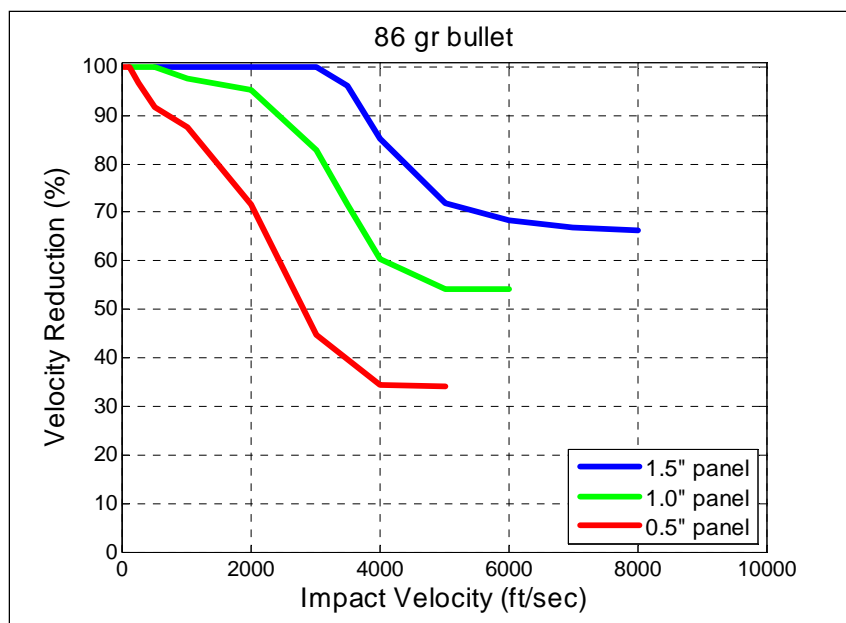


Figure 75. Velocity reduction rate with various thicknesses and impact velocities.

representing the projectile energy. These are velocity and kinetic energy criteria, which are proposed to quantify the behavior of the projectiles.

- **Velocity criteria:**

Based on the V&V problems, two observations are made from the numerical simulations and experimental results.

- If the impact velocity of the projectile is less than a threshold, the projectile will stop inside the panel or bounce back. In order for the projectile to perforate the panel, a minimum projectile velocity is required.
- Thicker panels yield greater velocity reduction, and therefore the minimum velocity required to perforate is a function of panel thickness.

Figures 76 to 78 show the comparison between numerical and experimental results using different projectile sizes. Exit velocity versus normalized impact velocity (normalized by the panel thickness) is plotted. Table 13 lists the minimum normalized impact velocity required for perforation, as determined from the numerical and experimental results. For the tests with a 32-grain projectile, larger discrepancy exists between the numerical and experimental results, while the simulation results for 86-grain and 129-grain projectile cases agree well with the experimental data.

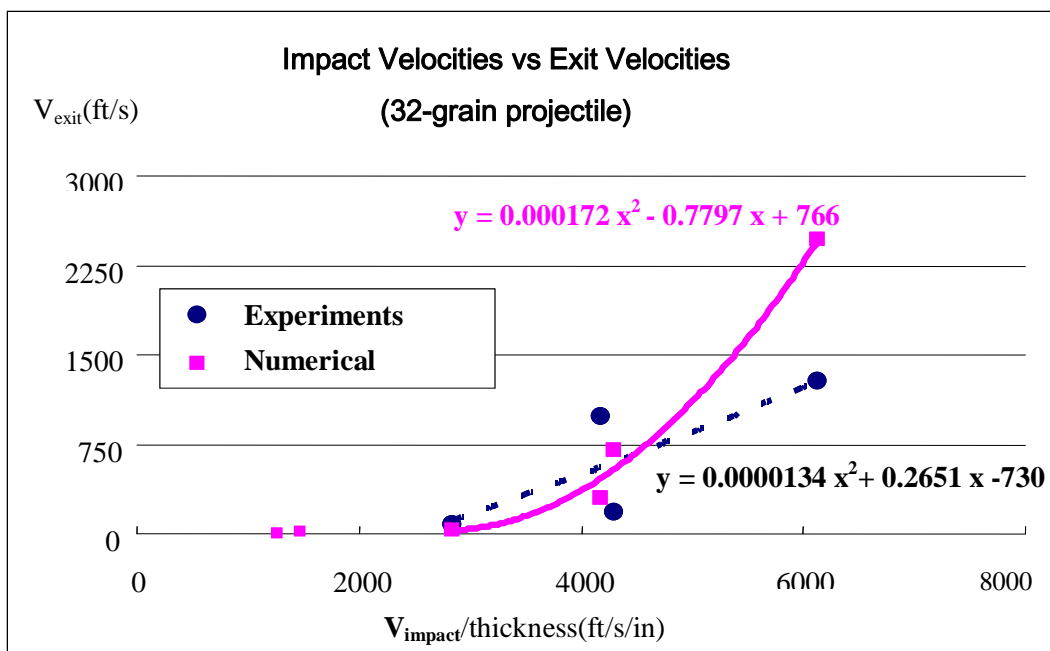


Figure 76. Normalized impact velocity vs. exit velocity (32-grain projectile).

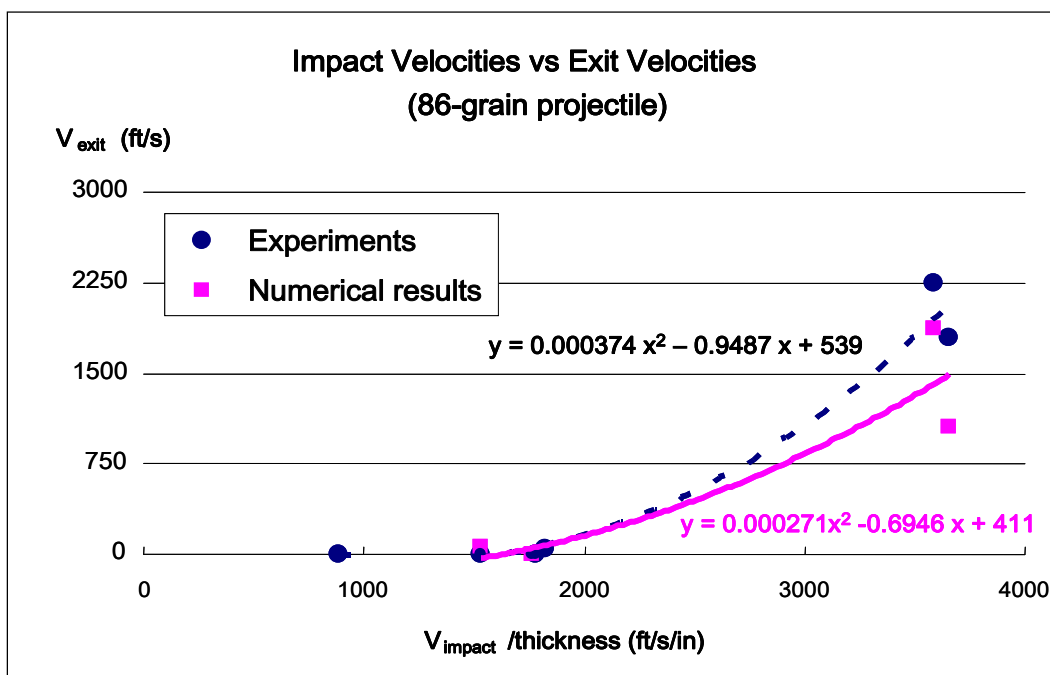


Figure 77. Normalized impact velocity vs. exit velocity (86-grain projectile).

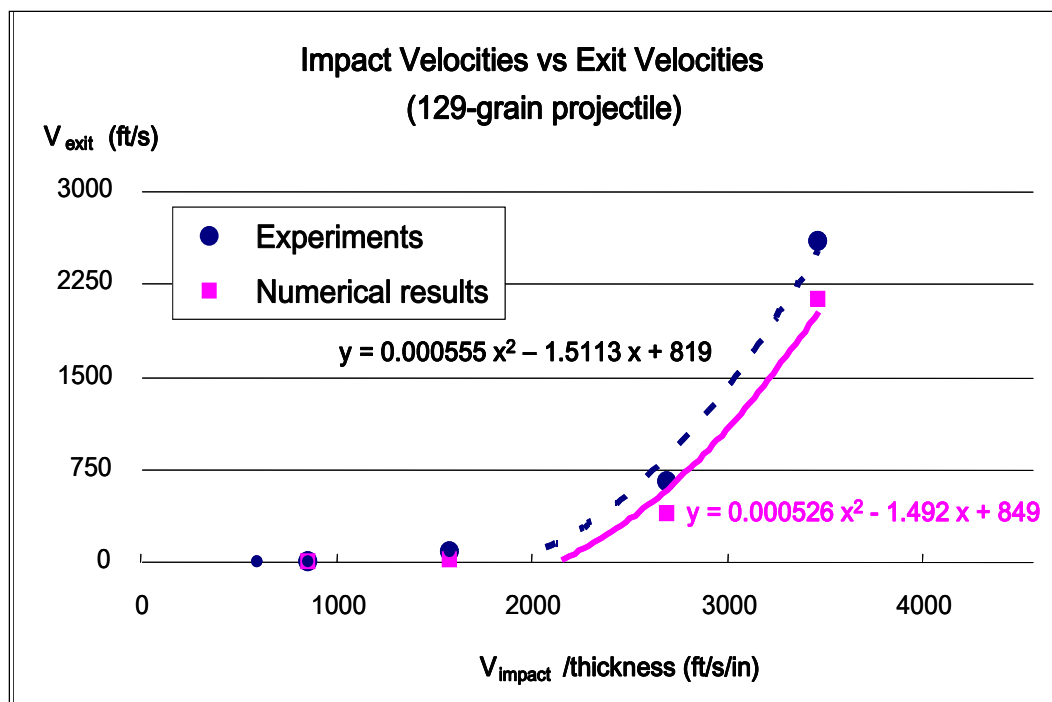


Figure 78. Normalized impact velocity vs. exit velocity (129-grain projectile).

Table 13. Minimum required normalized velocity.

$\left(\frac{V_{impact}}{thickness} \right)_{required}$	32-grain projectile	86-grain projectile	129-grain projectile
RKPM	3093 (ft/s/in.)	1636 (ft/s/in.)	2049 (ft/s/in.)
Experiments	2451(ft/s/in.)	1678 (ft/s/in.)	1976 (ft/s/in.)

Convert ft/s/in to m/s/mm as $(\cdot) \times 0.012$

- **Kinetic energy criterion:**

The following assumptions based on the numerical and experimental data are made for the construction of an empirical formula using kinetic energy criterion.

- Energy loss occurs for the projectile during penetration of the concrete panel. If the projectile's impact kinetic energy is less than a threshold, it will not perforate through the panel. Consequently, a minimum kinetic energy is required for perforation.
- The minimum required kinetic energy is also dependent on the panel thickness. The thicker the panel, the larger the reduction of kinetic energy.

Based on the previous information, an empirical formula is constructed in the following form

$$K_{exit} = R_d \frac{K_{impact}}{t} - \bar{K}_{cr} \quad (109)$$

where K_{impact} and K_{exit} are the impact and exit kinetic energy of the projectile, \bar{K}_{cr} is the critical kinetic energy for the projectile to perforate the panel, t is the thickness of the panel and R_d is the kinetic energy reduction factor, which is

$$R_d = \frac{c}{t} \quad (110)$$

where c is a constant that may be related to the material properties of the projectile and panel.

By least-squares fitting of the previous formula to the numerical and experimental results as plotted in

Figure 79, it can be seen that the curves generated from the numerical and experiment data show similar trends, although discrepancies exist. Table 14 lists the values of the characterized coefficient c and the critical kinetic energy $\bar{K}_{critical}$. These procedures will be performed more rigorously based on regression analysis or other well developed mathematical tools in the future.

Summary and discussions

Several numerical simulations were first carried out to determine certain optimum model parameters. All other V&V numerical results were based on use of these optimal values. The DIF is adopted since the J2 plasticity model for the projectile does not consider rate effects to instantaneously adjust yield stress with the changing of strain rate. For instance, on Runs 7 and 16, the experimental mass loss of the projectiles is about 60%, while numerically only a small amount of mass is lost. Both cases have extremely high impact velocity but with the smallest projectile size. Physically, the mass loss may be due to the melting of the projectile and subsequent

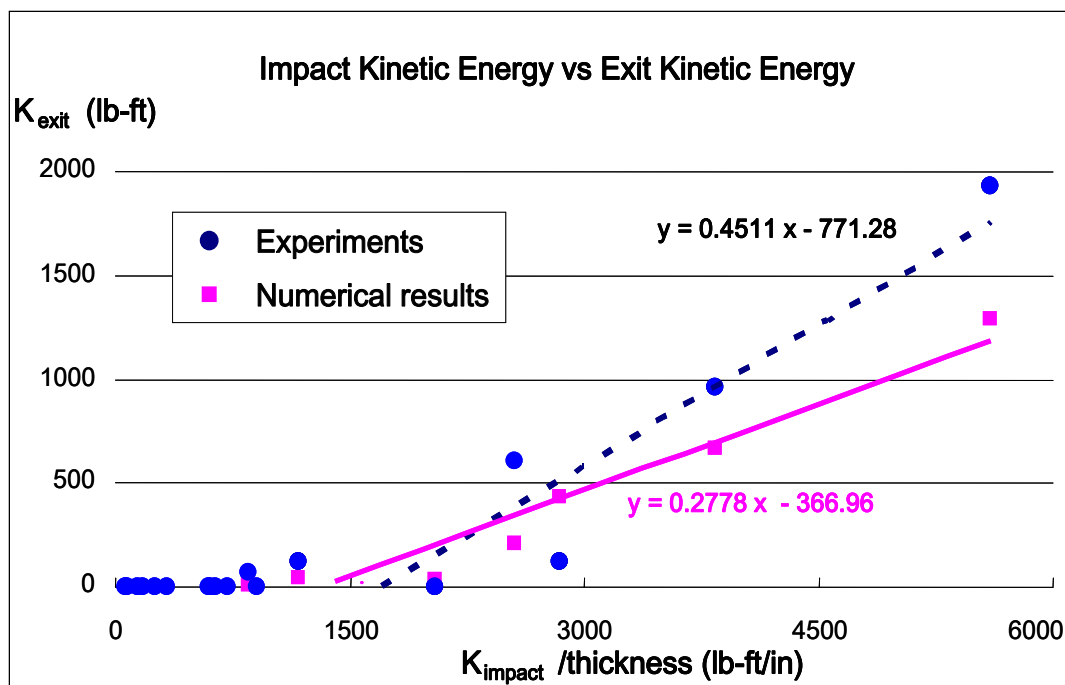


Figure 79. Normalized impact kinetic energy vs. exit kinetic energy.

Table 14. Fitted coefficient c and critical value $\bar{K}_{critical}$.

	c	$\bar{K}_{critical}$
RKPM	0.2778 (in.)	1321 (lb-ft)
Experiments	0.4511 (in.)	1710 (lb-ft)

Convert in to mm as $(\cdot) \times 25.4$; convert lb-ft to J as $(\cdot) \times 1.3558$.

erosion, while the J2 plasticity model does not include the thermal effects of metallic material. As the temperature of the projectile increases, the strength of the material should decline. This suggests that the magnitude of DIF needs to be modified to compensate for the thermal effects. In the current NMAP code, the magnitude of DIF employed is only determined by the impact velocity. For the impact velocity larger than 610 m/s, DIF of 1.5 is used, while DIF of 1.2 is selected for the impact velocity less than 610 m/s. The larger DIF reduces energy dissipation during perforation yielding an increase of exit velocity. Furthermore, the damage model in the projectile is not considered in the present study. These are the reasons why the numerical results exhibit higher exit velocity than the experimental ones for these two cases. If the thermal and damage effects are considered in the numerical models, more dissipated energy will be encountered in the numerical simulation, and lower numerical exit velocities are expected.

Empirical formulas are proposed to quantify the velocity reduction of projectile. As can be seen from Figures 76 to 78, the numerical V&V results show a good agreement with the experiments. Based on the velocity criterion, the numerical results show similar trends in comparison with the experimental data except for the cases with 32-grain projectile. As aforementioned, this can be attributed to the fact that thermal effects and projectile damage mechanisms are not considered in the simulation models.

For the material model of concrete, a multiscale AFC model is proposed. For the proposed multiscale AFC model, tensile and shear damage effects are considered separately, while in the original macroscale AFC model, only shear damage effect is included in the numerical algorithm. As can be seen from the damage patterns, the multiscale AFC model exhibits larger damage zones than the macroscale model due to the consideration of tensile damage.

6 Conclusions

A multiscale RKPM formulation for impact and penetration modeling was developed, with specific focus on methods to accurately model key phenomena such as multi-body contact, fast-evolving material damage, large material deformation, and large material flow. An enhanced semi-Lagrangian formulation was introduced to address the breakdown of the Lagrangian approximation when conditions such as free surface formation or closure occur, which commonly result from material fracture during penetration events. Temporal stability of the semi-Lagrangian formulation was also analyzed, and a strong dependence was shown between stability criteria and the velocity gradient. Dependence of the stability criteria on velocity gradient is of particular importance in impact problems, where very large gradients are encountered in the impact region. For strain calculation, a stabilized non-conforming nodal integration scheme was introduced. The SNNI scheme was derived from the similar stabilized conforming nodal integration method, but with simpler non-conforming strain smoothing domains that do not require continuous reconstruction in the semi-Lagrangian formulation.

To model multi-body contact, an enhanced kernel contact algorithm was developed. Contact conditions were detected based on kernel interaction between nodes of different bodies, allowing body interaction to be captured naturally within the RKPM framework. As such, a priori definition of contact surfaces was not required, which is a significant enhancement for problems where extensive material separation and debris formation occur. A technique using the level set method was introduced to determine surface normal at a contact surface. The level set method provides a more accurate determination of the surface normal as compared to using a point-to-point technique. Decomposition of the internal force between two nodes was used to identify the normal force acting between them, and tangential forces were subsequently modified using the Coulomb friction law. Under separation conditions, internal forces were modified to prevent non-physical tensile forces that were shown to give erroneous pull-back conditions.

A new multiscale formulation for damage evolution was developed, where continuum-scale damage evolution was linked to microstructure failure.

First a microcell analysis was introduced to explicitly model crack propagation in the material microstructure. Relationships between stress, strain and Helmholtz free energy of the microcell and homogenized continuum were then used to derive a new continuum-scale damage evolution function, which was termed the microcrack-informed damage model. It was shown that this multiscale approach could be used to derive microcrack-informed damage laws ranging from simple one- and two-parameter models to full-tensorial damage descriptions. The numerical size effect between the microcell and structural-scale models was also studied, and a scaling law was presented to obtain mesh objectivity. Notably, this multiscale formulation provides a framework in which numerical experiments at the microscale are used to determine continuum-scale parameters that were otherwise based on phenomenological laws. As such, much more accurate descriptions of these parameters (such as the damage evolution function) are provided, yielding a desired capability in terms of structural-scale analysis and multiscale material design.

New formulations developed in the project were implemented into the 3-D NMAP parallel code. The microcrack informed damage model was implemented into the ERDC-developed Advanced Fundamental Concrete model, and was used to define tensile damage evolution in the CorTuf ultra high-strength concrete material. This MIDM-enhanced version of the AFC model was also implemented into NMAP for the analysis of projectile penetration into ultra high-strength concrete targets.

The new formulations and NMAP code implementation were evaluated through 18 V&V tests that were based on penetration experiments conducted by ERDC. A small set of numerical experiments were initially performed to determine optimal values for certain model parameters. Key findings from the parameter optimization study included discretization guidelines, critical time-step criteria, dynamic increase factor criteria, and recommendations for boundary layer corrections, projectile support size adjustment and smoothing zone geometry. In terms of the V&V test results, generally good agreement was found from comparison of the numerical results and experimental data. With regard to percent velocity reduction of the projectile, error of 10% or less was observed in 14 of the tests. Error in the remaining four tests was less than 24%, where these four cases coincided with strong overmatch conditions in the experiments. Several of the V&V tests (Runs 3, 7, 9, 12 and 13) were selected to compare results using the original AFC model and the MIDM-enhanced version.

Each case was run using both AFC model versions, and comparisons were made in terms of exit velocity and panel damage. It was found that the MIDM-enhanced AFC model generally predicted higher exit velocity, larger craters and more damage than the original AFC model. These results were in-keeping with a more accurate tensile failure description provided by the multiscale formulation. Lastly, numerical and experimental results were used to develop empirical equations for predicting terminal ballistic conditions. Velocity criteria or kinetic energy criteria were used as a basis for the empirical expressions, and either exit velocity or exit kinetic energy was estimated as a function of impact velocity or energy normalized by the panel thickness. These empirical estimators were shown to provide reasonable predictions over the given range of impact conditions.

References

- Abaqus 6.5 *User's manual*. 2005. Providence, RI: Simulia.
- Adley, M. D., A. O. Frank, K. T. Danielson, S. A. Akers, and J. L. O'Daniel. 2010. *The advanced fundamental concrete (AFC) model*. Technical Report ERDC/GSL TR-10-51. Vicksburg, MS: U.S. Army Engineer Research and Development Center.
- American Society for Testing and Materials. (ASTM). 2008. *Standard specification for tool steels alloy*. Designation: A 681-08. West Conshohocken, PA.
- Bazant, Z. P. 1984. Size effect in blunt fracture: concrete, rock, metal. *ASCE J. Eng. Mech.* 110(4):518-535.
- Bakhvalov, N., and G. Panasenko. 1989. *Homogenization: Averaging processes in periodic media*. Kluwer Academic Publishers Group, Dordrecht.
- Belytschko, T., S. Loehnert, and J. H. Song. 2008. Multiscale aggregating discontinuities: A method for circumventing loss of material stability. *Int. J. Numer. Method Mech. Eng.* 73:869-894.
- Benssousan, A., J. L. Lions, and G. Papanicolaou. 1978. *Asymptotic analysis for periodic media*. North-Holland, Amsterdam.
- Boone, R. N. *Ballistic impact and perforation of ultra-high strength concrete panels*. M.S. thesis (in preparation), Mississippi State University.
- Budiansky, B., and R. J. O'Connell. 1976. Elastic moduli of cracked solid. *Int. J. Solid Struct.* 12:81-95.
- Chen, J. S., C. H. Pan, C. T. Tu, and W. K. Liu. 1996. Reproducing kernel particle methods for large deformation analysis of non-linear structures. *Comput. Method Appl. Mech. Eng.* 139:195-227.
- Chen, J. S., and H. P. Wang. 2000. Some recent improvements in meshfree methods for incompressible finite elasticity boundary value problems with contact. *Comput. Mech.* 25:137-156.
- Chen, J. S., C. T. Wu, S. Yoon, and Y. You. 2001. A stabilized conforming nodal integration for Galerkin meshfree methods. *Int. J. Numer. Method Eng.* 50:435-466.
- Chen, J. S., S. Yoon, and C. T. Wu. 2002. Nonlinear version of stabilized conforming nodal integration for Galerkin meshfree methods. *Int. J. Numer. Method Eng.* 53:2587-2615.
- Chen, J. S., W. Hu, M. Puso, Y. Wu, and X. Zhang. 2006. Strain smoothing for stabilization and regularization of Galerkin meshfree method. *Lecture notes in computational science and engineering* 57:57-76.

- Chen, J. S., and Y. Wu. 2007. Stability in Lagrangian and semi-Lagrangian reproducing kernel discretizations using nodal integration in nonlinear solid mechanics. In *Computational methods in applied sciences*, ed. V. M. A. Leitao, C. J. S. Alves, and C. A. Duarte, 55-77. Springer.
- Chen, J. S., P. C. Guan, L. Du, Y. C. Lin, and C. H. Lee. 2009. *A multi-scale meshfree approach for modeling fragment penetration into ultra high strength concrete: Part 1*. Project Technical Report.
- Cheng, C.H. 1992. Modeling of the elasto-plastic behavior for composite materials using homogenization method. Ph.D. dissertation. University of Michigan.
- Chi, S.W., C.H. Lee, M.J. Roth, J.S. Chen, and T.R. Slawson. *in preparation*. *User's manual for nonlinear meshfree analysis program (NMAP), Version 1.0*. Technical Report ERDC/GSL TR-11-xx. Vicksburg, MS: U.S. Army Engineer Research and Development Center.
- de Borst, R. 1986. Ph. D. thesis. Delft University of Technology, The Netherlands.
- Faria, R., J. Oliver, and M. Cervera. 1998. A strain-based plastic viscous-damage model for massive concrete structures. *Int. J. Solids Struct.* 35(14):1533-1558.
- Fish, J., K. Shek, M. Pandheeradi, and M. S. Shephard. 1997. Computational plasticity for composite structures based on mathematical homogenization: Theory and practice. *Comput. Method Appl. Mech. Eng.* 148(1-2):53-73.
- Fleming, M., Y. A. Chu, B. Moran, and T. Belytschko. 1997. Enriched element-free Galerkin methods for crack tip fields. *Int. J. Numer. Method Eng.* 40:1483-1504.
- Guan, P., J. S. Chen, Y. Wu, H. Teng, J. Gaidos, K. Hofstetter, and M. Alsaleh. 2009. A semi-Lagrangian reproducing kernel formulation for modeling earth moving operations. *Mech. Mater.* 41:670-683.
- Guan, P. C., S. W. Chi, J. S. Chen, T. R. Slawson, and M. J. Roth. *In preparation*. Semi-Lagrangian reproducing kernel particle method for fragment-impact problems. *Int. J. Impact Eng.*
- Guedes, J. M., and N. Kikuchi. 1990. Preprocessing and postprocessing for materials based on the homogenization method with adaptive finite element methods. *Comput. Method Appl. Mech. Eng.* 83(2):143-198.
- Hill, R. 1963. Elastic properties of reinforced solids: Some theoretical principles. *J. Mech. Phys. Solids* 11:357-372.
- Li, J., and X. D. Ren. 2009. Stochastic damage model for concrete based on energy equivalent strain. *Int. J. Solids Struct.* 46:2407-2419.
- Liu, W.K., S. Jun, and Y. F. Zhang. 1995. Reproducing kernel particle methods. *Int. J. Numer. Meth. Fl.* 20:1081-1106.
- Mazars, J. 1984. Application de la mecanique de l'endommagement au comportement non lineaire et a la rupture du beton de structure. *These de Doctorate d'Etat*, L.M.T., Universite Paris, France.

- Meyer, R., H. Ahrens, and H. Duddeck. 1994. Material model for concrete in cracked and uncracked states. *J. Eng. Mech., ASCE* 120(9):1877–1895.
- Mori, T., and K. Tanaka. 1973. Average stress in matrix and average elastic energy of materials with misfitting inclusions. *Acta Metal.* 21:571-583.
- Möes, N., and T. Belytschko. 2002. Extended finite element method for cohesive crack growth. *Eng. Fract. Mech.* 69:813-833.
- Nemat-Nasser, S., and M. Hori. 1999. *Micromechanics: overall properties of heterogeneous materials*. 2nd edition. Elsevier Science B.V.
- Norris, A. N. 1985. A different scheme for the effective moduli of composites. *Mech. Mater.* 4:1-16.
- Petersson, P. E. 1981. Crack growth and development of fracture zones in plain concrete and similar materials. *Report No. TVBM-1006*, Division of Building Materials, University of Lund, Sweden.
- Ren, X., J. S. Chen, J. Li, T. R. Slawson, and M. J. Roth. In preparation. Micro-cracks informed damage model for brittle solids. *Int. J. Solids Struct.*
- Rule, W. K., and S. E. Jones. 1998. A revised form for the Johnson-Cook strength model. *Int. J. Impact Eng.* 21(8):609-624.
- Taylor, G. I. 1948. The use of flat-ended projectiles for determining dynamic yield stress, Part I. In *Proc. R. Soc. London, Ser. A* 194:289–299.
- Timoshenko, S. P., and J. N. Goodier. 1934. *Theory of elasticity*. McGraw-Hill, New York.
- Wilkins, M. L., and M. W. Guinan. 1973. Impact of cylinders on rigid boundary. *J. Appl. Phys.* 44:1200–1206.
- Williams, E. M., S. S. Graham, P. A. Reed, and T. S. Rushing. 2009. Laboratory characterization of Cor-Tuf concrete with and without steel fibers. Technical Report ERDC/GSL TR-09-22. Vicksburg, MS: U.S. Army Engineer Research and Development Center.
- Wu, J. Y., J. Li, and R. Faria. 2006. An energy release rate-based plastic-damage model for concrete. *Int. J. Solids Struct.* 43(3–4):583–612.
- You, Y., J. S. Chen, and T. E. Voth. 2002. Characteristics of semi- and full discretization of stabilized Galerkin meshfree method. *Finite Elements in Analysis and Design* 38:999-1012.

Appendix A: Derivation of Influence Tensor Using Asymptotic Expansion Based Homogenization

An alternative approach for relating microscopic and macroscopic variables is the asymptotic expansion based homogenization method. Consider the model problem described by coarse-scale coordinate \mathbf{x} and fine-scale coordinate \mathbf{y} as shown in

Figure 14. The two length scales are related with a small parameter, ε , as

$$\mathbf{y} = \frac{1}{\varepsilon} \mathbf{x} \quad (\text{A1})$$

The spatial derivatives of a function Φ^ε with superscript ε denoting the combined (total) coarse-fine scale characters is expressed as

$$\nabla_{\mathbf{x}} \Phi^\varepsilon(\mathbf{x}) = \nabla_{\mathbf{x}} \Phi(\mathbf{x}, \mathbf{y}) = \nabla_{\mathbf{x}} \Phi(\mathbf{x}, \mathbf{y}) + \frac{1}{\varepsilon} \nabla_{\mathbf{y}} \Phi(\mathbf{x}, \mathbf{y}) \quad (\text{A2})$$

Based on asymptotic expansion, the total displacement vector is expanded as

$$\mathbf{u}^\varepsilon(\mathbf{x}) = \sum_{i=0}^{\infty} \varepsilon^i \mathbf{u}^{[i]}(\mathbf{x}, \mathbf{y}) \quad (\text{A3})$$

Substituting (A3) into Equation 41 and considering (A1) and (A2), expansion of the strain tensor is obtained as

$$\mathbf{e}^\varepsilon = \nabla_{\mathbf{x}}^s \mathbf{u}^\varepsilon = \sum_{k=-1}^{\infty} \varepsilon^k \mathbf{e}^{[k]} \quad (\text{A4})$$

where

$$\mathbf{e}^{[-1]} = \nabla_{\mathbf{y}}^s \mathbf{u}^{[0]} \quad (\text{A5})$$

$$\mathbf{e}^{[k]}(\mathbf{u}) = \nabla_{\mathbf{x}}^s \mathbf{u}^{[k]} + \nabla_{\mathbf{y}}^s \mathbf{u}^{[k+1]} \quad k \geq 0 \quad (\text{A6})$$

Introducing the elasticity tensor, the stress expansion is

$$\boldsymbol{\sigma}^{\varepsilon} = \mathbf{C}^{\varepsilon} : \mathbf{e}^{\varepsilon} = \sum_{k=-1}^{\infty} \varepsilon^k \boldsymbol{\sigma}^{[k]} \quad (\text{A7})$$

where

$$\boldsymbol{\sigma}^{[k]} = \mathbf{C}^{\varepsilon} : \mathbf{e}^{[k]} \quad (\text{A8})$$

Substituting expansion (A8) into the equilibrium condition Equation 36, the leading order equilibrium equations is obtained

$$\nabla_y \cdot \boldsymbol{\sigma}^{[-1]} = 0 \quad (\text{A9})$$

$$\nabla_x \cdot \boldsymbol{\sigma}^{[k]} + \nabla_y \cdot \boldsymbol{\sigma}^{[k+1]} = 0 \quad k \geq -1 \quad (\text{A10})$$

The formal solutions of these equations were discussed in the literature (Cheng 1992; Fish et al. 1997; Guedes and Kikuchi et al. 1990) and outlined are only the important results here. The first and second order formal solutions for displacement are expressed as

$$\mathbf{u}^{[0]} = \mathbf{v}^{[0]}(\mathbf{x}) \quad (\text{A11})$$

$$\mathbf{u}^{[1]} = \mathbf{v}^{[1]}(\mathbf{x}) + \chi(\mathbf{y}) : \nabla_x^s \mathbf{v}^{[0]}(\mathbf{x}) \quad (\text{A12})$$

where $\mathbf{v}^{[0]}(\mathbf{x})$ and $\mathbf{v}^{[1]}(\mathbf{x})$ are the coarse and fine scale solution functions of \mathbf{u} , and $\chi(\mathbf{y})$ is the third order characteristic tensor function of the microscopic cell (Bakhvalov and Panasenko 1989).

Consider the truncation of the strain and stress expansions to two scales

$$\mathbf{e}^{\varepsilon} = \frac{1}{\varepsilon} \mathbf{e}^{[-1]} + \mathbf{e}^{[0]} + \dots \approx \frac{1}{\varepsilon} \mathbf{e}^{[-1]} + \mathbf{e}^{[0]} \quad (\text{A13})$$

$$\boldsymbol{\sigma}^{\varepsilon} = \frac{1}{\varepsilon} \boldsymbol{\sigma}^{[-1]} + \boldsymbol{\sigma}^{[0]} + \dots \approx \frac{1}{\varepsilon} \boldsymbol{\sigma}^{[-1]} + \boldsymbol{\sigma}^{[0]} \quad (\text{A14})$$

where:

$$\mathbf{e}^{[-1]} = \nabla_y^s \mathbf{u}^{[0]} = \nabla_y^s \mathbf{v}^{[0]}(\mathbf{x}) = 0 \quad (\text{A15})$$

$$\boldsymbol{\sigma}^{[-1]} = \mathbf{C}^\varepsilon : \mathbf{e}^{[-1]} = \mathbf{C}^\varepsilon : \nabla_y^s \mathbf{u}^{[0]} = \mathbf{C}^\varepsilon : \nabla_y^s \mathbf{v}^{[0]}(\mathbf{x}) = 0 \quad (\text{A16})$$

$$\mathbf{e}^{[0]} = \nabla_x^s \mathbf{u}^{[0]} + \nabla_y^s \mathbf{u}^{[1]} = [\mathbf{I} + \nabla_y^s \chi(\mathbf{y})] : \nabla_x^s \mathbf{v}^{[0]}(\mathbf{x}) \quad (\text{A17})$$

$$\boldsymbol{\sigma}^{[0]} = \mathbf{C}^\varepsilon : \mathbf{e}^{[0]} = \mathbf{C}^\varepsilon : [\mathbf{I} + \nabla_y^s \chi(\mathbf{y})] : \nabla_x^s \mathbf{v}^{[0]}(\mathbf{x}) \quad (\text{A18})$$

Substituting (A15~18) into (A13~14), results in the following

$$\mathbf{e}^\varepsilon \approx \mathbf{e}^{[0]} = \nabla_x^s \mathbf{u}^{[0]} + \nabla_y^s \mathbf{u}^{[1]} = [\mathbf{I} + \nabla_y^s \chi(\mathbf{y})] : \nabla_x^s \mathbf{u}^{[0]}(\mathbf{x}) \quad (\text{A19})$$

$$\boldsymbol{\sigma}^\varepsilon \approx \boldsymbol{\sigma}^{[0]} = \mathbf{C}^\varepsilon : [\mathbf{I} + \nabla_y^s \chi(\mathbf{y})] : \nabla_x^s \mathbf{u}^{[0]}(\mathbf{x}) \quad (\text{A20})$$

where \mathbf{I} denotes the fourth-order identity tensor. Substituting stress expression (A20) into equilibrium Equation 36 and the cohesive traction Equation 39, the following equations result for solving the third-order tensor, $\chi(\mathbf{y})$

$$\nabla_y \cdot (\mathbf{C}^\varepsilon : \nabla_y^s \chi(\mathbf{y})) = 0 \quad \text{in } \Omega_y \quad (\text{A21})$$

$$[\mathbf{C}^\varepsilon : \nabla_y^s \chi(\mathbf{y}) : \nabla_x^s \mathbf{v}^{[0]}(\mathbf{x})] \cdot \mathbf{n} = -[\mathbf{C}^\varepsilon : \nabla_x^s \mathbf{v}^{[0]}(\mathbf{x})] \cdot \mathbf{n} + \mathbf{h} \quad \text{on } \Gamma_c \quad (\text{A22})$$

Comparing Equation 52 and (A19), the influence tensor can be expressive by the characteristic tensor as

$$\mathbf{A}^\varepsilon = -\nabla_y^s \chi(\mathbf{y}) \quad (\text{A23})$$

Appendix B: Derivation of Energy Bridging Equation Using Asymptotic Expansion Based Homogenization

Here we show that the energy bridging Equation 69 can be obtained by an asymptotic expansion based method. Substituting Equations (A19) and (A20) into the microscopic free energy defined in Equation 64 yields

$$\begin{aligned}\Psi^e &= \frac{1}{2} \boldsymbol{\sigma}^e : \mathbf{e}^e = \frac{1}{2} \mathbf{e}^e : \mathbf{C}^e : \mathbf{e}^e = \frac{1}{2} (\nabla_x^s \mathbf{u}^{[0]} + \nabla_y^s \mathbf{u}^{[1]}) : \mathbf{C}^e : (\nabla_x^s \mathbf{u}^{[0]} + \nabla_y^s \mathbf{u}^{[1]}) \\ &= \frac{1}{2} \nabla_x^s \mathbf{u}^{[0]} : \mathbf{C}^e : \nabla_x^s \mathbf{u}^{[0]} + \frac{1}{2} \nabla_y^s \mathbf{u}^{[1]} : \mathbf{C}^e : \nabla_y^s \mathbf{u}^{[1]} + \nabla_x^s \mathbf{u}^{[0]} : \mathbf{C}^e : \nabla_y^s \mathbf{u}^{[1]}\end{aligned}\quad (\text{B1})$$

Integrating over the microscopic cell, the following is obtained

$$\begin{aligned}\int_{\Omega_Y} \Psi^e d\Omega &= \int_{\Omega_Y} \left(\frac{1}{2} \nabla_x^s \mathbf{u}^{[0]} : \mathbf{C}^e : \nabla_x^s \mathbf{u}^{[0]} \right) d\Omega \\ &+ \int_{\Omega_Y} \left(\frac{1}{2} \nabla_y^s \mathbf{u}^{[1]} : \mathbf{C}^e : \nabla_y^s \mathbf{u}^{[1]} \right) d\Omega + \int_{\Omega_Y} (\nabla_x^s \mathbf{u}^{[0]} : \mathbf{C}^e : \nabla_y^s \mathbf{u}^{[1]}) d\Omega\end{aligned}\quad (\text{B2})$$

The three terms on the right hand side of Equation (B2) are rearranged as follows. The first term is expressed as

$$\int_{\Omega_Y} \left(\frac{1}{2} \nabla_x^s \mathbf{u}^{[0]} : \mathbf{C}^e : \nabla_x^s \mathbf{u}^{[0]} \right) d\Omega = \frac{V_Y}{2} \nabla_x^s \mathbf{u}^{[0]} : \langle \mathbf{C}^e \rangle : \nabla_x^s \mathbf{u}^{[0]}\quad (\text{B3})$$

The second term can be further manipulated by considering $k = -1$ in Equation (A10) to yield

$$\nabla_x \cdot \boldsymbol{\sigma}^{[-1]} + \nabla_y \cdot \boldsymbol{\sigma}^{[0]} = 0 \quad \text{in } \Omega_Y \quad (\text{B4})$$

Further considering the crack surface traction condition as

$$\boldsymbol{\sigma}^{[0]} \cdot \mathbf{n} = \mathbf{h} \quad \text{on } \Gamma_c \quad (\text{B5})$$

and substituting Equation (A16) in Equation (B4), the following results

$$\nabla_y \cdot \boldsymbol{\sigma}^{[0]} = 0 \quad (\text{B6})$$

Multiplying Equation (B6) by $\mathbf{u}^{[1]}$ and integrating it over Ω_y yields

$$\int_{\Omega_y} \mathbf{u}^{[1]} \cdot \nabla_y \cdot \boldsymbol{\sigma}^{[0]} d\Omega = 0 \quad (\text{B7})$$

By integration by parts, yields the following

$$\int_{\Omega_y} \mathbf{u}^{[1]} \cdot \nabla_y \cdot \boldsymbol{\sigma}^{[0]} d\Omega = \int_{\Omega_y} \boldsymbol{\sigma}^{[0]} \cdot \nabla_y \cdot \mathbf{u}^{[1]} d\Omega - \int_{\Gamma_c} \mathbf{u}^{[1]} \cdot \boldsymbol{\sigma}^{[0]} \cdot \mathbf{n} dS = 0 \quad (\text{B8})$$

where Γ_c is the crack surface within the microscopic cell. Considering the boundary condition in Equation (B5) and the symmetry of stress tensor, $\boldsymbol{\sigma}^{[0]}$, the following is shown

$$\int_{\Omega_y} \boldsymbol{\sigma}^{[0]} : \nabla_y^s \mathbf{u}^{[1]} d\Omega = - \int_{\Gamma_c} \mathbf{u}^{[1]} \cdot \mathbf{h} dS \quad (\text{B9})$$

Substituting Equation (A18) into Equation (B9), one obtains

$$\int_{\Omega_y} \nabla_x^s \mathbf{u}^{[0]} : \mathbf{C}^e : \nabla_y^s \mathbf{u}^{[1]} d\Omega + \int_{\Omega_y} \nabla_y^s \mathbf{u}^{[1]} : \mathbf{C}^e : \nabla_y^s \mathbf{u}^{[1]} d\Omega = - \int_{\Gamma_c} \mathbf{u}^{[1]} \cdot \mathbf{h} dS \quad (\text{B10})$$

The second term on the right side of Equation (B2) is then obtained. For the third term on the right hand side of Equation (B2), considering Equation (A12)

$$\int_{\Omega_y} \nabla_x^s \mathbf{u}^{[0]} : \mathbf{C}^e : \nabla_y^s \mathbf{u}^{[1]} d\Omega = \nabla_x^s \mathbf{u}^{[0]} : \left[\int_{\Omega_y} \mathbf{C}^e : \nabla_y^s \chi(\mathbf{y}) d\Omega \right] : \nabla_x^s \mathbf{u}^{[0]} \quad (\text{B11})$$

Substituting Equation (A20) into the homogenized stress expressed in Equation 49 yields

$$\begin{aligned} \bar{\boldsymbol{\sigma}} &= \langle \boldsymbol{\sigma}^e \rangle = \langle \mathbf{C}^e : [\mathbf{I} + \nabla_y^s \chi(\mathbf{y})] \rangle : \nabla_x^s \mathbf{u}^{[0]}(\mathbf{x}) \\ &= \langle \mathbf{C}^e \rangle : \nabla_x^s \mathbf{u}^{[0]}(\mathbf{x}) + \langle \mathbf{C}^e : \nabla_y^s \chi(\mathbf{y}) \rangle : \nabla_x^s \mathbf{u}^{[0]}(\mathbf{x}) \end{aligned} \quad (\text{B12})$$

Comparing Equation (B11) with (B12) gives

$$V_y \bar{\sigma} : \nabla_{\mathbf{x}}^s \mathbf{u}^{[0]} = V_y \nabla_{\mathbf{x}}^s \mathbf{u}^{[0]} : \langle \mathbf{C}^e \rangle : \nabla_{\mathbf{x}}^s \mathbf{u}^{[0]} + \int_{\Omega_y} \nabla_{\mathbf{x}}^s \mathbf{u}^{[0]} : \mathbf{C}^e : \nabla_{\mathbf{y}}^s \mathbf{u}^{[1]} d\Omega \quad (\text{B13})$$

Then substituting Equations (B3), (B10), and (B13) into Equation (B2), the following is obtained

$$\frac{1}{V_y} \left(\int_{\Omega_y} \Psi^e d\Omega + \frac{1}{2} \int_{\Gamma_c} \mathbf{u}^{[1]} \cdot \mathbf{h} dS \right) = \frac{1}{2} \bar{\sigma} : \nabla_{\mathbf{x}}^s \mathbf{u}^{[0]} \quad (\text{B14})$$

It is observed that $\nabla_{\mathbf{x}}^s \mathbf{u}^{[0]}$ is the macroscopic strain, $\bar{\epsilon}$, that is imposed on the microscopic cell by Equation 67. By substituting Equation 60 in Equation (B14), the following is finally obtained

$$\bar{\Psi} = \frac{1}{V_y} \left(\int_{\Omega_y} \Psi^e d\Omega + \frac{1}{2} \int_{\Gamma_c} \mathbf{u}^{[1]} \cdot \mathbf{h} dS \right) \quad (\text{B15})$$

Appendix C: Two-Variable Damage Model

According to the continuum damage theory, the general expression of the fourth-order damage representation is

$$\boldsymbol{\sigma} = (\mathbf{I} - \mathbf{D}) : \mathbf{C}_0 : \boldsymbol{\varepsilon}^e \quad (\text{C1})$$

where \mathbf{C}_0 is the initial elastic stiffness tensor, \mathbf{D} is the fourth order damage tensor, and $\boldsymbol{\varepsilon}^e = \boldsymbol{\varepsilon} - \boldsymbol{\varepsilon}^p$ and $\boldsymbol{\varepsilon}_p$ is the plastic strain. The effective stress is defined as

$$\boldsymbol{\sigma}_0 = \mathbf{C}_0 : \boldsymbol{\varepsilon}^e \quad (\text{C2})$$

Hence, the damage model in Equation (C1) can be expressed as

$$\boldsymbol{\sigma} = (\mathbf{I} - \mathbf{D}) : \boldsymbol{\sigma}_0 \quad (\text{C3})$$

To account for the unilateral effect, the positive-negative decomposition of the effective stress tensor is defined as

$$\boldsymbol{\sigma}_0 = \boldsymbol{\sigma}_0^+ + \boldsymbol{\sigma}_0^- \quad (\text{C4})$$

$$\boldsymbol{\sigma}_0^+ = \mathbf{P}^+ : \boldsymbol{\sigma}_0 \quad (\text{C5})$$

$$\boldsymbol{\sigma}_0^- = \boldsymbol{\sigma}_0 - \boldsymbol{\sigma}_0^+ = \mathbf{P}^- : \boldsymbol{\sigma}_0 \quad (\text{C6})$$

where the fourth-order projection tensors \mathbf{P}^+ and \mathbf{P}^- are (Faria et al. 1998)

$$\mathbf{P}^+ = \sum_i H(\hat{\sigma}_i) \mathbf{p}_i \otimes \mathbf{p}_i \otimes \mathbf{p}_i \otimes \mathbf{p}_i \quad (\text{C7})$$

$$\mathbf{P}^- = \mathbf{I} - \mathbf{P}^+ \quad (\text{C8})$$

in which \mathbf{I} is the fourth-order identity, $\hat{\sigma}_i$ and \mathbf{p}_i are the i^{th} eigenvalue and the corresponding eigenvector for the effective stress tensor $\boldsymbol{\sigma}_0$, and $H(x)$ is the Heaviside function

$$H(x) = \begin{cases} 1 & x \geq 0 \\ 0 & x < 0 \end{cases} \quad (C9)$$

Correspondingly, two damage scalars, d^+ and d^- , are introduced to describe the damage of materials under tension and compression respectively. According to the principles of thermodynamics, the state of an ensemble could be described by using the definition of Helmholtz free energy (HFE), which is expressed by using the state variables and internal variables. The total elastoplastic HFE is defined as

$$\psi = \psi(\boldsymbol{\epsilon}^e, \boldsymbol{\kappa}, d^+, d^-) \quad (C10)$$

where $\boldsymbol{\kappa}$ is the plastic variables. Decomposing the total HFE into the elastic and the plastic components, yields

$$\psi(\boldsymbol{\epsilon}^e, \boldsymbol{\kappa}, d^+, d^-) = \psi^e(\boldsymbol{\epsilon}^e, d^+, d^-) + \psi^p(\boldsymbol{\epsilon}^e, \boldsymbol{\kappa}, d^+, d^-) \quad (C11)$$

Neglecting the plastic strain under tension, the following plastic HFE is described

$$\psi^p(\boldsymbol{\epsilon}^e, \boldsymbol{\kappa}, d^+, d^-) = \psi^p(\boldsymbol{\epsilon}^e, \boldsymbol{\kappa}, d^-) = (1 - d^-) \psi_0^p \quad (C12)$$

The elastic HFE is further decomposed as

$$\begin{aligned} \psi^e(\boldsymbol{\epsilon}^e, d^+, d^-) &= \psi^{e+}(\boldsymbol{\epsilon}^e, d^+) + \psi^{e-}(\boldsymbol{\epsilon}^e, d^-) \\ &= (1 - d^+) \psi_0^{e+}(\boldsymbol{\epsilon}^e) + (1 - d^-) \psi_0^{e-}(\boldsymbol{\epsilon}^e) \end{aligned} \quad (C13)$$

Here the subscripts “e” and “p” refer to “elastic” and “plastic” components, respectively, and the subscript “0” refers to the “initial” state.

According to the second principle of thermodynamics, the following equation is obtained

$$\boldsymbol{\sigma} = \frac{\partial \psi^e}{\partial \boldsymbol{\epsilon}^e} = (1 - d^+) \boldsymbol{\sigma}_0^+ + (1 - d^-) \boldsymbol{\sigma}_0^- = (1 - d^+ \mathbf{P}^+ - d^- \mathbf{P}^-) : \boldsymbol{\sigma}_0 \quad (C14)$$

The damage energy release rate (DERR) can then be obtained as

$$Y^\pm = \frac{\partial \psi}{\partial d^\pm} \quad (C15)$$

REPORT DOCUMENTATION PAGE				Form Approved OMB No. 0704-0188	
Public reporting burden for this collection of information is estimated to average 1 hour per response, including the time for reviewing instructions, searching existing data sources, gathering and maintaining the data needed, and completing and reviewing this collection of information. Send comments regarding this burden estimate or any other aspect of this collection of information, including suggestions for reducing this burden to Department of Defense, Washington Headquarters Services, Directorate for Information Operations and Reports (0704-0188), 1215 Jefferson Davis Highway, Suite 1204, Arlington, VA 22202-4302. Respondents should be aware that notwithstanding any other provision of law, no person shall be subject to any penalty for failing to comply with a collection of information if it does not display a currently valid OMB control number. PLEASE DO NOT RETURN YOUR FORM TO THE ABOVE ADDRESS.					
1. REPORT DATE (DD-MM-YYYY) September 2011		2. REPORT TYPE Final report		3. DATES COVERED (From - To)	
4. TITLE AND SUBTITLE A multiscale meshfree approach for modeling fragment penetration into ultra high-strength concrete				5a. CONTRACT NUMBER	
				5b. GRANT NUMBER	
				5c. PROGRAM ELEMENT NUMBER	
6. AUTHOR(S) J. S. Chen, S. W. Chi, C. H. Lee, S. P. Lin, C. Marodon, M. J. Roth, and T. R. Slawson				5d. PROJECT NUMBER	
				5e. TASK NUMBER	
				5f. WORK UNIT NUMBER	
7. PERFORMING ORGANIZATION NAME(S) AND ADDRESS(ES) Department of Civil and Environmental Engineering University of California, Los Angeles Los Angeles, CA 90095				8. PERFORMING ORGANIZATION REPORT NUMBER ERDC/GSL TR-11-35	
9. SPONSORING / MONITORING AGENCY NAME(S) AND ADDRESS(ES) U.S. Army Engineer Research and Development Center Geotechnical and Structures Laboratory 3909 Halls Ferry Road Vicksburg, MS 39180-6199				10. SPONSOR/MONITOR'S ACRONYM(S)	
				11. SPONSOR/MONITOR'S REPORT NUMBER(S)	
12. DISTRIBUTION / AVAILABILITY STATEMENT Approved for public release. Distribution is unlimited.					
13. SUPPLEMENTARY NOTES					
14 Abstract: Results from the efforts in meshfree method development for fragment-impact modeling during April 2009 to March 2011 are described in this report. These efforts focused on an enhanced semi-Lagrangian reproducing kernel particle method formulation for modeling large material deformation and damage mechanisms, multiscale homogenization based on the energy bridging theory pertinent to fragment penetration modeling of concrete materials, and enhanced kernel contact algorithms to model multi-body contact applicable to penetration problems. Several benchmark problems associated with contact-impact simulations as well as multiscale modeling of material damage have been performed to examine the effectiveness of the developed computational methods. These newly developed computational formulations and the associated numerical algorithms have been implemented into the parallel Nonlinear Meshfree Analysis Program (NMAP) code. The numerical formulations and NMAP code implementation accomplished under this effort have been evaluated through 18 verification and validation (V&V) tests based on penetration experiments conducted at ERDC. The latest version of the NMAP code has been delivered to ERDC. This report, together with the 2009 technical report (Chen et al. 2009), offers the theoretical foundation of NMAP for general users.					
15. SUBJECT TERMS Meshfree RKPM		Damage Concrete Penetration Multiscale			
16. SECURITY CLASSIFICATION OF:			17. LIMITATION OF ABSTRACT	18. NUMBER OF PAGES 109	19a. NAME OF RESPONSIBLE PERSON
a. REPORT UNCLASSIFIED	b. ABSTRACT UNCLASSIFIED	c. THIS PAGE UNCLASSIFIED			19b. TELEPHONE NUMBER (include area code)